Strongly Confined Exciton-Polaritons in a Tunable Microcavity

Scott Dufferwiel

Department of Physics and Astronomy

University of Sheffield

Submitted for the degree of Doctor of Philosophy

December 2014

Abstract

Exciton-polaritons are quasiparticles arising from the strong coupling between quantum well excitons and photons in semiconductor microcavities. Polaritons have been shown to exhibit rich physics resulting from the polariton-polariton interaction such as non-equilibrium condensation and superfluidity. At present, quantum polariton processes such as polariton blockade and the Mott insulator transition, which rely on the strong single polariton-polariton interaction, have not been experimentally observed. This is due to the requirement of submicron lateral confinement in the polaritonic system which, using current fabrication methods, leads to degradation of the polariton linewidth. In this thesis a novel form of lateral polariton confinement is demonstrated through the use of micrometer sized hemispherical cavities. This introduces lateral photonic confinement with no degradation of the polariton linewidth and allows confinement sizes approaching the diffraction limit. In Chapter 2 the development of a fully tunable hemispherical microcavity is presented where nanopositioners are used to independently position two distributed Bragg Reflectors and form a microcavity where the cavity spectral resonance is tuned in-situ through control of the mirror separation. Strong-exciton photon coupling between quantum well excitons and cavity photons is demonstrated in Chapter 3 and submicron beam waists are presented. In Chapter 4 evidence for polariton condensation in the strongly confined system is presented where transverse modes show complex spin vortices and textures due to an effective spin-orbit coupling between the polariton pseudospin and angular momentum. Finally, fully tunable polaritonic molecules are presented in Chapter 5. Full tuning of the coupling strength is demonstrated through control of the centre-to-centre distance between adjacent cavities. In-situ tunability is performed through tuning of the exciton-photon detuning, as well as tuning of the two individual cavity resonances by introducing a relative angle between the two mirrors using goniometer stages.

Acknowledgements

I have been privileged to study in the Low Dimensional Structures and Devices (LDSD) group of the Department of Physics and Astronomy at the University of Sheffield. I would like to thank both past and present members of the group with whom my studies have overlapped. In particular I would like to thank Prof. Maurice Skolnick for giving me the opportunity to study within the group, as well as Dr. Dimitrii Krizhanovskii and Dr. Luke Wilson for their excellent guidance and supervision throughout my PhD studies.

I would also like to thank those that contributed substantially to the work in this thesis such as Dr. Francois Fras, Dr. Paul Walker, Dr. Feng Li and Dr. Emiliano Cancellieri. I also thank our collaborators, Dr. Aurelien Trichet and Prof. Jason Smith, whose expert knowledge in FIB milling of concave structures allowed the work presented in this thesis to be carried out.

Finally, I would like to thank my family and friends for their continued support.

Contents

Publication List

Journal Publications

S. Dufferwiel, F. Fras, A. Trichet, P. M. Walker, F. Li, L. Giriunas, M. N. Makhonin, L. R. Wilson, J. M. Smith, E. Clarke, M. S. Skolnick and D. N. Krizhanovskii. 'Strong exciton-photon coupling in open semiconductor microcavities', *App. Phys. Lett*, **104** 192107 (2014)

S. Schwarz, **S. Dufferwiel**, P. M. Walker, F. Withers, A. A. P. Trichet, M. Sich, F. Li, E. A. Chekhovich, D. N. Borisenko, N. N. Kolesnikov, K. S. Novoselov, M. S. Skolnick, J. M. Smith, D. N. Krizhanovskii and A. I. Tartakovskii. 'Two-dimensional metal-chalcogenide films in tunable optical microcavities', *Nano Lett.* **14** (12), 7003-7008 (2014)

S. Dufferwiel, F. Li, L. Giriunas, A. Trichet, I. Farrer, J. M. Smith, M. Skolnick and D. N. Krizhanovskii. 'Spin Textures of Polariton Condensates in a Tunable Microcavity with Strong Spin-Orbit Interaction', submitted, March (2015)

S. Dufferwiel, F. Li, L. Giriunas, A. Trichet, I. Farrer, J. M. Smith, M. Skolnick and D. N. Krizhanovskii. 'Tunable Polaritonic Molecules', in preparation, August (2014)

S. Dufferwiel, S. Schwarz, F. Withers, A. Trichet, F. Li, O. Del Pozo-Zamudio, C. Clark, A. Nalitov, D.D. Solnyshkov, G. Malpuech, K. S. Novoselov, J. M. Smith, M. S. Skolnick, D. N. Krizhanovskii, and A. I. Tartakovskii. 'Exciton-polaritons in van der Waals heterostructures embedded in tunable microcavities', submitted, April (2015)

Conference Presentations

S. Dufferwiel, F. Fras, A. Trichet, P. M. Walker, F. Li, L. Giriunas, M. N. Makhonin, L. R. Wilson, J. M. Smith, E. Clarke, M. S. Skolnick and D. N. Krizhanovskii. 'Strong exciton-photon coupling in open semiconductor microcavities', International Workshop of Polariton Devices: Scientific Research and Perspectives, St. Petersburg, March (2014)

S. Dufferwiel, F. Li, F. Fras, A. Trichet, P. M. Walker, L. Giriunas, J. M. Smith, E. Clarke, M. S. Skolnick and D. N. Krizhanovskii. 'Condensation of strongly confined exciton-polaritons in an open cavity structure', PLMCN2014, Montpellier, June (2014)

S. Dufferwiel, F. Li, F. Fras, A. Trichet, P. M. Walker, L. Giriunas, J. M. Smith, E. Clarke, M. S. Skolnick and D. N. Krizhanovskii. 'Strongly confined exciton-polaritons in a tunable semiconductor microcavity', ICPS2014, Austin, August (2014)

List of Figures

Chapter 1

Background

This thesis is concerned with the study of polaritons in a fully tunable microcavity system with embedded gallium arsenide (GaAs) quantum wells (QWs). In this Chapter a self consistent review of microcavities is presented with particular emphasis on the polaritonic effects relevant to the experimental work carried out in later chapters. Polaritons are quasiparticles arising from the strong coupling between QW excitons and photons in semiconductor microcavities. Their part-matter, part-light composition gives polaritons unique characteristics such as a large non-linear interaction inherited from their exciton component and direct access to their spin and dispersion through the outcoupling of polaritons to the far photonic field. Since their initial observation in 1992 [6], a rich research field has emerged due to their composite bosonic nature with notable experimental achievements including Bose-Einstein condensation of polaritons [7], and more recently hydrodynamical studies of polariton superfluidity [8]. Recently, many theoretical proposals based upon strong single polariton interactions have given rise to the prospect of quantum polaritons, such as single photon sources based upon polariton blockade [5] and novel states of matter such as the Tonks-Girardeau gas [9] or the Mott insulator transition [10] in polariton lattices. In this Chapter we will begin with a discussion of low dimensional semiconductors which provide the matter component of polaritons.

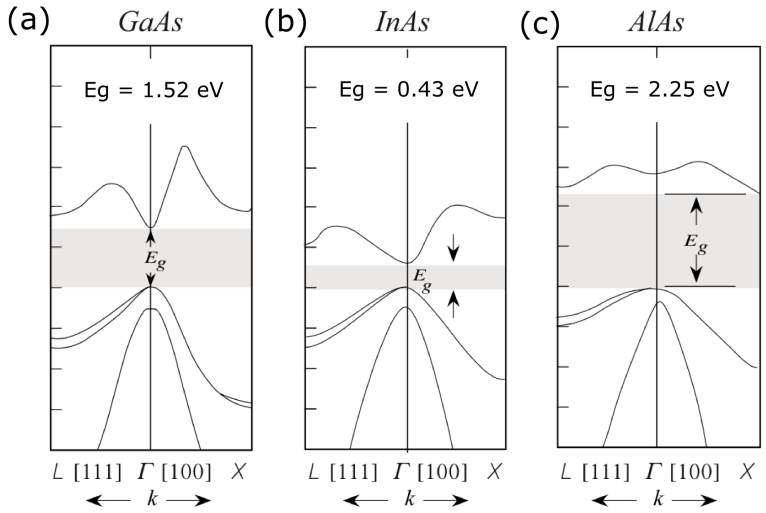

Figure 1.1: Figures taken from [11]. Band structure of (a) GaAs, (b) InAs (c) AlAs.

1.1 Low Dimensional Semiconductors

In this thesis semiconductor samples composed of GaAs and its alloys such as InGaAs and AlGaAs are studied. In this section a brief summary of the band structure is provided before discussing free Wannier-Mott excitons and QW excitons, which provide the matter component of the polaritonic system.

1.1.1 Semiconductor Band Structure

The band structures of the direct band gap semiconductors GaAs, InAs and the indirect band gap semiconductor AlAs are shown in Fig. 1.1. GaAs has a zinc-blende structure and has a direct band gap of 1.52 eV at 4K, marked by the shaded region, compared to 0.43 eV in InAs and 2.25 eV in AlAs. Alloys based upon these semiconductors such as $In_xGa_{1-x}As$ and $Al_xGa_{1-x}As$, allow control of the band gap energy through the choice of x. The bands below the shaded region correspond to the valence band. These lie below the Fermi level so are full of electrons and have p-type character. The two valence bands degenerate at k = 0 correspond to the light-holes (lh) and heavy-holes (hh). The

lifting of the degeneracy between these two bands and the third band at lower energy is due to spin-orbit splitting between hole bands and is known as the split-off band, where the energy difference is denoted by Δ. The bands above the shaded region correspond to the conduction bands and are formed from the s-antibonding electron orbitals. The band symmetry changes as a function of wavevector and is only well defined at the high symmetry points in the Brillouin zone such as Γ, X and L. Optical absorption occurs for incident photons with an energy larger than the band gap. An electron is excited from the conduction band to the valence band leaving behind a hole. The mutual coulomb attraction between the excited electron and hole leads to the form of a quasi-particle known as an exciton.

1.1.2 Wannier-Mott Excitons

The elemental excitation of a semiconductor is known as an exciton. These are quasi-particles arising from a conduction band electron and valence band hole bound by their coulomb interaction. Typically, an exciton is formed through the absorption of a photon with an energy larger than the band gap. Here, an electron is lifted from the valence band into the conduction band leaving behind an empty state. This empty state in the valence band has an effective positive charge so it is attracted to the excited conduction band electron. This mutual coulomb attraction causes the two to bind, forming an exciton with a structure comparable to that of a hydrogen atom. When the Bohr radius exceeds the lattice constant the excitons are described as Wannier-Mott excitons. Here the exciton can be described in the effective mass approximation where the periodic crystal potential is neglected and the electron and hole dispersions are described by effective masses. This is the case in the GaAs based structures studied in this thesis. An exciton can be well described by the Bohr model where the binding energy of the coulombically bound

electron-hole pair is given by

$$E_b = -\frac{\mu}{m_0}\frac{1}{\epsilon_r^2}\frac{R_H}{n^2} = -\frac{R_X}{n^2} \tag{1.1}$$

where n is the principle quantum number and R_H is the Rydberg energy of 13.6 eV. The quantity $R_X = (\mu/m_0\epsilon_r^2)R_H$ introduced here is the exciton Rydberg constant, where $\mu = (\frac{1}{m_{e*}} + \frac{1}{m_{h*}})^{-1}$ is the reduced mass of the electron-hole system. The binding energy of the exciton determines its stability. If the thermal energy k_BT is larger than the binding energy given by Eq 1.1 the excitons thermally dissociate into free electrons and holes. In GaAs the exciton binding energy is around 8 meV in contrast to the room temperature thermal energy of around 25 meV. As such, excitons in GaAs are unstable at room temperature. Instead the thermal energy must be lowered through the use of cryogenic cooling in order to exploit excitons in GaAs based devices. The electron-hole separation r_n, in the effective mass approximation, is given by the Bohr model to be:

$$r_n = \frac{m_0}{\mu}\epsilon_r n^2 a_H = n^2 a_X \tag{1.2}$$

where a_H is the Bohr radius of the hydrogen atom and $a_X = (m_0\epsilon_r/\mu)a_H$ is the exciton Bohr radius. The exciton Bohr radius determines the overlap between adjacent exciton wavefunction for a given density. At high enough densities, this overlap causes dissociation of excitons into an electron-hole plasma due to the screening of the coulomb interaction. This density is known as the Mott density, n_{Mott}, and is approximately given by the inverse volume of the exciton:

$$n_{Mott} \approx \frac{1}{\frac{4}{3}\pi r_n^3} \tag{1.3}$$

For GaAs the Mott density has a value of 1.1×10^{23} m^{-3}, which is easily achieved at high pump powers.

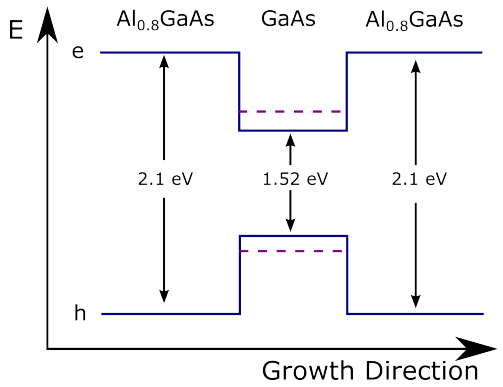

Figure 1.2: Typical GaAs quantum well heterostructure with AlGaAs barriers. The dashed lines indicate the increase in n = 1 energy level due to confinement.

1.1.3 Semiconductor Quantum Wells

Semiconductor QWs are heterostructures grown through molecule beam epitaxy (MBE) or metal-organic chemical vapour deposition (MOCVD) which allow for atomic precision in semiconductor growth. Fig. 1.2 shows a typical quantum well consisting of a thin layer of GaAs in-between AlGaAs barrier layers. The difference in band gap between the quantum well and barrier region leads to confinement of the excitons in the directions perpendicular to growth. In order to introduce quantum confinement, the height of the quantum well must be comparable to the exciton Bohr radius. This significantly alters the density of states compared to the three-dimensional case. The confinement leads to a decreased electron-hole separation which leads to increased binding energies. For a truly 2-dimensional exciton the binding energy is four times the bulk value. In AlGaAs/GaAs quantum wells, if the crystalline growth direction is along the [001] crystal axis, confinement then leads to a lifting of the degeneracy of the heavy and light hole bands due to a difference in confinement energies. Therefore, only holes from the heavy hole valence band and electrons from the conduction band determine their optical properties. Embedding QWs in optical resonators known as microcavities in regions of high electric field significantly increases the interaction between the QW excitons and cavity photons.

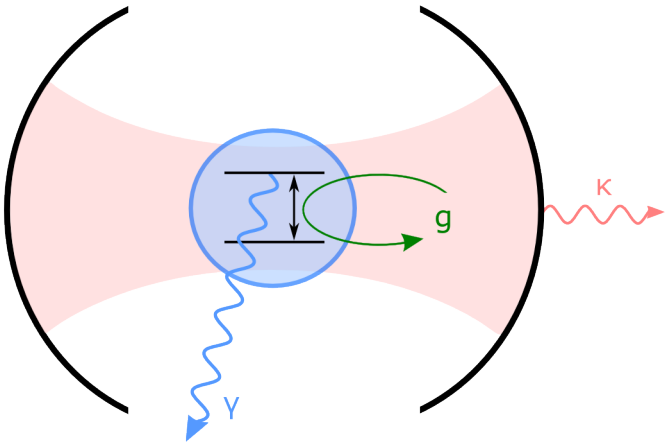

Figure 1.3: Three physical rates which determine the dynamics of an emitter-cavity system. The photon decay rate of the cavity κ, the non-resonant decay rate γ and the emitter cavity coupling parameter $g = \Omega_{Rabi}/2$.

1.1.4 Microcavities

In order to confine photons, optical cavities consisting of a planar Fabry-Perot cavity formed between two parallel mirrors can be used. Successive reflections between the two mirrors leads to interference and the formation of standing optical waves within the structure. In recent years optical microcavities have become widely utilised in order to explore the effects of cavity quantum electrodynamics (CQED). In microcavities two physical regimes exist which depend upon the magnitude of the emitter-cavity coupling strength, $\Omega_R/2$, the cavity mode decay rate, κ, and the non-resonant emitter decay rate, γ. In the weak coupling regime the losses are much greater than the emitter-cavity coupling ($\kappa, \gamma \gg \Omega_{Rabi}/2$). In this regime the cavity alters the local optical density of states and the emission rate can be enhanced or suppressed, this is known as the Purcell effect. In the strong coupling limit ($\Omega_{Rabi}/2 \gg \kappa, \gamma$) the energy is reabsorbed before it escapes the cavity and the energy oscillates between the emitter and cavity. This cyclic transfer of energy is known as a Rabi cycle and the associated splitting in energy leads to the formation of half-light half-matter quasiparticles known as polaritons.

The resonant wavelength of the cavity is determined by cavity mirror separation and is

given by $\lambda_c = 2n_{eff}L_{eff}/m$ where n_{eff}, L_{eff} are the effective cavity refractive index and length and m is the longitudinal mode index, and is chosen to be close to resonance with the transition of the active region in the cavity. In a microcavity $L_{eff} \approx \lambda$ leading to micron sized cavity lengths. Typically high reflectivity distributed Bragg reflectors (DBRs) are used to form the microcavity.

Distributed Bragg Reflectors

DBRs consist of $\lambda/4n$ thick alternating layers of high and low refractive index materials. Successive reflections between adjacent layers introduces a π phase shift of the beam causing constructive interference of reflection leading to very high reflectivities (R $\geq$ 99%) over a wavelength range called the stopband. The reflectivity of a DBR is dependent upon the refractive index of the materials used and the total number N of pairs of high and low index layers,

$$R = \left(\frac{1 - \frac{n_b}{n_a}(\frac{n_L}{n_H})^{2N}}{1 + \frac{n_b}{n_a}(\frac{n_L}{n_H})^{2N}} \right)^2 \tag{1.4}$$

where n_a and n_b are the external media refractive indices and n_h and n_l are the refractive indices of the high and low index materials. The spectral width of the stopband is determined by the refractive index contrast of the high and low index materials used,

$$\Delta_{sb} = \frac{2\lambda_{sb}\Delta n}{\pi n_{eff}} \tag{1.5}$$

where $n_{eff} = 2(\frac{1}{n_H} + \frac{1}{n_L})^{-1}$ is the effective refractive index.[12] A typical reflectivity spectrum of a microcavity is shown in Fig 1.4. The cavity resonance is at 750 nm and is set by the cavity region thickness.

Quality Factor

The ability of a cavity to confine light between its constituent mirrors is quantified by the quality-factor (Q-factor). This is a measure of the decay of the confined cavity mode due

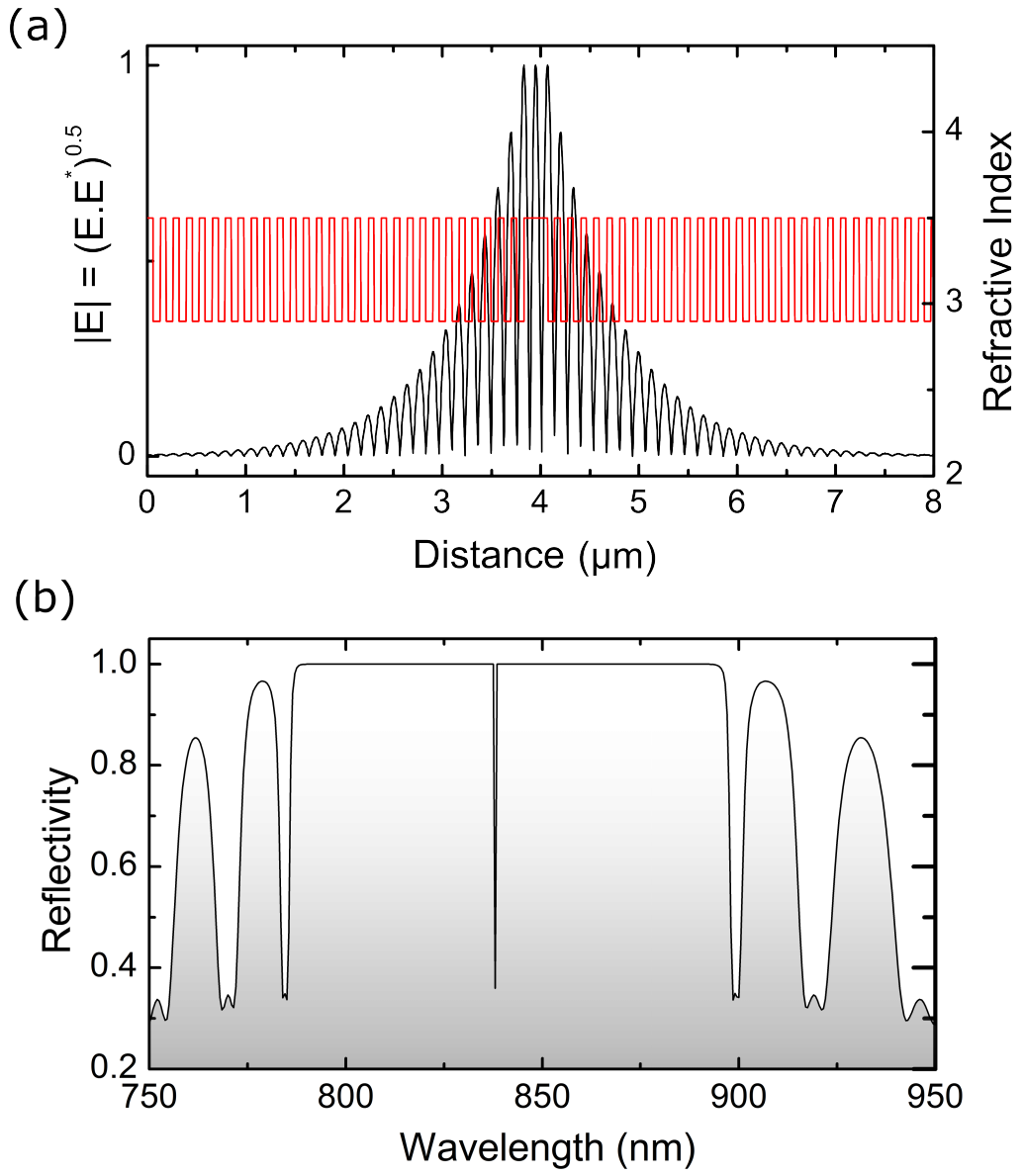

Figure 1.4: (a) Microcavity electric field profile for a cavity formed with a top (bottom) 28 (31) paired $AlGaAs/GaAs$ DBR with a λ GaAs cavity region calculated using a transfer matrix approach. (b) Reflectivity showing the cavity resonance at 840 nm.

to the escape of photons through the mirrors due to non-perfect reflectivity. The Q-factor of an optical resonator is defined as the ratio between the energy stored within the cavity divided by the energy dissipated each reflection cycle multiplied by 2π:

$$Q = \left| \omega_c \frac{U}{dU/dt} \right| \tag{1.6}$$

where ω_c is the cavity modes angular frequency, U is the electromagnetic energy stored inside the cavity and dU/dt is the energy loss rate. Solving Eq 1.6 gives the time dependence of the stored electromagnetic energy:

$$U_{(t)} = U_0 e^{-\omega_c t/Q} = U_0 e^{-t/\tau} \tag{1.7}$$

where the constant U_0 is the initial energy stored within the resonator and $\tau = Q/\omega_c$ is defined as the average lifetime of a cavity photon. Since $U_{(t)} \propto |E_{(t)}|^2$ the electric field inside the cavity be expressed as

$$E_{(t)} = E_0 e^{-\omega_c t/2Q} e^{-i\omega_c t} \tag{1.8}$$

where E_0 is the initial electric field corresponding to the initial energy density U_0. The Fourier transform of Eq 1.8 gives the expression in the frequency domain:

$$U_{(\omega)} = |E_{(\omega)}|^2 \propto \frac{1}{(\omega - \omega_c)^2 + (\omega_c/2Q)^2} \tag{1.9}$$

Hence the energy density of the stored cavity mode is expressed by a Lorentzian distribution where the full-width-half-maximum (FWHM) $\delta\omega = \omega_c/Q$. This gives the most commonly used expression to calculate the cavity Q-factor of

$$Q = \frac{\omega_c}{\delta\omega} = \frac{E_c}{\Delta E} \approx \frac{\lambda_c}{\Delta\lambda} \tag{1.10}$$

where E_c and λ_c are the cavity photon energy and wavelength.

The physical interpretation of the photonic Q-factor in terms of Fabry-Perot resonators used to confine light is that it is a measure of the ability of a cavity to confine the photonic mode. Better confinement is realised when the photonic lifetime is increased leading to larger Q-factors. In a typical resonator the photonic lifetime is governed through cavity losses which can be caused by the non-unitary reflectivity or by other loss mechanisms such as scattering at rough interfaces or absorption. In an ideal cavity, only the mirror losses due to non-perfect reflectivity determine the cavity Q-factor. In realistic cavities such as the hybrid semiconductor-dielectric cavities presented in this thesis, the loss terms due to scattering by to interface roughness play a role in the maximum achievable Q-factors.

1.2 Light-Matter Interaction

This section provides a brief overview of the light-matter interaction in semiconductor microcavities. The strong coupling regime and the physics describing polaritons most relevant to the work presented in this thesis is discussed in depth, while the weak coupling regime is discussed briefly.

1.2.1 Weak Coupling Regime

In the weak coupling regime a photon escapes the cavity before being resonantly reabsorbed by the active medium. Here the effect of the radiation field can be treated as a perturbation on the dynamics of the spontaneous emission in its excited state. Since the spontaneous emission from an excited state is due to the interaction with the vacuum field, if the energy of the transition is resonant with the cavity mode, the optical density of states increases the emission rate into the optical mode relative to the case in a vacuum and the emission rate is enhanced. In contrast if the dipole transition is placed out of resonance in a photonic gap, the photonic density of states is significantly reduced and the

emission rate decreases in comparison to the case in a vacuum. The spontaneous emission rate of a dipole emitter is characterised by Fermi's golden rule:

$$\tau = \frac{2\pi}{\hbar^2}|\mathbf{p}.\mathbf{E}(\mathbf{r},t)|^2\rho(\omega_e) \tag{1.11}$$

where ρ_e is the photonic density of states at energy $\hbar\omega_e$ and $|\mathbf{p}.\mathbf{E}(\mathbf{r},t)|^2$ is the matrix dipole element. In a vacuum the photonic density of states is given by:

$$\rho_{vac} = \frac{\omega^2 V n^3}{\pi^2 c^3} \tag{1.12}$$

where V is the mode volume, ω the angular frequency and n is the vacuum refractive index. By placing the emitter into a single mode cavity, the photonic density of states becomes significantly altered and the density is best described by a Lorentzian function:

$$\rho_c = \frac{2}{\pi}\frac{\delta\omega_c}{4(\omega-\omega_c)^2+\delta\omega_c^2} \tag{1.13}$$

where ω_c is the cavity frequency and $\delta\omega_c$ is the cavity linewidth (FWHM). The altered photonic density of states allows the enhancement or suppression of spontaneous emission through design of an appropriate cavity. This enhancement or suppression factor is known as the Purcell factor and is calculated through the ratio of spontaneous emission rates inside a cavity and outside a cavity.

$$\frac{\Gamma_c}{\Gamma_0} = \frac{3Q(\lambda_c/n)^3}{4\pi^2 V_{eff}}\frac{\delta\omega_c^2}{4(\omega_e-\omega_c)^2+\delta\omega_c}\frac{|E_{(r)}|^2}{|E_{max}|^2}\left(\frac{p.E_{(r)}}{pE}\right)^2 \tag{1.14}$$

The first term describes the figure of merit for enhancement of the spontaneous emission rate in the cavity and is known as the Purcell factor, F_P:

$$F_P = \frac{3Q(\lambda_c/n)^3}{4\pi^2 V_{eff}} \tag{1.15}$$

where Q is the cavity quality factor, n is the reactive index, λ_c is the cavity wavelength and V_{eff} is the effective mode volume. This value is often quantified by Q/V_{eff} in which maximum Purcell enhancements are expected for cavities that display large quality factors combined with small mode volumes. The second term describes the effect of detuning from the cavity resonance where maximum enhancement occurs, due to the decrease in the photonic density of states. The final terms are related to the placing of an emitter exactly at an electric field maximum (antinode) in order to maximise the coupling along with orientation of the dipole relative to the cavity field. In the ideal case where we have a dipole placed in resonance with the cavity at an electric field antinode orientated parallel to the electric field the enhancement is described fully by the Purcell factor. In reality, slight variations in the dipole placement and detuning from the cavity mode lead to a reduction from this value.

1.2.2 Strong Coupling

The strong coupling regime between an emitter and cavity is achieved if cavity photons are reabsorbed by the active medium at a faster rate than they escape the cavity. In this regime the interaction between the emitter and the cavity is reversible as an emitted photon is reabsorbed by the emitter before it escapes the cavity. The coherent reversible transfer of energy between emitter and cavity mode when close to resonance causes an energy splitting called the vacuum Rabi splitting. Experimentally, the strong coupling regime is demonstrated through the observation of this splitting between cavity and emitter in either absorption or reflectivity as a function of detuning and is known as an anticrossing. The Hamiltonian that describes the exciton-photon interaction in a microcavity is given by:

$$H = \sum_k (E_{X(k)} \hat{b}_k^\dagger \hat{b}_k + E_{ph(k)} \hat{a}_k^\dagger a_k + \frac{\hbar \Omega_{Rabi}}{2} (\hat{b}_k^\dagger \hat{a}_k + \hat{a}_k^\dagger \hat{b}_k)) \tag{1.16}$$

where excitons are regarded as bosons with a low enough density to avoid fermonic contributions. $\hat{b}_k^\dagger$ and $\hat{b}_k$ are the exciton creation and annihilation operators with in-plane

wavevector k and $\hat{a}_k^\dagger$ and $\hat{a}_k$ are the photonic creation and annihilation operators. Ω_{Rabi} is the vacuum Rabi splitting and for the case of quantum wells placed at the antinode of the electric field is given by:

$$\hbar\Omega_{Rabi} = \sqrt{\frac{N_{QW}(\hbar e)^2}{2\epsilon m_0 L_{eff}} f_{osc}} \tag{1.17}$$

where N_{QW} is the number of QWs, L_{eff} is the effective cavity length taking into account penetration into the mirrors, and f_{osc} is the oscillator strength of the transition. Diagonalising the Hamiltonian leads to two eigenenergies known as the upper polariton branch (UPB) and lower polariton branch (LPB). The eigenenergies, neglecting dissipation, are given by:

$$E_{UP(k)} = \frac{E_{ph(k)} + E_{X(k)}}{2} + \frac{1}{2}\sqrt{\Delta_k^2 + (\hbar\Omega_{Rabi})^2} \tag{1.18}$$

$$E_{LP(k)} = \frac{E_{ph(k)} + E_{X(k)}}{2} - \frac{1}{2}\sqrt{\Delta_k^2 + (\hbar\Omega_{Rabi})^2} \tag{1.19}$$

where the detuning between the exciton and the cavity mode is given by $\Delta_k = E_{ph(k)} - E_X$. Fig. 1.5(a) shows the anticrossing between the bare cavity mode and exciton energy as a function of detuning leading to the formation of the UPB and LPB. The energy separation between the two branches is at the minimum when $E_{ph} = E_X$ and is given by the Rabi splitting Ω_{Rabi}. Experimentally weak and strong coupling can be differentiated through the characteristic anticrossing of the photon and exciton eigenenergies when tuned through resonance. Fig. 1.5(a) shows the typical crossing behaviour between the cavity energy in the weak coupling regime (dashed line) and the characteristic anticrossing in the strong coupling regime (full lines).

The polariton operators can be written in the systems constituent exciton-photon basis:

$$\begin{pmatrix} p_k \\ q_k \end{pmatrix} = \begin{pmatrix} X_k & C_k \\ -C_k & X_k \end{pmatrix} \begin{pmatrix} b_k \\ a_k \end{pmatrix} \tag{1.20}$$

where $p_k^\dagger$, p_k and $q_k^\dagger$, q_k are the creation and annihilation operators for the lower and

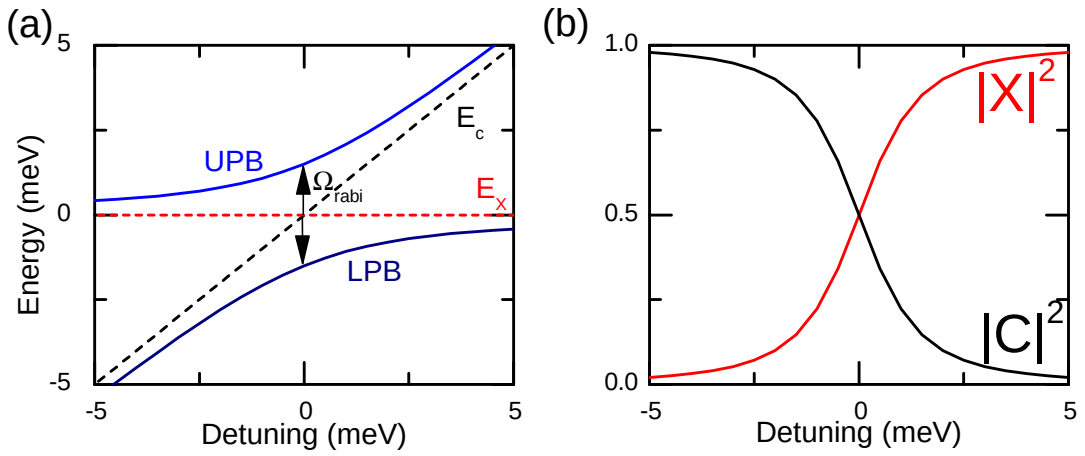

Figure 1.5: (a) Anticrossing between cavity mode (black dashed line) and QW exciton (red dashed line) showing the formation of the UPB (blue line) and LPB (navy blue line) as a function of exciton-photon detuning at k = 0. The Rabi splitting is 3 meV. (b) Hopfield coefficients of the LPB as a function of detuning corresponding to the photonic fraction (red line) and the exciting fraction (black line).

upper polariton. X_k and C_k are the Hopfield coefficients which describe the excitonic and photonic content of the polariton and are given by

$$X_k^2 = \frac{\Delta_k + \sqrt{\Delta_k^2 + (\hbar\Omega_{Rabi})^2}}{2\sqrt{\Delta_k^2 + (\hbar\Omega_{Rabi})^2}}, C_k^2 = -\frac{\Delta_k - \sqrt{\Delta_k^2 + (\hbar\Omega_{Rabi})^2}}{2\sqrt{\Delta_k^2 + (\hbar\Omega_{Rabi})^2}} \tag{1.21}$$

with the condition that $X_k^2 + C_k^2 = 1$ [13]. Fig. 1.5(b) shows the two coefficients for the LPB as a function of detuning. At resonance, $\delta = 0$ meV, the polariton is half-light half-matter while at large detunings the polariton can have much more photonic or excitonic character dependent on whether the detuning is positive or negative. The finite linewidths of both the exciton and photon can be introduced as imaginary components in the Hamiltonian for exciton and photon energies:

$$E'_{X(k)} = E_{X(k)} - i\gamma_X \tag{1.22}$$

$$E'_{ph(k)} = E_{ph(k)} - i\gamma_{ph} \tag{1.23}$$

This can be incorporated into the Hamiltonian that describes the strongly coupled system (Eq 1.16) and leads to the following expressions for upper and lower polariton eigenenergies:

$$E_{UP(k)} = \frac{E_{X(k)} + E_{ph(k)}}{2} - i\frac{\gamma_X + \gamma_{ph}}{2} + \frac{1}{2}\sqrt{(\Delta_k - i(\gamma_X - \gamma_{ph}))^2 + (\hbar\Omega_{Rabi})^2} \quad (1.24)$$

$$E_{LP(k)} = \frac{E_{X(k)} + E_{ph(k)}}{2} - i\frac{\gamma_X + \gamma_{ph}}{2} - \frac{1}{2}\sqrt{(\Delta_k - i(\gamma_X - \gamma_{ph}))^2 + (\hbar\Omega_{Rabi})^2} \quad (1.25)$$

At resonance ($\Delta_k = 0$), this gives us the following condition to observe strong coupling: $(\hbar\Omega_{Rabi})^2 > (\gamma_x - \gamma_{ph})^2$ which gives rise to real energy splitting and polariton branches. When $(\hbar\Omega_{Rabi})^2 < (\gamma_x - \gamma_{ph})^2$ the energy spitting is imaginary and the system is in the weak coupling regime. Further discussion on the linewidths required to observe the anticrossing is given by Savona et al [14]. Here the expression to observe the splitting in absorption was shown to be

$$\hbar\Omega'_{rabi} = \sqrt{(\hbar\Omega)^2 - 2(\gamma_X^2 + \gamma_{ph}^2)} \quad (1.26)$$

and provides a more stringent requirement to observe strong coupling. When $\Omega_{rabi}/2 > \gamma_X^2 + \gamma_{ph}^2$ the system is in the strong coupling regime and when $\Omega_{rabi}/2 < \gamma_X^2 + \gamma_{ph}^2$ the system is in the weak coupling regime. In between these two the system lies in the intermediate coupling regime where the Rabi splitting can be estimated from the coupled oscillator model but cannot be resolved in the experimental absorption spectrum [14].

1.3 Microcavity Polaritons

The first observation of microcavity polaritons is credited to Weisbuch *et al.* (1992) who measured the energy shift of two peaks in reflectivity as a function of detuning [6]. This characteristic anticrossing was correctly attributed to the formation of the upper and

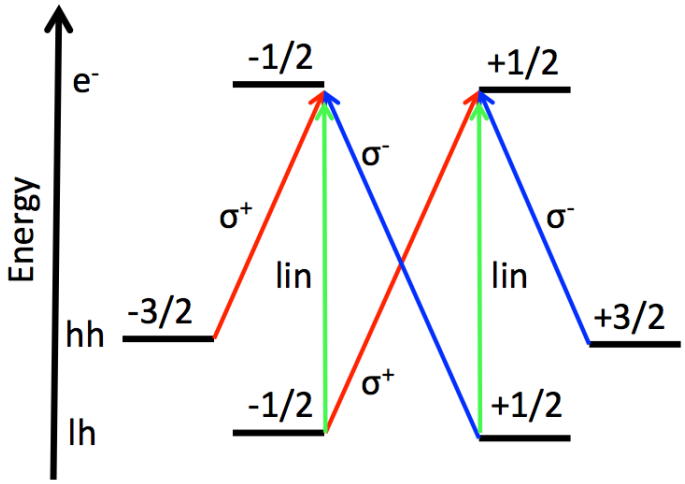

Figure 1.6: Optical transitions in zincblende semiconductor QWs for electrons, light-holes and heavy-holes. Absorption of σ^+, σ^- and linear polarised photons are shown by the red, blue and green arrows.

lower polariton branches due to strong coupling between the GaAs QW exciton and the microcavity photons. Since the pioneering work of Weisbuch *et al.* significant progress has been made in the field of solid state polaritons with the observation of Bose-Einstein condensation [7], superfluid like behaviour [15, 8], and the formation of bright solitons [16]. In this section the basic properties of polaritons will be reviewed, concentrating on the work relevant to the experimental results presented in this thesis.

1.3.1 Polarisation Properties

In GaAs conduction band electrons with s-symmetry have a spin angular momentum $m_j = \pm 1/2$ while valence band holes with p-symmetry have a spin angular momentum of $m_j = \pm 1/2, \pm 3/2$ for light-holes and heavy-holes. Hence the total angular momentum J_z for an exciton can have projections of ± 1 and ± 2 along the growth axis, depending on whether the composite structure is an electron-light-hole or electron-heavy-hole.

Due to angular momentum conservation the absorption of a photon creates an exciton with a spin projection of ± 1, since the photon spin angular momentum is 0 or ± 1. Excitons

with spin $J_z = \pm 1$ are referred to as *'bright states'* as they couple to photons. Excitons with $J_z = \pm 2$ are referred to as *'dark states'* since they do not couple with photons. The bright $J_z = \pm 1$ exciton states couple to the light field emitting and absorbing σ^+ and σ^- polarised photons. The overall polarisation of the macroscopic polariton system can be any superposition of these states and its polarisation is fully represented by the Poincáre sphere and Stokes vector formalism. The Stokes vector is defined as

$$S = \begin{pmatrix} S_0 \\ S_1 \\ S_2 \\ S_3 \end{pmatrix} \tag{1.27}$$

where S_0 is the normalised total intensity. S_1 is the degree of linear polarisation in the vertical and horizontal basis defined by:

$$S_1 = \frac{I_H - I_V}{I_H + I_V} \tag{1.28}$$

where I_H and I_V are the intensities of horizontal and vertically polarised light. S_2 is the degree of polarised light in the diagonal basis:

$$S_2 = \frac{I_{D^+} - I_{D^-}}{I_{D^+} + I_{D^-}} \tag{1.29}$$

where I_{D^+} and I_{D^-} are the intensities of +45° and -45° linearly polarised light. Finally, S_3 is the degree of circular polarisation.

$$S_3 = \frac{I_{\sigma^+} - I_{\sigma^-}}{I_{\sigma^+} + I_{\sigma^-}} \tag{1.30}$$

where I_{σ^+} and I_{σ^-} are the intensities of σ^+ and σ^- circularly polarised light. The Poincáre sphere, shown in Fig. 1.7 is a vectorial representation of the polarisation where each orthogonal axis corresponds to S_1, S_2 and S_3. Fully polarised light corresponds to a unit

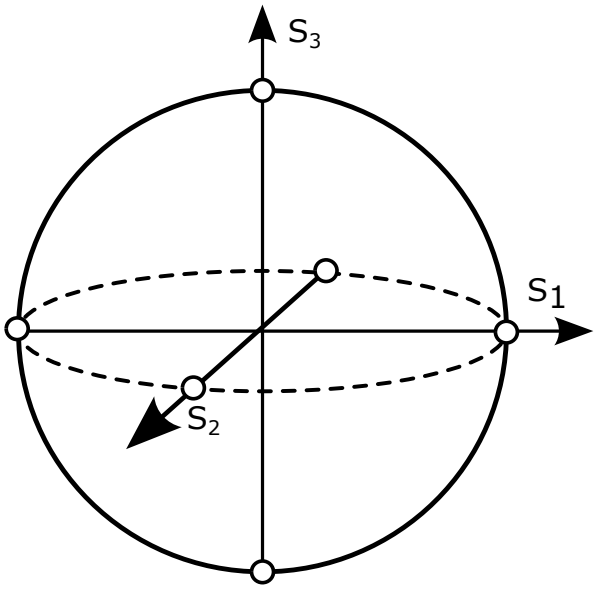

Figure 1.7: Poincare sphere. Each point on the sphere consists of a fully polarised state in the linear (S_1), diagonal (S_2) and circular (S_3) basis. Points which lie within the surface correspond to a partially polarised state.

vector starting in the centre of the sphere and ending at a point on its surface. Partially polarised light is a vector that begins in the centre of the sphere and ends within it, with completely unpolarised light being a zero length vector at the centre of the sphere.

1.3.2 Cavity Dispersion Relation

The presence of a microcavity introduces quantisation of the photon wavevector in the direction of growth. As such the cavity dispersion takes on a 2-dimensional character

$$E = \frac{\hbar c}{n_c \lambda} = \frac{\hbar c k}{n_c} = \frac{\hbar c}{n_c}\sqrt{k_z^2 + k_{||}^2} \tag{1.31}$$

where n_c is the refractive index of the cavity and k_z is the light wavevector in the growth direction and $k_{||}$ is the light wavevector in the perpendicular direction and is given by

$$k_{||} = k \sin\theta \tag{1.32}$$

where θ is the angle between the emitted light and the normal of the cavity surface. Since we have quantisation in the growth direction we can write the dispersion relation as:

$$E_{(k_{||})} = \sqrt{E_z^2 + \frac{\hbar^2 c^2 k_{||}^2}{n_c^2}} \tag{1.33}$$

Since this is parabolic at low $k_{||}$ vectors, we can introduce an effective mass to describe the curvature of the dispersion relation at $k_{||} = 0$:

$$m_{photon} = \frac{n_c h}{\lambda c} \tag{1.34}$$

The polariton effective mass m^*_{pol}, which is inherited from the photon and exciton is also approximately quadratic in the low momentum limit and can be written as

$$E(k_{||}) \approx \frac{\hbar^2 k_{||}^2}{2m^*_{pol}} + E_0 \tag{1.35}$$

Fig. 1.8 shows the bare photon and exciton dispersions (dashed lines). Strong coupling between the two leads to the formation of the UPB and LPB (solid lines) with a separation at $k = 0$ given by the Rabi splitting. The polariton effective mass is typically $\approx 10^{-4} m_e$ due to the low inherited effective mass of the cavity photon. This low effective mass, along with the low density of states is a key reason polariton condensation can be observed at relatively high temperatures and low densities. Polariton condensation is discussed in more detail below.

1.3.3 Polariton Relaxation

The dispersion relation of polaritons introduces complicated relaxation dynamics due to the variation in density of states as well as a change in the interacting excitonic component as a function of wavevector and detuning. Non-resonant excitation of a microcavity produces a population in the electron-hole continuum at high energies above the UPB as

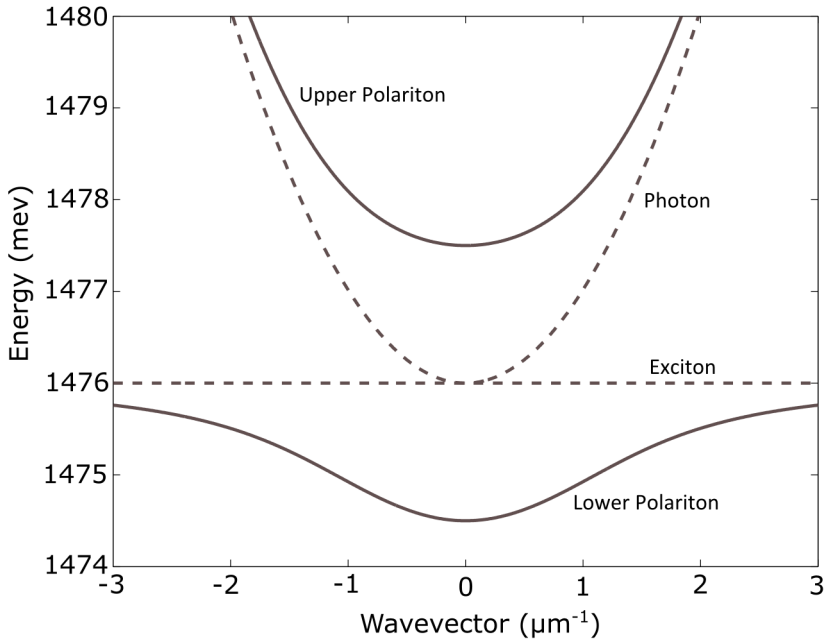

Figure 1.8: Plotted dispersion for photons (upper dashed line) and exciton (lower dashed line) in a microcavity in resonance. The full lines show the UPB and LPB formed in the strong coupling regime with $\Omega_{Rabi} = 3$ meV.

shown in Fig. 1.9. These electron-holes relax to the UPB branch through LO phonon scattering before scattering with acoustic phonons to high momentum exciton states on the exciton dispersion. Further relaxation through acoustic phonon scattering occurs along the dispersion to the LPB. At low momentum states the excitons enter the strong coupling region and form polaritons.

Under low excitation powers, in the strongly coupled region, the dominant relaxation mechanism of polaritons is polariton-polariton scattering in contrast to the relaxation along the *dark* region where polariton acoustic-phonon scattering dominates. The *dark* region of the polariton dispersion is characterised by the area in which the in-plane polariton momentum $k_{||}^{pol}$ is greater than that of a free photon within the microcavity $k_{||}^{phot}$. In the dark region conservation of momentum dictates that the exciton states cannot emit a photon and the relaxation time of ≈100 ps is much shorter than the exciton-like lifetime of around 1 ns [17]. Excitons and polaritons at high wavevectors must undergo relaxation in order to reach the strongly coupled bright region. In order do so the excitons must dissipate around 5-10 meV. A comprehensive theoretical description of relaxation of non resonantly pumped microcavities can be found in Tassone *et al.* (1997) where a semi-classical treatment describes scattering events through rate equations. The main result of this is that the main polariton-phonon scattering event is most efficient when the energy of the phonon is around 1 meV which corresponds to a phonon wavelength of 10 nm, the typical size of a QW in the growth direction, and has a scattering time of around 10 ps. As such several of these events are required to allow relaxation from the bottleneck region to the ground state.

The larger photonic character of the polaritons with decreasing in-plane momentum significantly reduces the polariton lifetime. In the strongly coupled region at low momentum states the opposite is true and the polariton lifetime in this *bright* region becomes comparable to the polariton-phonon time. At a particular in-plane momentum, k_{bot}, the polariton leakage rate is faster than acoustic phonon scattering (≈ 10 ps) preventing ther-

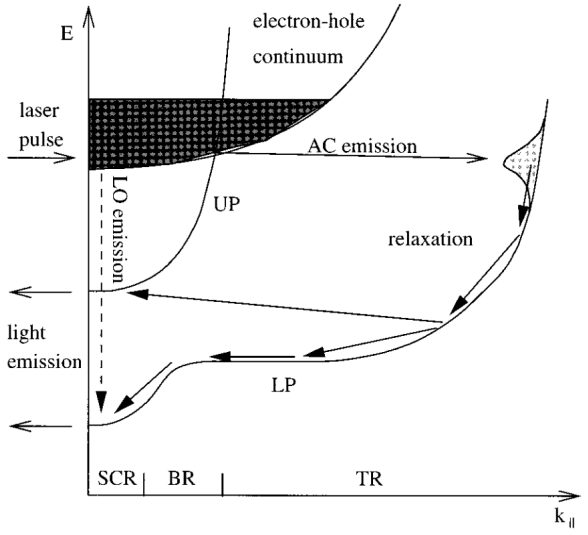

Figure 1.9: Figure taken from [17]. Schematic representation of the polariton dispersion. Non-resonant laser excitation excites the electron-hole continuum which scatter to high k-states on the LP branch through acoustic phonon emission. Relaxation along the LP branch then occurs in the thermal region (TR) until the bottle neck region (BR)is reached where the lifetime is less than the scattering time preventing large accumulation at low k-states in the strong-coupling regime (SCR).

modynamic equilibrium from being reached and the efficient relaxation of polaritons to $k = 0$. Simultaneously, at low in plane momentum states the LPB energy density of states decreases steeply slowing the relaxation of polaritons through acoustic phonon emission. The two mechanisms combine to cause build-up of the polariton population at k_{bot} and is known as the bottleneck effect [17, 18]. The shorter lifetime of the polariton in this region prevents this relaxation to the ground state from occurring. Instead, relaxation to the ground state must occur through a small number of high energy scattering events, which are much less efficient. This effect is amplified in negatively detuned microcavities where the steeper LPB dispersion requires a larger number of scattering events to reach the ground state.

At higher excitation power the polariton density becomes much higher and inter-particle scattering mechanisms begin to determine the relaxation dynamics. In polariton-polariton scattering a 2-body polariton interaction leads to one polariton gaining energy and mo-

mentum and scatters further into the dark region while the second polariton loses this energy and momentum and relaxes down the polariton dispersion to a lower momentum state eventually to the ground state. Alternatively polaritons can relax via polariton-free carrier scattering. Here a free carrier removes energy and momentum from the polariton allowing it to move to lower momentum states on the dispersion. This process is 10x more efficient than polariton-polariton scattering and occurs on much shorter timescales [17].

A number of methods exist to suppress the bottleneck effect and will be briefly discussed here. Positively detuned samples do not exhibit the bottleneck effect due to the increased polariton lifetime caused by the higher exciton component of the LPB. This leads to a very shallow LPB so significantly less scattering events are required to reach the ground state. Alternatively, high power non-resonant excitation can be used to inject a large exciton density leading to significantly increased scattering to the ground state. When the system is pumped strongly under non-resonant excitation, rather than observing stimulated scattering to the ground state, a saturation effect can be observed. Carriers that have not relaxed to the optically active region form an electron-hole plasma as the Mott density is reached. This causes a screening of the coulomb interactions between electrons and holes. Consequently, these states become 'bleached' and the strong coupling is lost [19, 20]. Above this saturation density the emission is primarily via the weakly-coupled cavity mode. If the excitation density is high enough, population inversion can occur leading to conventional stimulated emission and photonic lasing. In many cases the polariton condensation occurs at exciton densities smaller than the Mott density, followed by bleaching of the strong coupling regime and photonic lasing at high power.[21] Finally resonant excitation can inject polaritons at any required k-vector or can be used to inject polaritons into the ground state through optical parametric oscillations (OPO) which relies on stimulated polariton-polariton scattering [22, 23].

The strong polariton-polariton interactions are 3-4 orders of magnitude larger than the

photon-photon interaction in for example silicon due to a Kerr nonlinearity. This interaction has led to the observation of a number of nonlinear effects such as solitons [16], superfluid-like behaviour [8] and OPO at moderate excitation power. Potentially this strong polariton-polariton interaction can be applied to study quantum correlated gases such as the Tonks-Girardeau and Mott insulator states. In this case structures which laterally confine polaritons are required.

1.3.4 Low Dimensional Polaritons

The introduction of lateral confinement in microcavities leads to discretisation of the polariton energies and dispersion. Several systems have been developed to achieve lateral confinement based on excitonic or photonic confinement. In this case the dimensionality of the polaritons can be reduced from 2-dimensional to 1-dimensional in microwires and 0-dimensional in polariton boxes. This removes the translational symmetry and quantises the polariton dispersion in the confined directions.

Spatial modulation of the polariton potential can be introduced using single or cross propagating surface acoustic waves (SAWs) leading to 1 and 2- dimensional confinement. Currently the lateral size is limited to around 8 μm by the small penetration into the microcavity at higher SAW frequencies [25, 26]. The application of controlled stress can be used to spatially localise the exciton wavefunction through using a tip pushing on the backside of the microcavity creating a potential trap. Here the energy dispersion spectra remains a quasi-continuum due to weak confinement [27, 28]. Alternatively, polaritons of reduced dimensionality can be achieved through confinement of their photonic component. This has been demonstrated through depositing and patterning a thin metal strip on the top of a cavity. Metallic strips or discs modulate the cavity mode energy through inducing a shallow potential on the polariton states [29, 30]. Alternatively, mesa structures can be defined by etching the cavity layer before depositing the top Bragg mirror. The mesa region has a larger cavity thickness and forms a 0-dimensional cavity with full discretisation

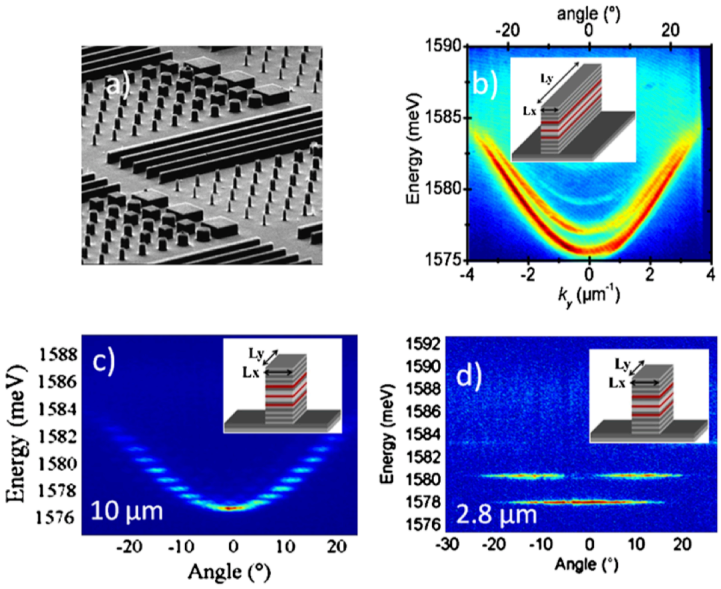

Figure 1.10: Figure taken from [24]. (a) SEM image of an array of micro wires and micropillars etched from a planar microcavity. (b) Polariton emissions from a microwire showing the formation of 1-dimensional subbands. (c) 10 μm micropillar dispersion (d) 2.8 μm micropillar dispersion.

of the photon and thus, the polariton energies [31]. Interestingly, these systems offer the coexistence of both 0-dimensional discrete polariton states in the mesa and a 2-dimensional polariton continuum in the planar surrounding region. Lateral photonic confinement can also be achieved through fully etching a planar cavity into wires or pillars where polariton discretisation is obtained through total internal reflection at the sidewall - air interface. In this case the translational invariance of the polariton states is lost and the in-plane wavevector, k_x, becomes quantised by $k_x = \frac{p\pi}{L_x}$, where L_x is the lateral length in the x-direction and p is an integer. In one direction this leads to the splitting of the polariton states into 1-dimensional subbands in the y-direction as shown in Fig. 1.10 (b). Etching in 2-dimensions leads to the formation of micropillars where the in-plane wavevector is quantised in both x and y-directions [32]. As a result micropillar polaritons form discrete states with a mode spacing that depends upon the micropillar size. The mode degeneracy is determined by the micropillar geometry which can be square or circular leading to different eigenmode profiles. Finally, full photonic confinement can be employed through

the use of photonic crystals [33]. Typically micropillars and photonic crystal microcavities suffer from increased losses due to surface recombination and increased sidewall scattering as the dimensions are reduced and in all mentioned cases the spectral tuning of the cavities is extremely limited.

1.4 Tunable Cavities

Conventionally, microcavities are grown via Molecular Beam Epitaxy (MBE) leading to planar Fabry-Perot type cavities. In order to control the exciton-photon detuning, rotation-stop is used during the cavity region growth before the top DBR is grown. This leads to a gradient in the cavity thickness across the sample allowing the detuning to be varied by simply measuring a piece from different locations on the wafer.

Recently, in situ spectral tunability in microcavities has been demonstrated based upon open cavity systems. Here, the top and bottom DBRs are grown separately and mounted onto nanopositioner stacks as shown in Fig. 1.11. The separation between the two mirrors is then controlled, allowing full spectral tunability. The top mirror in these systems is a concave DBR in order to introduce lateral photonic confinement and limit the effect of beam walk-off due to poor parallelism between the mirrors. To date the concave DBRs have been fabricated using two main methods; laser ablation and focused ion beam (FIB) milling.

In laser ablation a high power CO_2 laser is focussed onto the surface of either an optical fiber or flat substrate [35, 36, 37]. The strong absorption of the 10.6 μm laser light within the first few microns of the surface allows controlled melting of the sample. At high laser intensity, the removal of the material is dominated by evaporation and shapes the depression with very low surface roughness due to surface tension in a thin molten layer on the surface [38]. Using this approach cavities were developed that demonstrated strong coupling with single quantum dots (QDs) [39]. To date, the minimum RoC, which

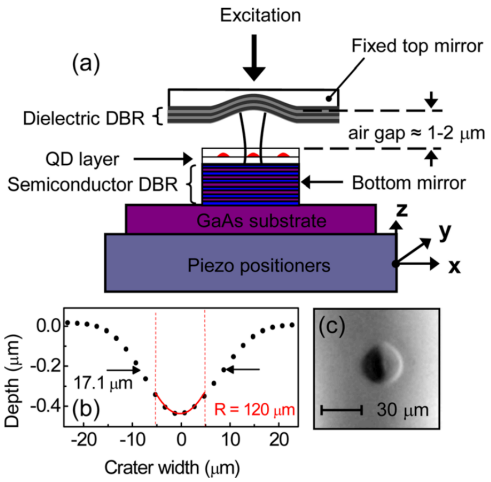

Figure 1.11: Figure taken from [34]. Schematic of an open cavity system with QDs embedded in the cavity region. (a) The top DBR is a dielectric concave feature. The bottom DBR is a semiconductor DBR with a cavity region containing Stranski-Krastonov QDs at the antinode of the E-field. The bottom sample can be tuned using XYZ-nanopositioners allowing full spatial and spectral tuning. (b) Profile of concave DBR before DBR coating. Fabricated using laser ablation. The RoC of the spherical section is 120 μm. (c) Microscope image of the concave DBR.

determines the degree of photonic confinement, achieved using laser ablation is 10 μm [40].

Focused ion beam (FIB) milling, in contrast to laser ablation, allows concave features to be milled into silica substrates with much smaller radii of curvature [41]. In this thesis, the smallest RoC used is 5.6 μm as this is close to the limitation imposed by the stability condition that $L < RoC$ for stable resonator modes, although smaller RoCs of 3 μm have been demonstrated in literature [41]. The ability to fabricate small features, arises from the small lateral size of the gallium beam of $\sim$ 5 nm. To create the concave feature a gallium beam is used to mill the silica substrate. By varying the dwell time per pixel concave depressions with surface roughnesses of $\sigma_{rms} = 0.7$ nm can be milled. Due to the small radii of curvature, mode volumes down to $2 - 4$ μm^3 could be achieved. The flexibility of this fabrication method lends itself nicely to the fabrication of more complex cavities such as coupled cavities which are studied in this thesis and has the potential to

fabricate 1-dimensional chains and 2-dimensional arrays of coupled cavities.

A number of alternative fabrication methods have been demonstrated such as using wet etching approaches where arrays of concave mirrors are fabricated in silicon substrates by isotropically wet-etching through circular apertures in a lithographic mask using a mixture of HF and HNO_3 in acetic acid. In this case the RoC remained relatively large $\sim 185\mu m$ [42]. Steinmetz *et al.* (2006) deposited mirrors onto silicon micro lenses before transferring them to fiber tips using a lift-off technique [35]. Finally, Cue *et al.* (2006) used trapped bubbles in glass to produce spherical surfaces before coating with dielectric layers achieving radii of curvature of $\sim 50\mu m$ [43].

1.5 Polariton Condensation

Polaritons are composite bosons and as such obey Bose-Einstein statistics in the low density regime. In the case of integer-spin bosons, the wavefunction is symmetric under particle exchange, causing constructive interference between probability amplitudes of particles in the same state. This leads to an enhanced probability that two different particles will be found in the same quantum state. This is known as bosonic stimulation where the transition rate of a bosonic particle in a quantum state is proportional to $N + 1$ where N is the number of particles already in the state. In the low density limit excitons have been shown to act as good bosons and this is inherited by their polariton counterparts. Hence it is possible for polaritons to undergo bosonic stimulated scattering leading to macroscopic occupation of the ground LPB state at k = 0, known as polariton condensation.This section provides an overview of Bose-Einstein (BEC) in a historic context before reviewing the more recent developments in polariton condensation.

1.5.1 Bose-Einstein Condensation

The demonstration of BEC in dilute atomic gases in 1995 [44, 45] has led to a flurry of interest, both theoretically and experimentally, in highly degenerate quantum gases in both atomic and solid state systems. The initial studies of the quantum mechanical properties of massless Bose particles were carried out by S.N. Bose in 1924 [46], leading to the development of the field now known as photon statistics. This work was extended by A. Einstein in 1925 to a system of non-interacting massive Bose particles where the basic idea of BEC was presented [47]. The BEC phase transition arises from the quantum statistics of Bose particles and leads to the macroscopic occupation of the lowest quantum energy state at high particle densities. The energy distribution of N non-interacting bosons at a temperature T in a volume R^d where R is the system size and d is the dimensionality is given by the Bose-Einstein distribution function:

$$f(k,T,\mu) = \frac{1}{e^{\frac{E(k)-\mu}{k_B T}} - 1} \tag{1.36}$$

where μ is the chemical potential and is the energy required to add a particle to the system. By defining a temperature, T, we have assumed that the system is in thermal equilibrium and has a finite density.

The total particle number can be written as

$$N(T,\mu) = \sum_k f(k,T,\mu) = \frac{1}{e^{\frac{-\mu}{k_B T}} - 1} + \sum_{k\neq 0} f(k,T,\mu) \tag{1.37}$$

where the particles in the ground state $E, k = 0$ are separated from the uncondensed particles.

The particle density is then given by integrating over reciprocal space

$$n(T,u) = \lim_{T\to\infty} \frac{N(T,\mu)}{R^d} = n_0 + \frac{1}{(2\pi)^d} \int_0^\infty f(k,T,\mu)\,\mathrm{d}k \tag{1.38}$$

where the ground state density is given by

$$n_0(T,\mu) = \lim_{R\to\infty} \frac{1}{R^d} \frac{1}{e^{\frac{-\mu}{k_b T}} - 1} \tag{1.39}$$

For nonzero μ, there is no ground state occupation and the ground state density is zero. Increasing the chemical potential also increases the particle density. The maximum particle density that the system can accommodate before occupation of the ground state is known as the critical density and is given by

$$n_c(T) = \lim_{\mu\to 0} \frac{1}{(2\pi)^d} \int_0^\infty f(k,T)\,\mathrm{d}k \tag{1.40}$$

Analytical solutions of this equation reveal that there is convergent behaviour for d $>$ 2 and divergent behaviour for d $\leq$ 2. This tells us that in a system with two or less dimensions the system can accommodate an infinite number of particles, while for a system with 3 dimensions, the chemical potential becomes zero when the critical density is reached. Increasing the density above this leads to accumulation of particles in the ground states. The ground state density is finally given by

$$n_0(T) = n(T) - n_c(T) \tag{1.41}$$

This is characterised by a phase transition where increasing the particle density leads to macroscopic occupation of the ground state and can be described by a single coherent wavefunction.

For over ten years, the proposal by Einstein remained an entirely theoretical phase transition for a fictitious system of non-interacting Bose particles. Independently in 1938 P. L. Kapitza [48] and J. F. Allen and A. D. Misener [49] discovered superfluidity in liquid helium-4. In the same year F. London presented the intuitive idea that superfluidity could be a manifestation of BEC. [50] Linking the superfluidity of strongly interacting helium-4

with the BEC of a non-interacting ideal gas studied by Einstein was carried out in 1947 by N. N. Bogoliubov who presented the first microscopic theory of interacting Bose gases in the context of BEC [51]. At a similar time, L. D. Landau developed a phenomenological theory of superfluidity in terms of the excitation spectra of the helium-4 liquid [52] which was later supported both experimentally and by the full microscopic theory developed by R. P. Feynman [53]. Despite the initial successful development of a theoretical understanding of superfluidity, it was not until the experimental realisation of atomic BEC in 1995 that the theoretical concepts proposed by A. Einstein [47] and N. N. Bogoliubov [51] were confirmed.

1.5.2 Polariton Condensation

In 1996, A. Imamoglu proposed that exciton-polaritons, as composite bosons, should undergo a form of BEC [54]. Due to very low effective mass inherited from their photonic component, polaritons were expected to undergo the BEC phase transition at cryogenically accessible temperatures. Furthermore, polaritons overcome problems associated with achieving an exciton-BEC such as localisation and inhomogeneous broadening via their spatially extended wavefunctions. By increasing the number of QWs inside a microcavity, the exciton density per QW can be significantly reduced while keeping the same polariton density allowing large particle densities to be reached without undergoing a transition to an electron-hole plasma. Due to the photonic component of polaritons the effective mass is very small $\approx 10^{-4} m_e$ which results in a critical temperature of $\approx 10K$. These temperatures are easily achieved using conventional liquid helium cryogenics and hence polaritons provided the first observation of condensation behaviour in the solid state [7]. As discussed in the previous section it is forbidden for a 2-dimensional non-interacting bosonic system to undergo Bose-Einstein condensation. Instead, a weakly interacting Bose gas such as a polaritonic system can undergo quasi-condensation at temperature below the Berezinskii-Kosterlitz-Thouless transition temperature T_{BKT}. In this case the condensate

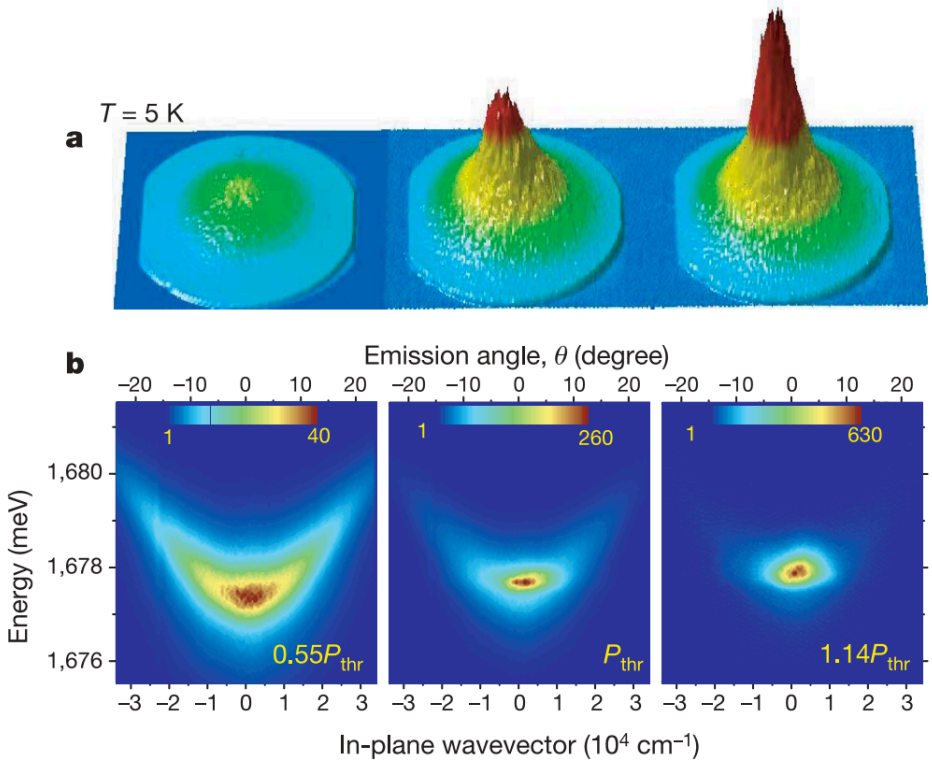

Figure 1.12: Figure taken from [7] (a) Momentum space distribution of the LPB as a function of non-resonant excitation power in a 16 CdTe QW microcavity. (b) Angular resolved spectra showing the accumulation of ground state polaritons above threshold.

wavefunction does not exhibit macroscopic coherence that is infinite in extent, as is the case of a BEC, but instead decays slowly according to a power law rather than exponentially [55]. The first non-ambiguous demonstration of polariton BEC was carried out by J. Kasprzak et al. [7] using a 16 QW Cd-Te microcavity. The authors directly measured the ground state occupation as a function of non-resonant pump power, deduced from angular resolved spectroscopy. Above a threshold power P_{th} the emission becomes confined to a narrow angular range centred at $k = 0$ as shown in the famous plots of Fig. 1.12. Other signatures of polariton condensation were observed such as a phase transition from unpolarised emission below P_{thr}, to linearly polarised emission above P_{thr}. Long range spatial coherence over the entire pump spot was observed above P_{thr}, whereas below threshold the spatial coherence only extended over the thermal de Broglie wavelength. Polariton

BEC has since been observed in GaAs based microcavities [56, 57] as well as at room temperature in wide bandgap materials such as ZnO [58, 59] and GaN [60, 61] and organics [62, 63]. However, a polariton condensate is not strictly a standard BEC for two main reasons: It is generated by final-state stimulation through phonon and polariton-exciton scattering and is not necessarily in thermal equilibrium with the phonon bath. Secondly, the polariton condensate is non-equilibrium in nature due to the finite polariton lifetime, since polaritons couple to the external photonic field due to leakage through the microcavity mirrors.

Since the initial demonstration of polariton condensation the field has blossomed with the advent of superfluid hydrodynamics in these systems [15]. Further significant experimental achievements followed, such as Josephson oscillations [64], Bogoliubov excitations [65, 66], quantised vortices [67], dark solitons [68, 69] and bright solitons [16]. The above effects can be theoretically described by mean field approximations, whereas quantum effects are yet to be addressed experimentally. Significantly, quantum polaritonic effects based upon the interaction of single polaritons have not yet been observed due to the small single polariton-polariton interaction strength of around 9 μeV.μm^2 [32].

1.6 Polariton Blockade

Polariton blockade is a nonlinear optical process where a microcavity emits a stream of nonclassical single photons due to the nonlinear polariton-polariton interaction preventing the injection of a second polariton into the cavity. The first prediction of a single photon nonlinear process was by Imamoglu *et al.* (2007) [70] and is known as 'photon blockade', in analogy with the Coulomb blockade effect [71, 72].

Consider a a single mode cavity with an optical nonlinearity U and cavity linewidth γ where, $U > \gamma$. Under resonant excitation when the cavity is in a two-photon state the cavity mode is spectrally shifted by U which moves out of resonance with pumping

resonant laser frequency ω_0. Hence only a single photon can be injected at a time, i.e the presence of a single photon within the cavity prevents the injection of a second photon. In transmission this leads to a strongly antibunching single photon source. The experimental demonstration of polariton blockade depends strongly on the magnitude of the polariton-polariton interaction strength, which arises from the coulomb interaction between their constituent excitons.

1.6.1 Polariton-Polariton Interaction

Polaritons interact with each other through their exciton component which causes polariton-polariton scattering in resonantly pumped microcavities. The polariton-polariton interaction comes from the coulomb interaction between their constituent exciton components [73]. Ciuti et al. (1998) have shown that the scattering of excitons is strongly spin dependent where the scattering between excitons of the same composite spin is allowed, and the scattering between excitons of opposite spins is only possible via the dark exciton states [74]. The spin dependent interaction was then shown to be repulsive for polaritons with the same spin and attractive for polaritons with opposite spins, where the attractive interaction is significantly weaker than the repulsive [73]. Overall this leads to a repulsive interaction for polaritons which is experimentally manifested as a blueshift in the LPB energy at high polariton densities. The polariton-polariton interaction has a theoretical value of around 3 μeV.μm^2, given by $\approx 3a_bE_B$, where a_b and E_B are the exciton Bohr radius and binding energy [74]. Experimental estimates of the interaction strength in micropillars yield a value of 9 μeV. μm^2 [32].

1.6.2 Conventional Polariton Blockade

Conventional polariton blockade describes polariton blockade in a single cavity. Verger *et al.* (2006) proposed a nonclassical light source based upon the nonlinearity in polariton systems that arises from the polariton-polariton interaction. In this theoretical proposal

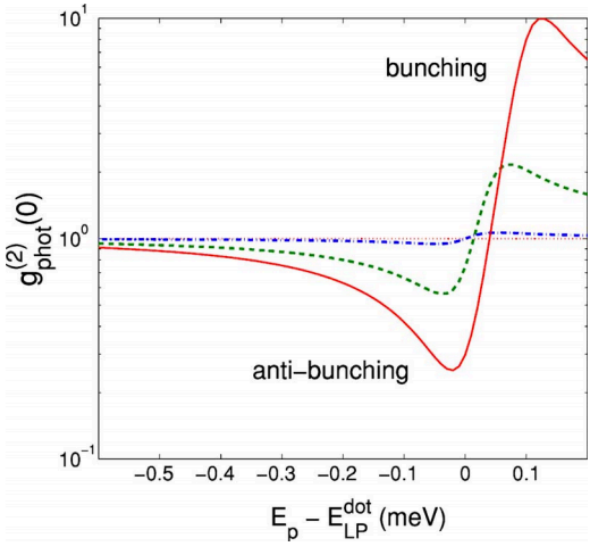

Figure 1.13: Figure taken from [76]. Second-order coherence function $g^{(2)}(0)$ plotted versus resonant laser pump detuning for three difference cavity-exciton detunings. Solid 5 meV; dashed 0 meV; dotted-dashed -5 meV.

3-dimensional polariton confinement is introduced into the photonic component leading to a polariton dot. Such confinement increases the polariton-polariton interaction due to the increased overlap of their exciton wavefunctions. This small interaction is in contrast to the comparatively large inhomogeneously broadened lower polariton linewidths of $\gamma = 80$ μeV that can be experimentally achieved [75]. The large discrepancy between the interaction and the linewidth make it difficult to experimentally achieve $U > \gamma$ and demonstrate a polaritonic single photon source.

1.6.3 Feshbach Blockade

In recent years significant advances have been made in the field of strongly correlated atomic gases due to the Feshbach resonance effect in atomic collisions [77]. The Feshbach resonance is the increase in scattering cross-section observed when the energy of two interacting atoms is resonant with a molecular state.

The possibility of utilising an analogous Feshbach resonance to increase the polaritonic

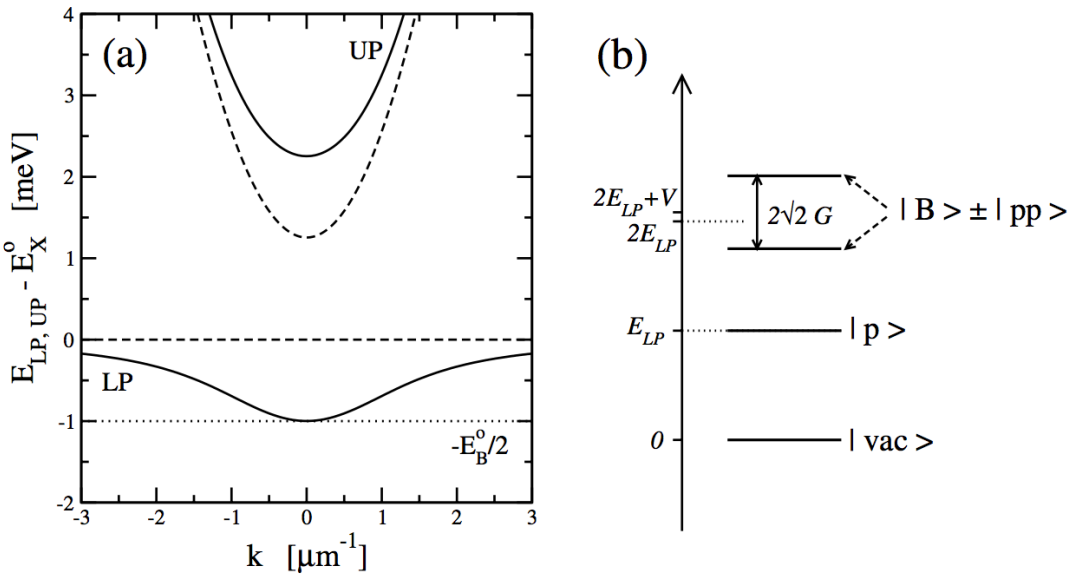

Figure 1.14: Figure taken from [79]. (a) The solid lines display the UPB and LPB dispersions. The dashed lines indicate the bare cavity and exciton energies. The detuning is set so that the ground state of the LPB is in resonance with the biexciton energy (horizontal dotted line). (b) Schematic diagram of the energy states at the Feshbach resonance depicted in (a).

optical nonlinearity in microcavities was proposed where the intermediate molecular state is provided by the biexciton state [78]. When the LPB is in resonance with the biexciton state a nonlinear shift of $\sqrt{2}G \approx \hbar\Omega_R a_B/L$ is expected, as shown in Fig. 1.14 [79]. This interaction can be used to generate a source of antibunched photons. Recently, the polaritonic Feshbach resonance was observed in GaAs/AlAs microcavity containing a single 8 nm $In_{0.04}Ga_{0.96}As$ QW [80]. In this work, a σ_+ pump and σ_- probe were applied with zero delay. The transmitted probe beam was measured to reveal the energy shift and amplitude variation of the lower polariton resonance due to the presence of the polariton pump population, as a function of exciton-photon detuning. When the energy of two lower polaritons passes through the biexciton resonance a characteristic dispersive shape is observed in the energy shift, a feature of resonant scattering. The energy shift is shown to switch from a redshift to a blueshift, demonstrating the modification of the interaction

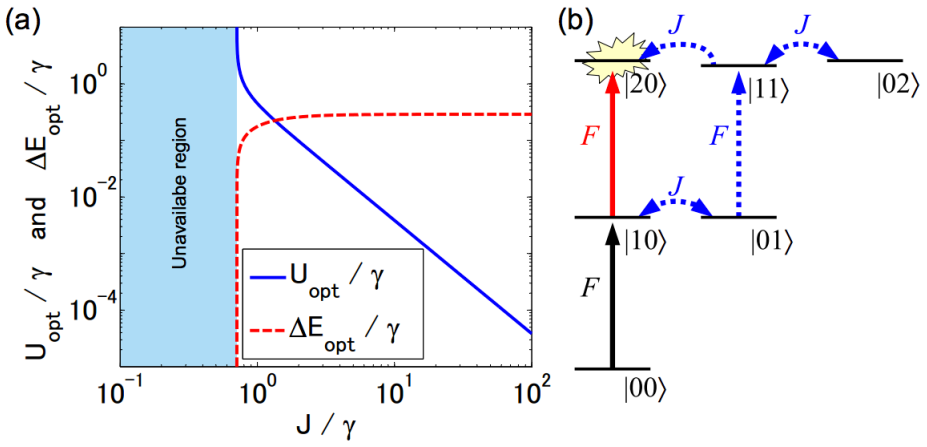

Figure 1.15: Figure taken from [5]. (a) Optimal nonlinearity U_{opt} and detuning ΔE_{opt} as a function of coupling strength J. Perfect antibunching is obtained $J > \gamma/\sqrt{2}$. (b) Transition paths between states in the coupled cavity configuration. The direct excitation path from $|10\rangle$ to $|20\rangle$ is forbidden due to interference with the path drawn by the dotted arrows.

between pump and probe polaritons from attractive to repulsive.

1.6.4 Polariton Blockade in Coupled Cavities

The previous sections on blockade require that the nonlinearity U exceeds that of the loss rate given by the lower polariton linewidth γ_{LP}. Recently, an analytical study of a resonantly pumped cavity coupled to a non-pumped auxiliary cavity showed that strong antibunching can be obtained with only a weak Kerr nonlinearity $U << \gamma$ [81] due to a subtle quantum interference effect. The underlying mechanism for the nonclassical photon statistics was revealed using a wavefunction amplitude approach by Bamba *et al.* (2011) [5]. Fig. 1.15(b) shows the cavity energy levels with tunnelling between two coupled cavities where $|mn\rangle$ represent the Fock state with m particles in the pumped cavity and n particles in the second cavity. Perfect antibunching can be achieved for an optimal set of parameters. Assuming equal energy and loss rates of the two coupled cavities are in perfect resonance and have the same linewidth, the authors calculate the optimal parameters of

the interaction strength U and the pump laser detuning $\Delta E = E - \hbar\omega_p$ to be [5]:

$$\Delta E_{opt} \approx \frac{\gamma}{2\sqrt{3}} \qquad U_{opt} \approx \frac{2}{3\sqrt{3}}\frac{\gamma^3}{J^2} \tag{1.42}$$

For $J \gg \gamma$, this directly implies that $U_{opt}/\gamma \ll 1$. This is due to destructive interference between the amplitudes of the two transition paths as shown in Fig. 1.15. This quantum interference is between the two-photon injection path ($|10\rangle \rightarrow |20\rangle$), and the tunnelling transition between the two cavities ($|10\rangle \leftrightarrow |01\rangle \rightarrow (|11\rangle \leftrightarrow |02\rangle) \rightarrow |20\rangle$). For certain values of the U and ΔE, the two above transition paths have opposite phases and equal amplitudes, leading to full destructive interference. The relaxation on U/γ required to observe photon blockade comes at the expense of an oscillatory $g^{(2)}(\tau)$ function. The characteristic scale of the oscillations is determined by the cavity-cavity tunnelling rate $J \gg \gamma$. As a result of the fast timescales involved, a streak camera with a temporal resolution of around 2 ps will be required to observe the antibunching along with coupled cavities with tunnelling times that exceed this resolution.

In this thesis a tunable open access cavity is presented where 3-dimensional confinement of the photonic mode is introduced from the hemispherical cavity geometry with open optical access for both real and k-space imaging. This system is suitable for the observation of polariton blockade based upon the proposal of Bamba *et al.* (2011), combining strong lateral confinement, in order to increase the polariton-polariton interaction, with high Q-factors and tunable photonic molecules with tunnelling times that allow experimental measurement of the photon autocorrelation function.

Chapter 2

Development of an Open Cavity System

2.1 Introduction

This Chapter outlines the development of a tunable cavity system. The open cavity consists of two independent nanopositioner stacks that allow the positioning of two mirrors. When the two mirrors are brought together a microcavity is formed where full tunability of the spectral resonance is achieved through control of the separation along with full xy-spatial positioning of the mirrors. The formed cavity is a hemispherical resonator. A complete review of the Gaussian optics required to fully describe the optical modes within the hemispherical cavity is presented. Finally, two 10 paired SiO_2/TiO_2 dielectric DBRs were fabricated and used to form a hemispherical cavity where the top mirror has a concave shape with a radius of curvature of 25 μm. Reflectivity studies are then performed at low temperature demonstrating the formation of stable modes with Q-factors of up to 7,000 and a mirror separation of around 1 μm.

2.2 Motivation

The open cavity system was designed to meet a number of criteria:

- Free space coupling of optical excitation and collection.
- Spectral tuning of the cavity resonance through fine control of the cavity length.
- Spatial tuning through translational positioning in the xy-directions of both mirrors.
- Operation at cryogenic temperatures (4K).
- High Q-factor and small mode volume.
- Isolation from mechanical vibration.

The application of such a system in the field of polariton physics comes from the ability to arbitrarily select the exciton-photon detuning along with the strong lateral photonic confinement which is present in hemispherical microcavities. This confinement increases the exciton wavefunction overlap for a given excitation density, increasing the polariton-polariton interaction. Furthermore, the versatility of the system allows the incorporation of unconventional emitters simply through placement of a foreign emitter on the surface of the planar mirror such as exfoliated metal dichalcogenides [82] and colloidal quantum dots (QDs) [83].

A goal of this thesis was to demonstrate a system with strong lateral confinement of exciton polaritons and high Q-factors. As such a demonstration of strong coupling along with submicron beam waist sizes is required. As discussed in Section 1.6.2 in order to observe polariton blockade a significant increase in the single polariton-polariton interaction is required. This can be achieved through increasing the overlap of the exciton wavefunction through lateral confinement - leading to a stronger interaction. Conventional systems which have lateral confinement include micropillars, mesas and photonic crystals. In all cases the ability to decrease the dimensions below a few microns is limited by surface recombination and quenching of the QW exciton which leads to significant degradation of

the polariton linewidth. Furthermore, the ability to select a particular detuning *in-situ* through tuning of the cavity resonance is limited to the growth of a cavity wedge in micropillars and mesas and limited to temperature tuning and gas absorption in photonic crystals. A truly tunable system, where the exciton-photon detuning can be selected with ease, would allow the excitonic component to be selected arbitrarily. Both of these criteria are achieved by using a tunable open cavity with a hemispherical geometry. The open nature allows full tunability of the spectral resonance through control of the mirror separation, while the hemispherical geometry introduce lateral confinement into the photonic component which is then inherited by the polaritonic wavefunction. Using this method unprecedented lateral sizes can be achieved using radii of curvature below 15 μm where the confinement is submicron and approaches the diffraction limit for decreasing radii of curvature.

2.3 Cavity Housing Design

The open cavity system allows independent nanopositioning of both top and bottom mirror in the xyz-directions. The top piezo stacks consists of three Attocube Ltd closed loop nanopositioners, ANPx51/RES for xy positioning and ANPz51/RES for z positioning. The bottom piezo stack consists of two ANPx101/RES for xy nanopositioning and an ANPz101/RES for z-movement. The tilt of the bottom mirror can also be controlled using two goniometer stages (ANGp101/RES and ANGt101/RES). All of the piezo nanopositioners have resistive readout that allows their position to be known to an accuracy of ±200nm. The range of travel of ANP51 and ANP101 nanopositioners is 3mm and 5mm respectively and the ANGt and ANGp goniometer nanopositioners have travel ranges 6.6° and 5.4°. Applying a DC voltage (0-70V) across the nanopositioners allows sub-nm positioning of the piezos for fine tuning of the mirror position. The system is presented in Fig. 2.1 showing the assembled insert (a) that corresponds to the schematic shown in Fig. 2.2, along with the bottom sample holder (b), the custom mounted objective (Thor-

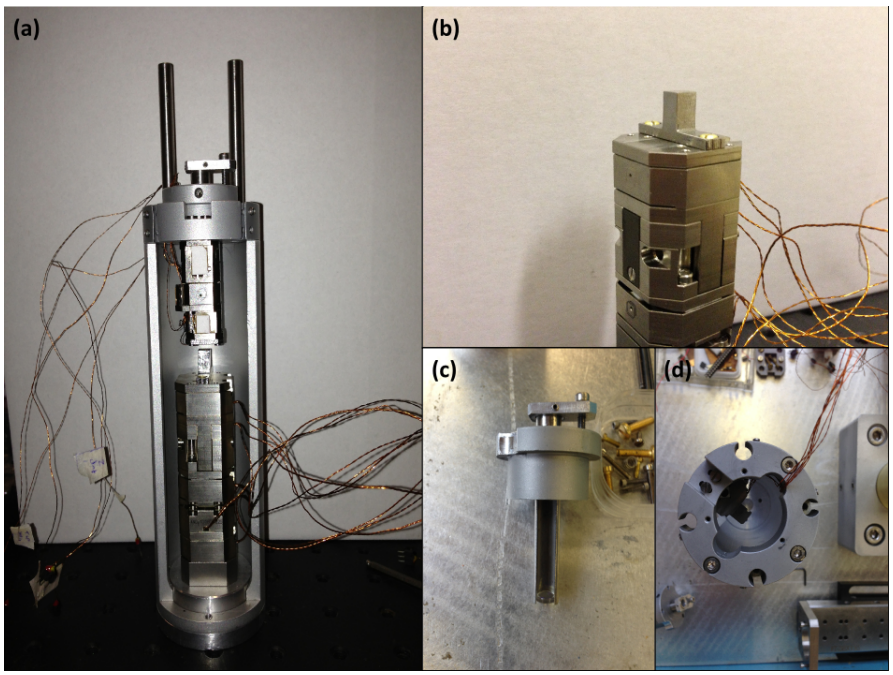

Figure 2.1: (a) Open cavity insert with two independent nanopositioner stacks. (b) Bottom nanopositioner stack with custom titanium sample holder. (c) Height adjustable lens tube. (d) View along optical path showing the top sample holder.

labs NA=0.55 aspheric B-coated) with tunable height (c) and the optical path with the lens removed showing the top sample holder (d). The nanopositioners are fixed in a rigid titanium housing to isolate the cavity from mechanical noise. These low frequency noise-induced vibrations are minimised to ensure that the cavity length is not changed through longitudinal vibrations. Furthermore the rigidity of the cavity insert ensures that it has a high resonant frequency so there is a minimal response to mechanical vibration. Both the piezo nanopositioners and the sample holders are also made from titanium to minimise any difference in thermal contraction during cool down to cryogenic temperatures. Finally, a small titanium platform (11mm) is used beneath the bottom piezo stack to raise the bottom sample holder into the range of movement of both sets of the piezo positioners.

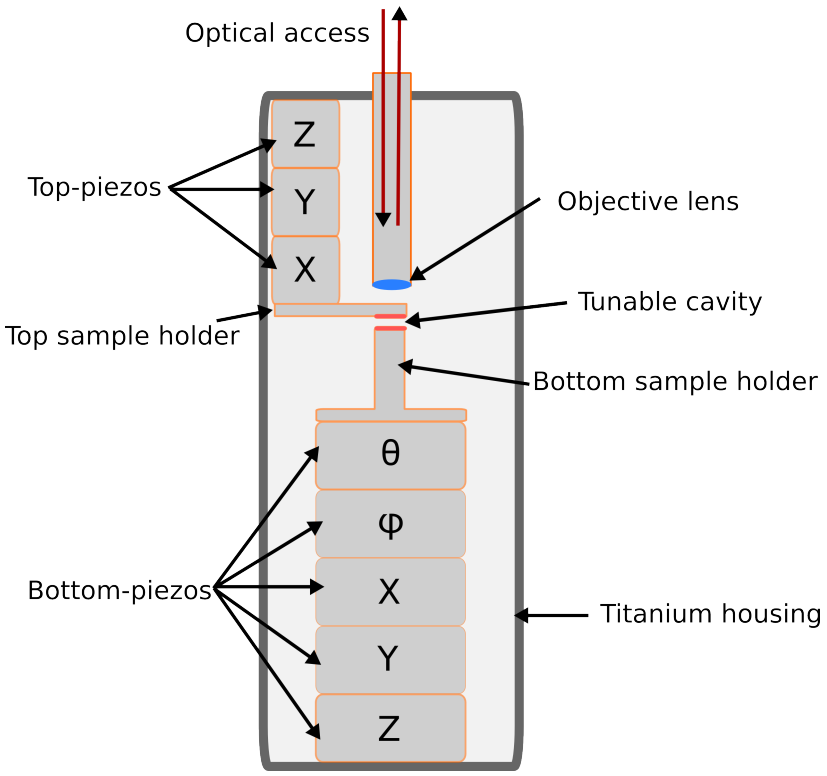

Figure 2.2: Schematic diagram of the open cavity system. Independent xyz-movement of the two mirrors is performed using two separate Attocube nanopositioner stacks. Two goniometer ϕ and θ nanopositioners allow control of the tilt angle of the bottom sample. The system is housed in a titanium enclosure to minimise differences in thermal contraction when cooled to low temperature. Optical access to the cavity is provided through a 0.55NA objective lens.

2.4 Hemispherical Cavities

In an open cavity system the two mirrors are grown separately before being brought together to form a tunable microcavity. Such a system is not limited to a standard monolithic planar-planar Fabry-Perot microcavity since the cavity is no longer fabricated by molecular beam epitaxy (MBE). Instead the cavity can be formed by a planar bottom mirror and a concave top mirror which forms a hemispherical microcavity. This section briefly outlines the mode profiles in such a resonator and how lateral photonic confinement can be introduced. This lateral confinement also allows higher Q-factor cavity modes to

be used as the resonator quality is not as dependent on perfect parallelism between the top and bottom mirrors as in the planar case, as beam walk-off is minimised.

2.4.1 Gaussian Modes

In order to describe the electric field profile within a hemispherical resonator the full wave nature of light must be considered. The scalar wave equation for an electric field in a vacuum is written as

$$\nabla^2 E(r,t) - \frac{1}{c^2}\frac{\partial^2}{\partial t^2}E(r,t) = 0 \tag{2.1}$$

where $E(r,t)$ is the E-field and c is the speed of light. The most trivial solution to Maxwells equations is a monochromatic plane wavefunction with an angular frequency ω

$$E(r,t) = E(r)e^{-i\omega t} \tag{2.2}$$

Inserting this into the the scalar wave equation leads to the scalar time dependent *Helmholtz equation*:

$$\nabla^2 E(r) + k^2 E(r) = 0 \tag{2.3}$$

where the wavevector is given by

$$k^2 = \frac{\omega^2}{c^2} \tag{2.4}$$

A number of solutions exist for the *Helmholtz equation* such as $E(\mathbf{r}) = E_0 e^{i\mathbf{k}.\mathbf{r}}$ for a unidirectional plane wave or $E(\mathbf{r}) = \frac{1}{r}e^{i\mathbf{k}.\mathbf{r}}$ for a spherical wave with $r = \sqrt{x^2+y^2+z^2}$. Assuming a trial solution of the form $E(\mathbf{r}) = E_0(\mathbf{r})e^{ikz}$ for small divergence angles the paraxial wave equation can be shown to be

$$\nabla_\perp^2 E(\mathbf{r}) + 2ik\frac{\partial E(\mathbf{r})}{\partial z} = 0 \tag{2.5}$$

Here $\nabla_\perp^2$ is the transverse Laplacian given by $\nabla_\perp^2 = \frac{\partial^2}{\partial x^2} + \frac{\partial^2}{\partial y^2} + \frac{\partial^2}{\partial z^2}$. A rigorous derivation of the paraxial wave equation can be found in *Laser Physics* (1986) [84]. The complete

solution of this partial differential equation takes the form:

$$E(\mathbf{r}) = \frac{Ae^{ikz}e^{i\phi(z)}}{\sqrt{1+z^2/z_R^2}} e^{ik(x^2+y^2)/2R(z)} e^{-(x^2+y^2)/w^2(z)} \tag{2.6}$$

which describes a Gaussian beam characterised by the beam waist, $\omega(z)$, the radius of curvature of the phase profile $R(z)$ and the Guoy phase shift $\phi(z) = \tan^{-1}(z/z_R)$. The beam waist has a minimum value ω_0 at the focus of the Gaussian beam. The distance z_0 is defined such that $\omega(z_R) = \omega_0\sqrt{2}$. This E-field distribution describes freely propagating waves without the influence of confinement due to the formation of cavities.

In the case of a hemispherical cavity consisting of a planar mirror and a concave mirror the E-field profile must satisfy Gaussian mode profiles modified from the freely propagating case due to confinement. Here the mirror radius of curvature imposes boundary conditions on the mode where the beam phase front must match the curvature of the mirror. In this case the minimum beam waist of the mode will lie on the planar mirror so long as the stability condition $L < RoC$ is met, where L is the mirror separation. This can be generalised to the case of different types of resonators through the resonator parameter g:

$$g_i = 1 - \frac{L}{RoC_i} \tag{2.7}$$

which defines the stability condition for a cavity consisting of two mirrors $i = 1, 2$ as $0 \geq g_1 g_2 \leq 1$. For a hemispherical cavity the second mirror is planar so for this case $g_2 = 1$. The dependence of the beam waist on each of the mirrors can be written as

$$\omega_1 = \left(\frac{\lambda L}{\pi}\right)^{1/2} \left(\frac{R}{L_{eff}} - 1\right)^{-1/4} \tag{2.8}$$

$$\omega_0 = \left(\frac{\lambda L}{\pi}\right)^{1/2} (L_{eff}R - L_{eff}^2)^{1/4} \tag{2.9}$$

where ω_1 is the beam waist on the curved mirror and ω_0 the beam waist on the planar

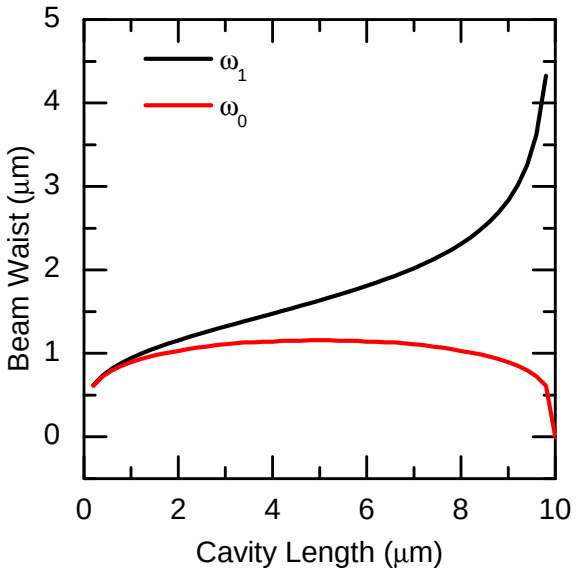

Figure 2.3: Gaussian beam waists for a hemispherical cavity as a function of cavity length. The radius of curvature of the concave mirror is 10 μm.

mirror. Fig. 2.3 shows the simulated beam waists on the mirrors as a function of cavity length for a concave mirror with RoC = 10 μm. The beam waist on the planar mirror is approximately constant at around 1 μm while ω_1 diverges as the length approaches the unstable resonator regime $L = R$ and modes become unstable. For very short cavity lengths $L \leq 3$ μm there is very little divergence between the two beam waists and $\omega_0 \approx \omega_1$. The degree of photonic confinement in a hemispherical microcavity is determined by the beam waist size, which is in turn determined by the radius of curvature and the cavity length. In the study of polaritons, the degree of lateral confinement is determined by the beam waist size on the quantum well, which is located in a cavity region on the planar mirror. Therefore, the degree of polaritonic confinement is determined by ω_0. Fig. 2.4 shows the planar mirror beam waist at a cavity length of 1 μm as a function of the concave mirror radius of curvature. For radii of curvature of less than 15 μm the expected beam waist size on the planar mirror is submicron in size, with significant reduction in ω_0 for small RoC down to ≈ 0.5 μm for a hemispherical cavity with a 2 μm radius of curvature top mirror. As discussed in Section 1.6.2, in order to increase the polariton-polariton

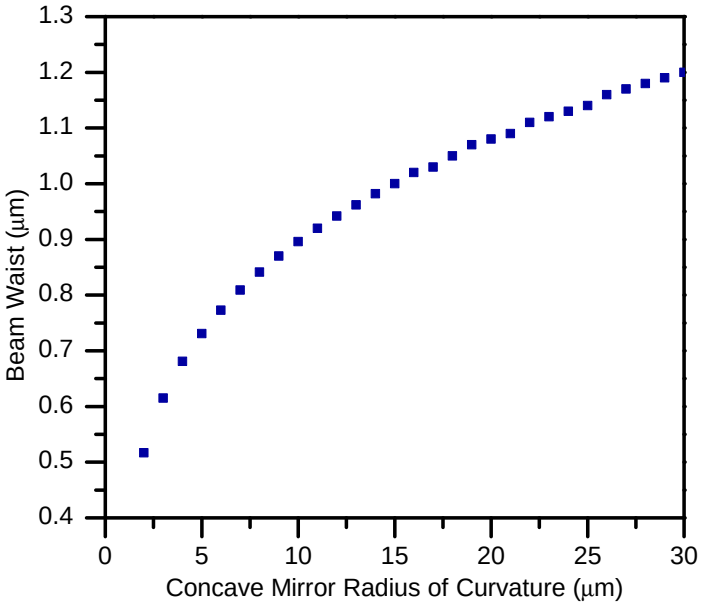

Figure 2.4: Beam waist on the planar mirror in a hemispherical cavity as a function of concave mirror radius of curvature. The cavity length is set to 1 μm. The submicron lateral confinement regime is achieved for R $\leq$ 15 μm.

interaction, lateral polariton confinement can be used. Here, by using a hemispherical microcavity with a concave mirror with a radius of curvature of less than 15 μm, submicron lateral photonic confinement can be achieved. Since in a polaritonic system the QW lies in a cavity region near the surface of this mirror, the photonic confinement is inherited by the polariton, leading to submicron polariton confinement. By using a system based upon a hemispherical cavity, one avoids any etching of the QW which can lead to degradation of polariton linewidth due to surface recombination and quenching of the exciton as seen in micropillars.

Cavity Eigenfrequencies

The eigenfrequencies of a cavity resonator are given by:

$$\nu_{qmn} = \frac{c}{2n_{cav}L}\left(q + (m+n+1)\frac{\cos^{-1}(\pm\sqrt{g_1 g_2})}{\pi}\right) \tag{2.10}$$

where n_{cav} is the cavity refractive index, q is the longitudinal mode index, m and n are the transverse Gaussian mode indices. For a hemispherical cavity, as presented in this thesis, the second mirror is planar so $g_2 = 1$. The longitudinal and transverse mode spacings then follow and are given by:

$$\Delta\nu = \frac{c}{2n_{cav}L}\Delta q \qquad\qquad \Delta\nu_T = \frac{c}{2n_{cav}L}\frac{\cos^{-1}\sqrt{g}}{\pi}(\Delta m + \Delta n) \tag{2.11}$$

where Δq, Δm and Δn are the differences in longitudinal and transverse Gaussian mode indices.

2.4.2 Gaussian Mode Profiles

The previous Section presented the mathematical description of Gaussian beams and its application to hemispherical resonators. The final discussion presented the idea of transverse Gaussian modes appearing for certain resonances which are quantified by the transverse indices m and n. These higher order modes can be accounted for in the solution to the paraxial wave equation through the inclusion of additional structure in the x-y plane. The general solution in the xy basis is given by

$$E(\mathbf{r}) = AF_x\left[\frac{x}{\omega_0}\right]F_y\left[\frac{y}{\omega_0}\right]e^{iP(z)}e^{ik(x^2+y^2)/2q(z)} \tag{2.12}$$

where F_x and F_y are functions of $\frac{x}{\omega_0}$ and $\frac{y}{\omega_0}$, and A is a constant. After some manipulation and separation of variables we get the second order differential equation [84]:

$$\frac{d^2F}{du^2} - 2u\frac{dF}{du} + \frac{c}{2}F = 0 \tag{2.13}$$

where the variable u is a function of x or y and $\omega(z)$, and c is a constant. The solutions of this second order differential equation are given by the Hermite polynomials H_{mn}. We can then write the electric field of the Hermite-Gaussian modes as:

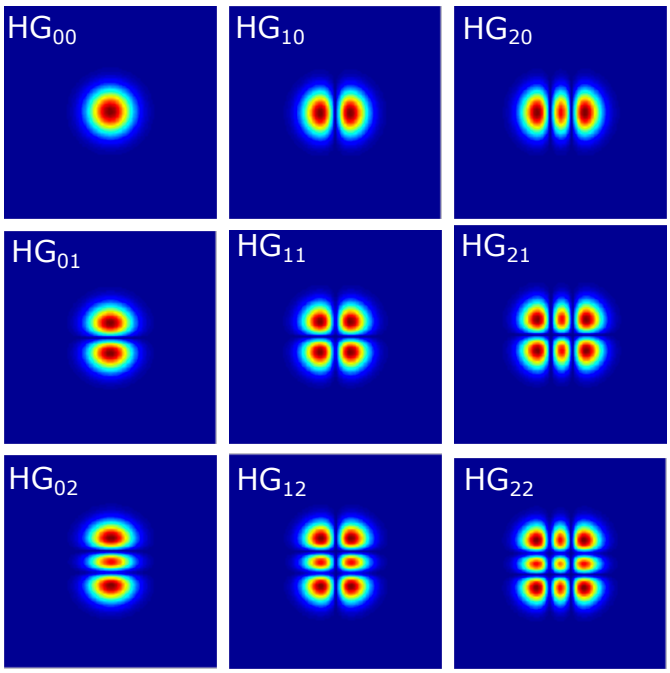

Figure 2.5: E-field profiles for the first 9 Hermite-Gaussian beams HG_{mn}.

$$E_{m,n}(r) = E_0 \frac{\omega_0}{\omega(z)} H_m\left[\frac{\sqrt{2}x}{\omega(z)}\right] H_n\left[\frac{\sqrt{2}y}{\omega(z)}\right] e^{i(kz-(m-n-1)\tan^{-1}(\frac{z}{z_0}))} e^{(ik(\frac{r^2}{2R(z)})-\frac{r^2}{\omega_z^2})} \tag{2.14}$$

where the transverse indices m and n indicate the Hermite polynomial order. The electric field profile of the first 9 TEM_{mn} modes are plotted in Fig. 2.5. Transverse modes with equal $|m+n|$ are degenerate. In physical systems this degeneracy is often broken due to a slight asymmetry in the cavity structure.

If we choose to solve the paraxial wave equation in cylindrical coordinate basis instead of choosing the Cartesian xy-coordinate basis, we can obtain alternative transverse mode profiles based on cylindrical symmetries. Using a suitable trial solution gives us the second order differential equation:

$$\left(\frac{\partial^2}{\partial r^2} + \frac{1}{r}\frac{\partial}{\partial r} + \frac{1}{r^2} + 2ik\frac{\partial}{\partial z}\right) E_{r,\phi.z} = 0 \tag{2.15}$$

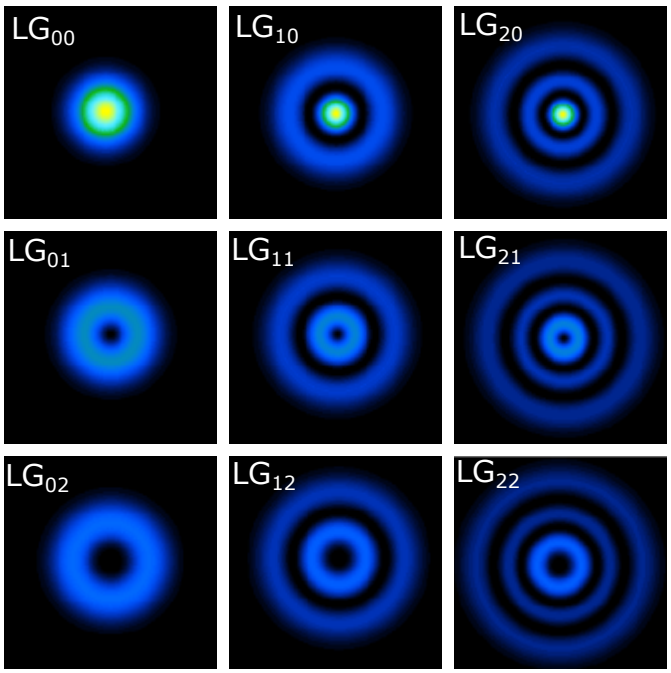

Figure 2.6: E-field profiles for the first 9 helical Laguerre-Gaussian modes $LG_{\rho l}$

The solutions are given by the associated Laguerre polynomials L_p^l. The E-field of the Laguerre-Gaussian modes is given by:

$$E_{l\rho}(r,\phi,z) = E_0 \frac{\omega_0}{\omega(z)} e^{il\phi} \left(\frac{r\sqrt{2}}{\omega(z)}\right)^{|l|} L_p^{|l|}\left[\frac{2r^2}{\omega(z)^2}\right] e^{\frac{-r^2}{\omega(z)^2}} e^{\frac{ikr^2}{2R(z)}} e^{-i(2p+l+1)\tan^{-1}(\frac{z}{z_0})} \tag{2.16}$$

The first 9 Laguerre-Gaussian mode profiles are plotted in Fig. 2.6. Transverse modes with equal $|2l+p|$ are degenerate in energy. For LG_{lp} modes with $l \geq 1$ the transverse mode carries orbital angular momentum with a phase rotation given by $2\pi l$ leading to phase vortices.

Both the Hermite-Gaussian and Laguerre-Gaussian modes provide a complete set of transverse modes in their respective basis and can be written in terms of each other. Experimentally the boundary conditions of the photonic structure determines the observed mode profiles; for a cylindrically symmetric cavity such as a cylindrical micropillar or mesa,

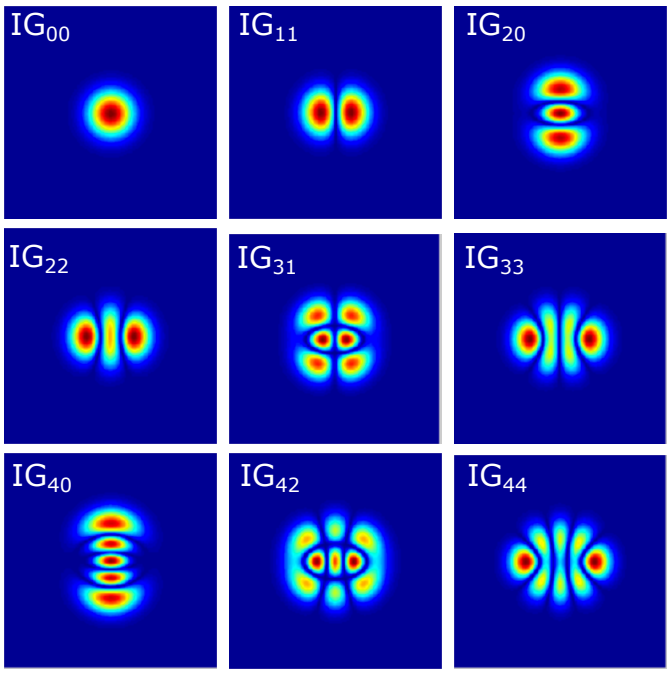

Figure 2.7: E-field distributions for a selection of even Ince-Gaussian beams.

Laguerre-Gaussian modes would be expected, while for a square micropillar, Hermite-Gaussian modes would be expected. In reality perfectly cylindrical systems are difficult to fabricate and Laguerre modes are often not observed. Instead elliptically symmetric Mathieu- or Ince-Gaussian modes are observed which are the solution to the paraxial wave equation in an elliptical basis, as seen in mesa structures [85]. A selection of the Ince-Gaussian modes are plotted in Fig. 2.7 in the elliptical basis.

2.4.3 FDTD Models

In the previous discussion on Gaussian modes, perfectly reflecting mirrors were assumed. In reality the cavities studied in this work consist of DBR mirrors where there is significant penetration of the E-field into the DBR mirrors. In this section the hemispherical cavity is modelled using MEEP, an open FDTD software package, in order to extract expected values for photonic Q-factors and beam waist sizes on the planar mirror. Fig. 2.8(a) shows the geometrical structure used in the FDTD analysis. The top mirror is a concave feature

with radius of curvature of 5.6 μm and a diameter of 4 μm. Simulations were calculated in a cylindrical geometry where the 2-dimensional grid presented in Fig. 2.8(a) has complete rotational symmetry. This significantly reduces the computational requirements in comparison to a full 3-dimensional simulation. The grid resolution was chosen to be 5 nm in order to accurately model the concave mirror curvature and the DBR layer thicknesses. The refractive indices of the DBR layers were chosen to be 1.4 for the low index SiO_2 and 2.05 for the high index TiO_2. The silica substrate refractive index was chosen to be 1.54. Each DBR has 10 repeats of alternating high and low index quarter wave stacks. These values are representative of the values used in the fabricated mirrors.

For the initial simulation, the separation between the two mirrors was chosen to approximately set the longitudinal mode within the cavity stopband at a distance of around 1 μm. A single simulation with a broadband excitation source placed at the surface of the planar DBR was used to excite the cavity modes and a harmonic inversion technique used to output the mode energy and Q-factors [86]. The simulation was then performed a number of times with a narrow energy source to individually excite the modes to identify the longitudinal resonance. The resonances of the cavity have relatively high Q-factors so decay at a much slower rate then the transient electromagnetic field from the excitation source. Once sufficient time has passed for these transient fields to decay, typically around 2 or more decay times ($\tau = Q/\omega$), the electromagnetic field within the cavity can be assumed to have single frequency harmonic time dependence and the field profile fully represents the excited single cavity mode. Once identified, simulations were then run iteratively to fine tune the cavity mode resonance close to the centre of the stopband at 650 nm. A final simulation with a small grid size of 5 nm was used to output the electromagnetic field of the longitudinal mode. Fig. 2.8(b) shows the z-component of the E-field with narrow band excitation of the longitudinal mode. The Q-factor of the mode is 8031 and was extracted using *Harminv* [86] after the E-field at the surface of the planar mirror had decayed to 10^{-3} from its initial value. The profile shows the focusing effect introduced by the hemispherical geometry where the wavefront at the surface of the concave feature matches the

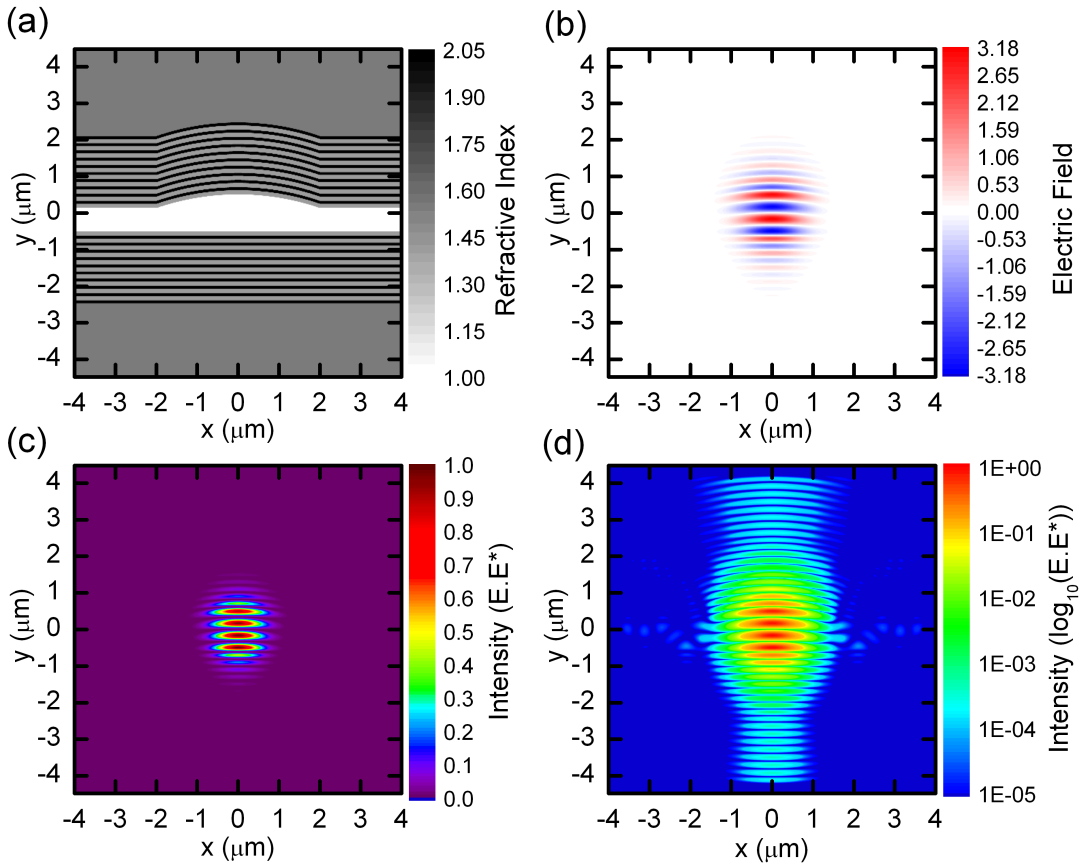

Figure 2.8: (a) Dielectric structure of the hemispherical cavity with 5.6 μm radius of curvature and 4 μm diameter. The separation between the mirrors is 1.05 μm. The resolution of the simulation was set to 5 nm. (b) Electric field component in z-direction after excitation of the longitudinal mode close to the centre of the cavity stopband at 649.1 nm. The Q-factor of the mode is 8031. (c) Electric field intensity ($E.E^*$). (d) Electric field density for the longitudinal mode plotted on a logarithmic colour scale ($log_{10}(E.E^*)$).

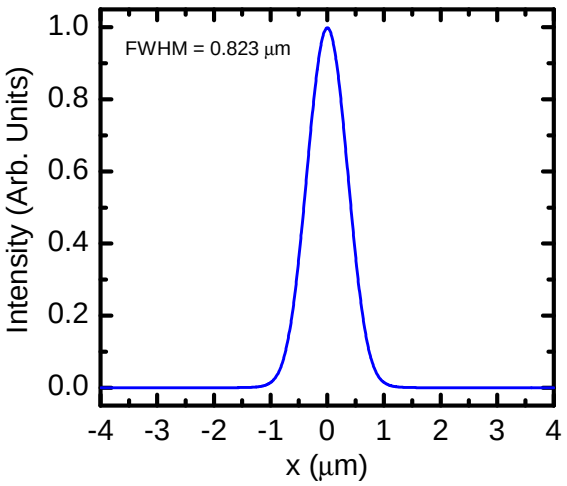

Figure 2.9: Lateral extent of electric field intensity at the surface of the bottom DBR. The FWHM of the Gaussian fit is 0.823 μm.

curvature of the concave DBR. This is focused to a smaller lateral extent on the bottom planar mirror where the wavefronts become parallel to the planar DBR layers.

The electric energy density is plotted in Fig. 2.8(c) on a linear scale showing the strong localisation of the electric field within the cavity and emphasises the strong lateral confinement introduced in the cavity. Fig. 2.8 (d) shows the energy density plotted on a logarithmic scale. Clear leakage of the electric field is occurring into the cavity formed between two planar mirror areas. This is attributed to the sharp discontinuity between the concave region and the planar region leading to scattering into side propagating modes. In the experimental cavities it is currently unclear how the interface forms between the planar and concave regions but can be reasonably expected to play a role in the maximum cavity Q-factors that can be reached in open hemispherical cavities. The beam waist of the electric field at the surface of the planar DBR extracted from the FDTD model is shown in Fig. 2.9. The profile can be fitted with a Gaussian function and has a FWHM = 0.831 μm. The Gaussian beam waist, $\omega_0 = \mathrm{FWHM}/\sqrt{2\ln 2}$, has a value of 0.7057 μm which is comparable to the value of 0.7 μm calculated in the previous section in the Gaussian beam approximation.

2.5 Cavity Design

The tunable cavity consists of two separately grown DBR mirrors. The top concave structure is a dielectric DBR fabricated with $\lambda/4n$ alternating layers of SiO_2 and TiO_2 with refractive indices of 1.4 and 2.1 respectively. The layer thickness is controlled to give maximum reflectivity at a particular wavelength. For the initial demonstration of the open cavity in reflectivity this was at 650 nm and 10 DBR pairs. In the later Chapters in this thesis discussing work with polaritons the QW material varies between $In_{0.04}Ga_{0.96}As$ and $GaAs$ so concave DBR mirrors with stop bands centred at 840 nm and 780 nm were fabricated to match the QW exciton energy.

2.5.1 Concave Mirror Fabrication

The fabrication of the concave mirrors was performed by Dr A. Trichet of the Photonic Nanomaterials Group at the University of Oxford. Fabrication of the concave DBR structures consists of a two step process [41]. Firstly, an array of concave mirrors is produced using focused ion beam (FIB) milling of a silica substrate. A gallium ion beam is focused onto a silica substrate to eject material and mill into the surface. By varying the dwell time as a function of position, the ion beam mills concave features into the surface of the silica substrate. The ability of the FIB approach to produce high quality - low surface roughness templates for DBR mirrors relies on the ability to focus the gallium ion beam down to 5 nm. The rms surface roughness of the uncoated concave depressions is <0.7 nm. On a single chip, multiple concave mirrors are produced with varied parameters of radii of curvature. The radii of curvature of the concave depressions are measured using AFM after the milling process. The planar fused silica substrates have lateral dimensions of 5x5x1 mm. This leads to a large area of redundant surface since the milled array is only around 400x400μm. This redundant portion of the substrate can be detrimental in achieving very small mirror separations of a few microns as the edges of the substrate can come into contact with the bottom sample first. A large surface area also increases

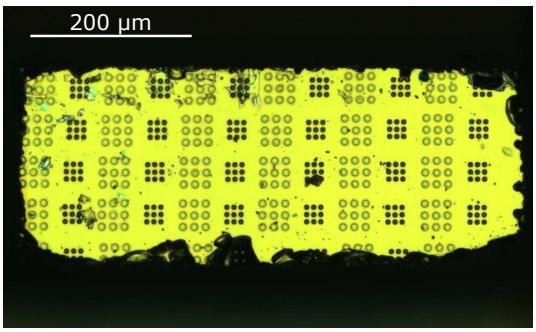

Figure 2.10: Microscope image of the concave depression after DBR coating. The radius of curvature of the two sizes is 12.5 µm and 25 µm.

the probability of large particulates being in the cavity which prevent small mirror separations from being reached. The solution to this was to utilise a silicon dicer to remove these large planar areas and create a plinth around 500x500x500 µm at the centre of the sample. A microscope image of the fabricated sample is shown in Fig. 2.10 showing the array of concave features on a 500x300 µm plinth. A full description of the fabrication can be found in Dolan *et al.* (2010) [41] and in the thesis of Dr. P. R. Dolan [87].

2.6 Low Temperature Demonstration

The initial demonstration of the tunable open cavity was carried out at low temperature - ensuring the maximum stability of the attocube nanopositioners. Fig. 2.10 shows an optical image of the top sample consisting of multiple 3x3 arrays of concave mirrors with radii of curvature of 25 µm and 12.5 µm. The bottom mirror was a planar dielectric mirror leading to a hemispherical cavity. The DBR mirrors have a coating of 10 pairs of SiO_2/TiO_2. The two mirrors were mounted on the two independent attocube nanopositioner stacks. Before being placed in a bath cryostat dipstick, a room temperature alignment procedure was performed. The tube was then pumped to vacuum before being flushed with a small amount of He exchange gas. Finally the system was cooled in a He Dewar lowering the system temperature to around 4K. A small optical table was then attached to the top of the system allowing optical access to the tunable cavity through a glass window. White light

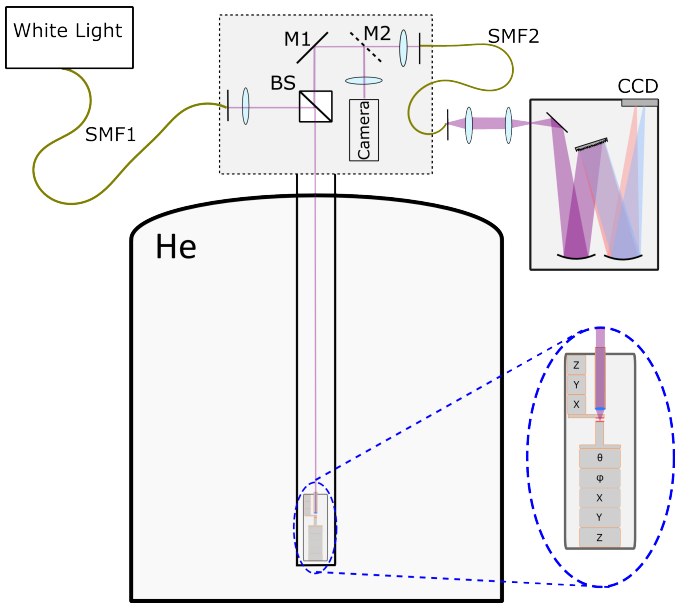

Figure 2.11: Low temperature reflectivity experimental set-up. White light coupled through a single mode fiber (SM1) before being collimated and sent to the cavity using a 50:50 beam splitter (BS). The reflected signal is collected by a single mode fiber (SM2) before being imaged onto the slits of a spectrometer. The inset shows the open cavity insert.

reflectivity was performed using a Bentham WS100 white light source which is coupled to a single mode fiber. The white light was fibre coupled to the optical table before being collimated and sent down the optical path to a 0.55NA aspheric objective using a 50:50 beamsplitter and focused onto one of the 25 µm RoC concave mirrors as shown in Fig. 2.11. The spot size was around 2 µm and centred on the concave mirror in order to maximise the coupling into the longitudinal resonance of the cavity. The reflected signal was collected using a single mode fibre before being focused onto a 0.75m spectrometer with a spectral resolution of 50 µeV. The reflected signal was optimised at 700 nm, rather than at the centre of the stopband of 650 nm, since the white light source intensity decreases sharply below 700 nm. The initial focus of the excitation was set by moving the top mirror using the top z-nanopositioner.

In order to form the cavity, the bottom mirror is brought up towards the top mirror. Initially this is done using the continuous movement control of the bottom z-nanopositioner.

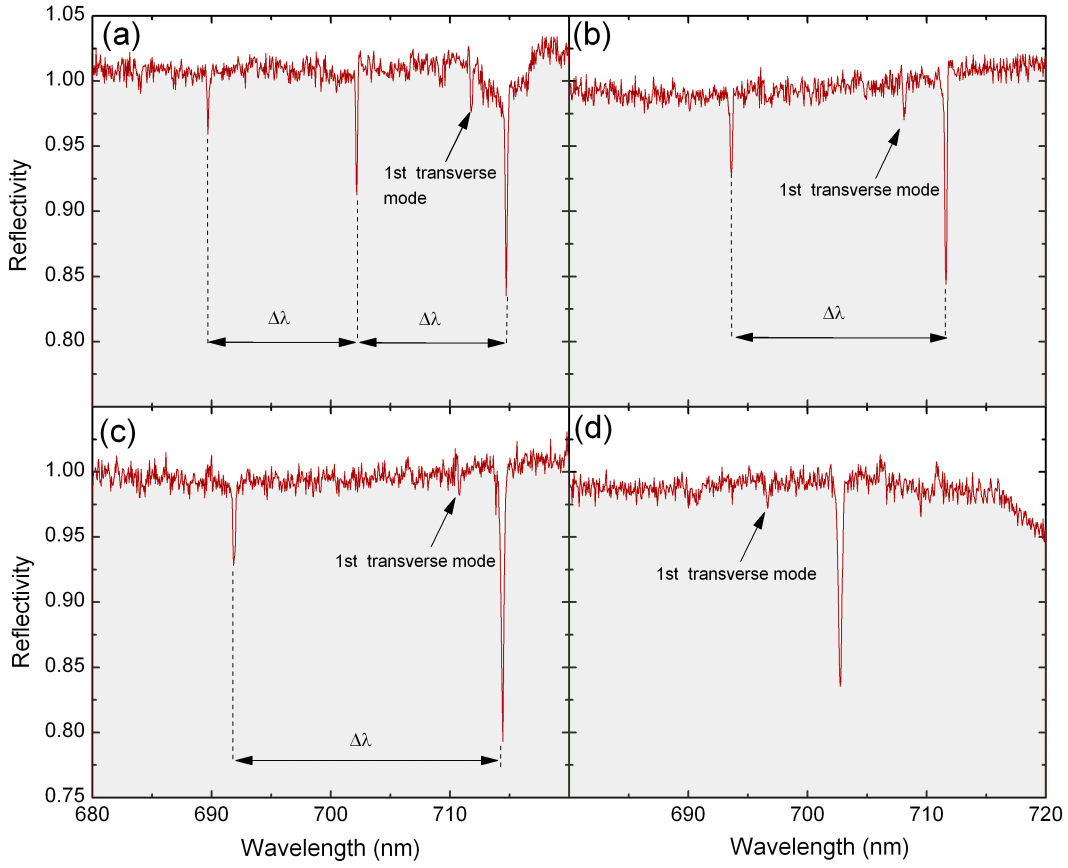

Figure 2.12: Normalised white reflectivity spectra of cavities formed with RoC = 25 µm. (a) L = 20.0 µm (b) L = 13.6 µm(c) L = 12.7 µ(d) L = 2.1 µm. A single longitudinal resonance is present within the spectral window.

When the mirror separation becomes small (L ≈ 30 µm) a number of fringes become visible across the planar region of the top mirror. These correspond to the Fabry-Perot resonances of the planar cavity where the fringes appear due to the relative angle between top and bottom mirrors. In order to reach small mirror separations, the two mirrors must have a high degree of parallelism between them. These fringes provide an indication of this relative angle and can be corrected for by using the two goniometer stages, which allow the bottom sample to be tilted in ϕ and θ. When the relative angle between the two mirrors is removed, the fringes are no longer present and instead the entire planar area local to the pump spot lights up with a symmetrical spatial distribution. Once a high de-

gree of parallelism is achieved, the mirror separation is reduced until the stability criteria $L < RoC$ is reached. At this point stable resonator modes exist within the concave-planar cavities. The cavity lengths in this case are estimated using Eq 2.11 from the longitudinal mode spacing. Further fine tuning of the angle can then be performed to minimise the cavity length through incrementally changing both θ and ϕ and measuring the mode spacing when the mirrors are touching. The cavity length is then reduced by $\approx \lambda/2$ so that the mirrors are no longer touching and the full tunability of the longitudinal mode is possible. Fig. 2.12 shows the reflectivity spectra of the hemispherical cavity formed with a RoC = 25 μm concave DBR for various cavity lengths. The white light spectra is significantly distorted from the use of aspheric lenses as an objective along with fiber collimation and collection lenses. This introduces three sources of chromatic aberration. At a cavity length of L = 20.0 μm a number of longitudinal resonances are present within the spectra (Fig. 2.12 (a)) where the cavity length has been estimated using the mode spacing and Eq 2.11. As the mirrors are brought closer the mode spacing decreases until a single longitudinal mode is present within the spectral window (Fig. 2.12 (d)) at a cavity length of 2.1 μm. The Q-factor is around 3,000 at L = 2.1 μm and around 7,000 at L = 20.0 μm. This is attributed to the increased photonic lifetime due to the much larger cavity length. This is in contrast to the expected value of around 8,000 at L $\sim$ 1 μm from the FDTD simulations in Section 2.4.3. This can be attributed to a combination of being off the centre of the DBR stopbands by 50 nm along with broadening of the cavity resonance due to acoustic vibrations. The cavity length is estimated from a reference reading from the closed loop piezo readout, where the cavity length can be estimated from the longitudinal mode spacing. This mode spacing is shown clearly in Fig. 2.12 (a) and gives a value for the effective cavity length including the penetration into the DBR mirrors L_{DBR}. For the dielectric DBRs used here, this penetration is small due to the large refractive index contrast and can be estimated, using a transfer matrix simulation, to be $\sim$ 1.2 μm for both top and bottom mirrors. The first transverse mode associated with the longitudinal mode is present in the spectra, but the drop in intensity is weak due to the poor mode matching

with the excitation spot. Higher order transverse mode resonances are not revealed due to even poorer mode matching between the resonant white light and the higher order modes. This is because the the pump spot is a TEM_{00} Gaussian beam with a lateral size of around 2 μm, while the higher order modes have transverse Gaussian profiles that do not match this profile leading to poor transmission of the resonant excitation into the cavity.

These experimental results demonstrate that the open cavity system achieves all of the motivating criteria presented in Section 2.2 such as spectral and spatial tunability, free space optical access, and operation at cryogenic temperatures. The relatively low Q-factor measured at L = 2 μm can be attributed to instabilities in the system, most likely introduced by acoustic vibration. In the next chapter on strong coupling in the system a number of dampening mechanisms and isolation systems are introduced in order to significantly increase the photonic Q-factors due to increased stability against acoustic vibrations.

2.7 Summary

The open cavity system was developed from initial design considerations to the experimental demonstration of stable cavity modes at low temperature. This included the construction of a custom housing for the cavity and a homemade bath cryostat system. The Gaussian mode structure of the hemispherical cavity was discussed theoretically and shown to allow for submicron beam waists for radii of curvature below 15 μm. An FDTD study was performed showing the electric-field profile of the confined longitudinal mode and revealed that the interface between planar and concave DBR regions is likely to result in an increase in photonic losses in the system. A low temperature demonstration of the tunable cavity was performed using two dielectric DBR mirrors to form a hemispherical cavity. Q-factors of up to 7,000 and cavity lengths down to 2 μm were achieved. Further work in this thesis builds upon this initial demonstration where the developed tunable cavity system is used to study strongly confined exciton-polaritons.

Chapter 3

Zero Dimensional Exciton-Polaritons

In this chapter strong exciton-photon coupling is demonstrated in the tunable cavity system presented in the previous chapter. The hybrid cavity consists of a bottom semiconductor DBR with a cavity region containing 6 $In_{0.06}GaAs$ QWs and a top dialectric concave DBR. Using the nanopositioners to independently position the two mirrors, the cavity resonances were tuned through the QW exciton energy. When close to resonance a characteristic anticrossing was observed demonstrating strong coupling with a Rabi splitting of up to 5.8 meV. The combination of both longitudinal and lateral confinement creates photonic confinement in 3-dimensions and leads to the formation of 0-dimensional polariton dots. For the smallest radii of curvature concave mirrors of 5.6 μm and 7.5 μm, real-space polariton imaging revealed submicron lateral confinement due to the hemispherical cavity geometry.

3.1 Introduction

As discussed in Section 1.2.2 the strong coupling between a QW and cavity photons in a semiconductor microcavity lead to the formation of quasiparticles known as exciton-polaritons. Such systems are of significant interest due to their part-matter part-photon nature - leading to both a large nonlinearity arising from exciton-exciton interactions and the ability to out-couple to the photon field.

In recent years polaritonic systems have attracted significant attention as they exhibit topical phenomena such as non-equilibrium BEC [7], superfluid-like behaviour [8] and bright soliton [16] and dark soliton [69] formation. Conventional microcavity systems are monolithic systems consisting of two semiconductor DBRs separated by an $m\lambda/2$ cavity region containing one or more QWs located at electric-field antinodes. The cavity resonance in these systems is fixed during fabrication and in-situ tuning of the cavity energy is limited to the incorporation of a tapered cavity region across the MBE grown microcavity. As discussed in the previous chapter, by using an open cavity system full tunability of the cavity resonance can be performed.

3.1.1 Lateral Confinement

The photonic component of polaritons leads to a low in-plane effective mass of around 10^{-4} m_e. Due to this, micrometer sized lateral confinement causes discretisation of the polariton energies. This lateral confinement also increases the polariton-polariton interaction strength for the equivalent excitation power due to the increased overlap of the excitonic component of their wavefunction. As discussed in Section 1.6, combining very narrow polariton linewidths with strong submicron lateral confinement has the potential to lead to the observation of polariton blockade. A number of systems have been developed to laterally confine polaritons based upon confinement of either their excitonic or photonic component. Spatial modulation of both excitonic and photonic components

can be introduced using cross propagating surface acoustic waves (SAWs) but the confinement size is currently limited to around 8 μm due the small penetration of the SAWs at high frequency [88]. Controlled stress has been applied to a monolithic microcavity in order to introduce a stress potential which spatially localises the exciton wavefunction. In this case the confinement is relatively weak and the polariton energy spectrum remains a quasi-continuum and not strong discretisation [27, 28]. Mesa structures have been fabricated within monolithic microcavities through patterned regrowth which confines the photonic component in 3-dimensions [31]. These mesa structures act as polariton traps forming areas of 0-dimensional confinement within a 2-dimensional microcavity due to a slight variation in cavity length. Micropillars, fabricated through post growth etching, introduce lateral confinement through total internal reflection at the sidewalls [32]. Typically, reduced lateral dimensions lead to significantly larger losses and degradation of the polariton linewidth due to surface scattering and recombination. Linewidths are around 4 meV for micron sized etched micropillars, which for one QW is comparable to the Rabi splitting. As such, the strong coupling cannot be fully resolved and a Kerr nonlinearity cannot be achieved. Finally, post growth etching can be used to fabricate photonic crystal cavities with small lateral dimensions [33]. Significantly, in all the above cases, the ability to perform in-situ tuning of the cavity mode energy is extremely limited.

3.2 Cavity Mirrors

The formed cavity consists of two mirrors mounted on two independent nanopositioner stacks which allows full spatial and spectral tuning of the cavity, as discussed in the previous Chapter. Fig. 3.3(a) shows the set-up of the open cavity system. This consists of a top dielectric concave DBR array and a bottom semiconductor DBR with a cavity region containing QWs that are separated by a micron sized gap. The top mirror is an array of dielectric concave DBRs with various radii of curvature which are fabricated using FIB milling, before coating with dielectric layers as discussed in Section 2.5.1. In contrast to

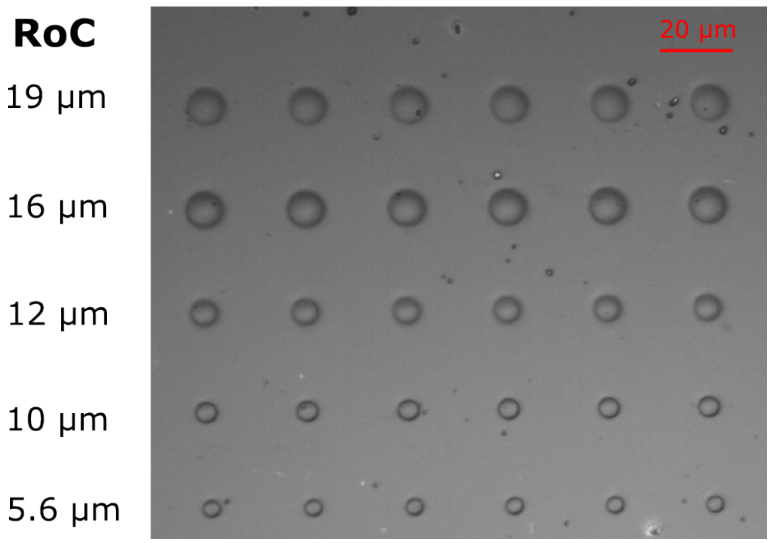

Figure 3.1: Concave mirror array consisting of various radii of curvature.

fiber based open microcavities, where the concave feature is fabricated using laser ablation into the end of an optical fibre [36, 89, 90, 39] FIB milling on a planar substrate allows both the fabrication of smaller RoCs and allows multiple concave mirrors with different RoCs to be fabricated in an array on the same sample. A microscope image of the concave mirror array is shown in Fig. 3.1. The radii of curvature of the different concave mirrors is 19 µm, 16 µm, 12 µm, 10 µm, 7.5 µm and 5.6 µm with a corresponding decrease in the feature diameter. The lateral confinement of the Gaussian beam waist is smaller for decreasing radius of curvature. The required concave mirror is then selected by placement in the optical path using the xy-nanopositioners. The dielectric DBR is formed with 9 pairs of SiO_2/TiO_2 quarter wavestacks, terminating with a high index TiO_2 layer. The substrate is a double sided polished silica substrate. The bottom sample is a semiconductor half-cavity consisting of a 27 paired GaAs / $Al_{0.85}Ga_{0.15}As$ DBR grown via MBE on a GaAs substrate. On top of the planar DBR a $3\lambda/2$ GaAs active cavity region was grown. This contains two sets of 3 10nm $In_{0.05}GaAs$ QWs placed at adjacent electric-field antinodes as shown in Fig. 3.2. For the semiconductor mirror the piezo stack also consists of two tilt goniometer stages allowing full control of the parallelism between the mirrors.

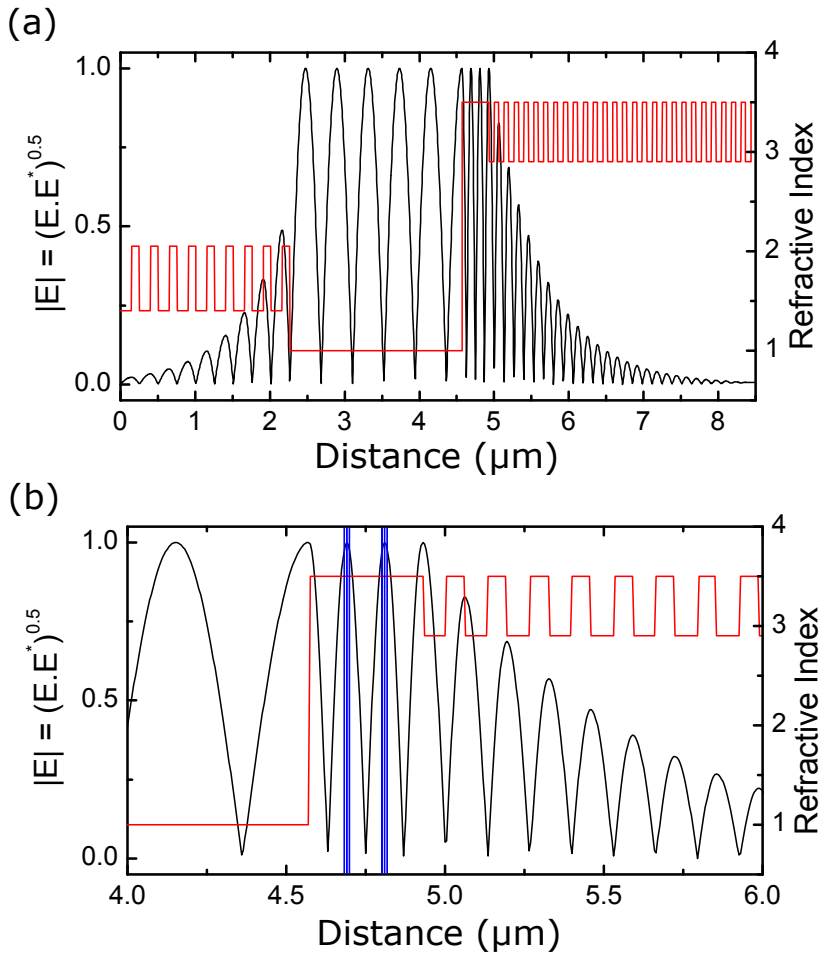

Figure 3.2: Theoretical E-field profile in formed cavity. The concave top mirror has been modelled as a planar mirror in order to use a transfer matrix approach. (a) Full cavity with a 9 paired SiO_2/TiO_2 top mirror, a $11\lambda/4n$ air gap and a bottom 27 paired GaAs / $Al_{0.85}Ga_{0.15}As$ DBR with a $3\lambda/2$ GaAs cavity region at the surface containing $In_{0.05}GaAs$ QWs. (b) Close up of the QW containing region. Two sets of three 10 nm $In_{0.05}GaAs$ QWs are placed at E-field antinodes in a cavity region at the surface of the semiconductor DBR.

3.3 Cavity Characterisation

The cavity characterisation was performed at low temperature by placing the open cavity insert inside a vacuum bath cryostat which is securely fastened inside a liquid He Dewar. A small amount of He exchange gas is used to assist in thermalisation before the cryostat is cooled. Optical access to the cavity is provided by the attachment of a small Thorlabs optical table on the top of the cryostat with free space optical access down to the cavity though an optical window.

Stable modes are formed within a hemispherical cavity when the stability condition $L_{phys} \leq$ RoC is satisfied, where RoC is the radius of curvature of the concave mirror and L_{phys} is the physical cavity length and must take into account the field penetration into the DBRs. [84] For the hybrid cavity here the physical length is defied by

$$L_{phys} = L + L_{DBR1} + L_{DBR2} + L_{QW} \tag{3.1}$$

where L is the tunable mirror separation distance as indicated in Fig. 3.3(a), L_{DBR1} and L_{DBR2} are the physical field penetration depths into the dielectric and semiconductor DBRs and L_{QW} is the physical length of the cavity-QW containing region. The longitudinal spectral resonances of the cavity are determined by the condition that the round trip phase in the cavity $\phi(k, L)$ is an integer multiple of 2π.

$$\phi(k, L) = 2kL + \phi_{DBR}(k) = 2m\pi \tag{3.2}$$

where m is an integer, k is the vacuum wavenumber and L is the mirror separation distance. The structural constant $\phi_{DBR}(k)$ is the sum of the reflection phases of the top DBR and combined bottom DBR and cavity region and may be calculated using a transfer matrix technique. This formula may be rearranged to allow extraction of the mirror separation L from the free spectral range $\Delta\lambda = \lambda_{(m-1)} - \lambda_{(m)}$ between adjacent longitudinal modes. The usual expression becomes modified to account for the difference in DBR reflection phase

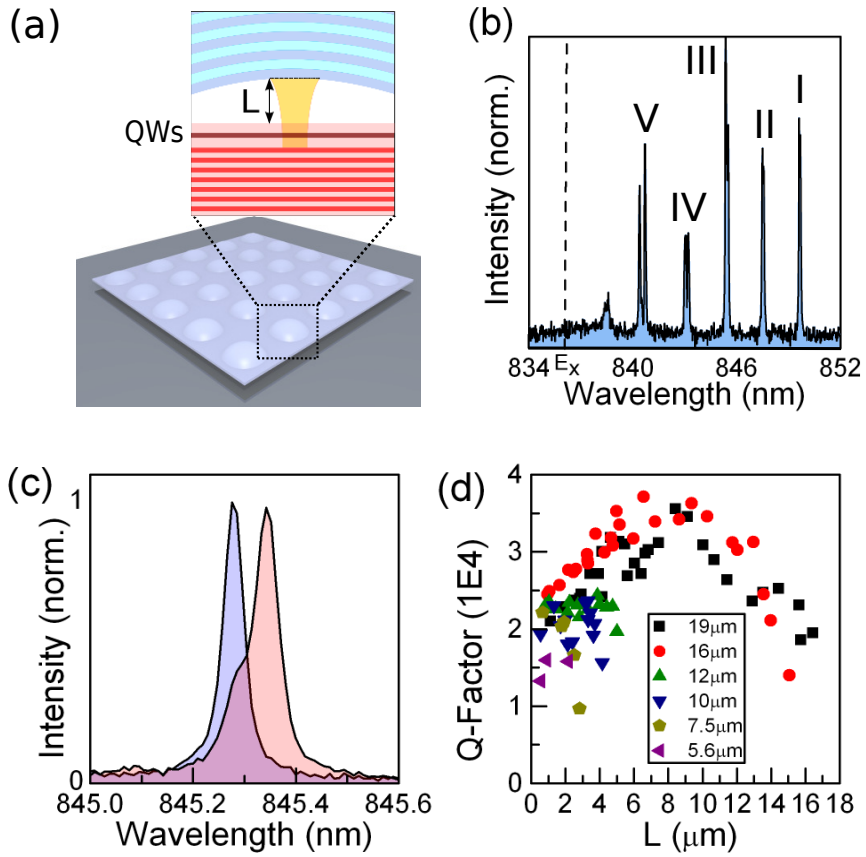

Figure 3.3: (a) The open cavity system formed by an array of dielectric concave DBRs and a semiconductor DBR containing QWs. The inset shows the formed hemispherical cavity with the mirrors separated by a small gap. (b) Typical photoluminescence (PL) spectrum at large negative exciton-photon detuning showing the formation of a longitudinal mode and higher order transverse modes due to lateral confinement (c) The longitudinal mode at large negative detuning shows an orthogonal polarisation splitting of 110 μeV due to birefringence. (d) Photonic Q-factor as a function of mirror separation for concave mirror RoCs of 19 μm, 16 μm, 12 μm, 10 μm, 7.5 μm and 5.6 μm.

$\Delta\phi_{DBR} = \phi_{DBR,(m-1)} - \phi_{DBR,(m)}$ at the two wavelengths of the adjacent longitudinal modes.

$$L = \frac{\lambda_m^2}{2\Delta\lambda}\left(1 + \Delta\phi_{DBR}/2\pi\right) \tag{3.3}$$

3.3.1 Photoluminescence

Fig. 3.3(b) shows a typical photoluminescence (PL) spectrum with the longitudinal cavity mode at a large negative exciton-photon detuning of around -22.7 meV. In this regime the lower polariton is largely photonic and the optical characteristics of the cavity can be probed. Non-resonant excitation is performed close to a cavity reflectivity minimum using a 685 nm laser diode. Spectroscopy is performed using a 0.75m monochromator with a cooled CCD at $-70°C$. In addition to the ground longitudinal cavity mode a number of higher order transverse modes (labelled II, III, IV, V) with equal energy spacing due to lateral confinement are observed. This suggests that the transverse photonic potential created by the curved top mirror is nearly parabolic. Fig. 3.3(c) shows that for a concave mirror of 19 μm the longitudinal mode exhibits a splitting between orthogonally polarised modes of ∼110 μeV, which is likely to arise from birefringence in the bottom and/or in the top mirror due to stress. Higher order transverse modes also split into doublets with an energy splitting of the order of ∼100-200 μeV as seen in Fig. 3.3(b) due to a combination of birefringence and breaking of the cylindrical symmetry in the shape of the top mirror.

Fig. 3.3(d) shows the photonic Q-factor as a function of L measured for mirrors with different RoC, where L was deduced from white light reflectivity spectra using Eqn. 3.3. The photonic Q-factor of the microcavity increases with cavity length due to the increased photonic lifetime from around 25,000 at $L = 1$ μm up to a maximum value of $\approx 35,000$ at $L = 9$ μm for the mirror with RoC = 19 μm and 16 μm. The Q-factor then decreases as L and hence L_{phys} increase further. This can be attributed to the diverging beam waist on the concave mirror leading to larger losses as we approach the limits of the stability condition

[41]. Furthermore, the increase in beam waist size on the concave mirror also leads to increased out-coupling of the polaritons through the concave-planar mirror interface as shown in Fig. 2.8. The minimum mirror separation before touching that can be reached is $L \approx 1$ μm. This is only achievable as in-situ control of the mirror parallelism using the goniometer stages to tilt the bottom mirror in ϕ and θ is possible.

3.4 Strong Coupling

In order to spectrally tune the cavity resonance, a DC voltage was applied to the bottom z-piezo nanopositioner which decreases the mirror separation L. By scanning the cavity length in this manner, the cavity modes are tuned through resonance with the QW exciton energy. Fig. 3.4(a) shows the characteristic avoided crossing in PL between the cavity modes and QW exciton. It is clear that both the longitudinal mode and higher order transverse modes all display an avoided crossing with the exciton resonance. Each photonic mode is characterized by a specific field distribution in the plane of the QWs and couples to an excitonic mode with the same in-plane distribution. As a result, different photonic modes couple to spatially orthogonal exciton states. Polariton states from different photon modes are therefore orthogonal and are well described by the coupling between a single photon mode and a single excitonic mode for each of them. The Rabi splitting Ω_{Rabi}, when mode-I is at resonance with the QW exciton at a mirror separation $L \sim 5$ μm, is 4.4 meV and is comparable across all modes due to the negligible dependence of the coupling strength with exciton wavevector. Fig. 3.4(b) shows a spectral slice at zero detuning between the longitudinal mode and the QW exciton. The confined upper polariton has a weaker PL signal as polaritons tend to relax towards the lowest energy states of the trap. The upper polariton is significantly broader than the lower polariton branch due to scattering with phonons and QW disorder potential to the lower polariton and the exciton reservoir [91]. At zero exciton-photon detuning at the minimum effective cavity length we measure a lower polariton linewidth of 260 μeV. The bare QW exciton linewidth is 1.2

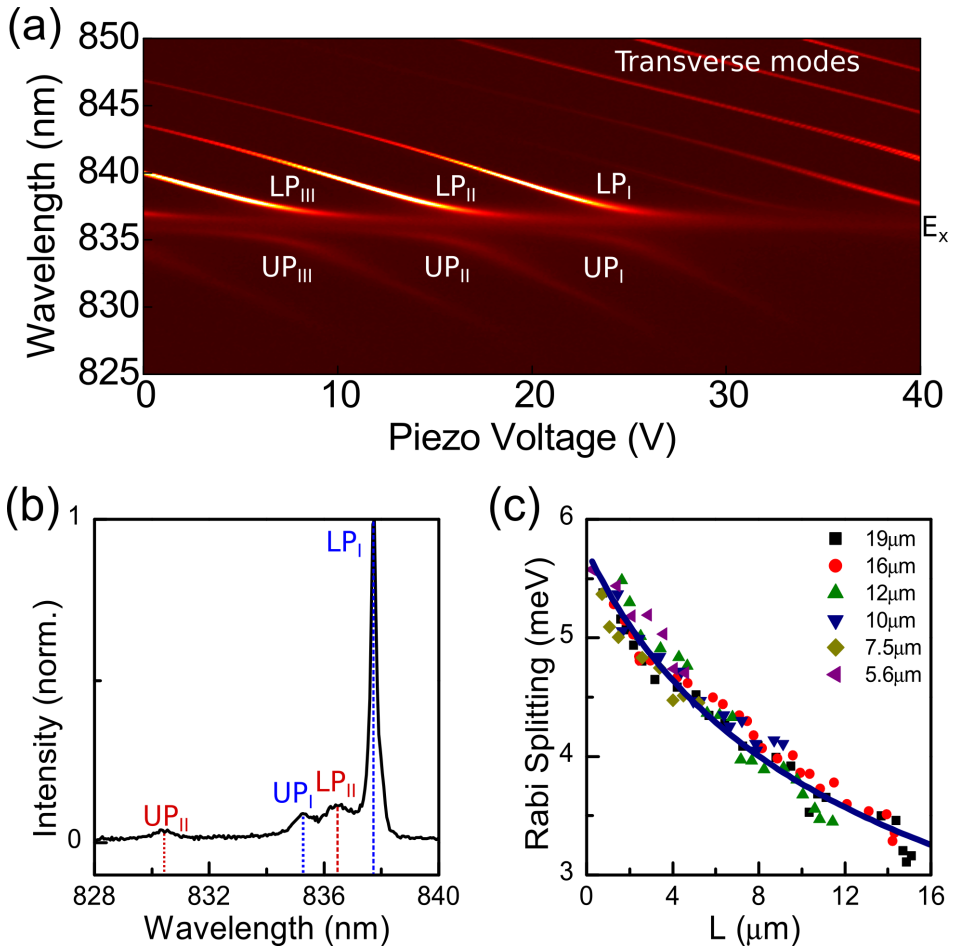

Figure 3.4: (a) Typical avoided crossings as the cavity modes are tuned through resonance with the QW exciton. The RoC of the concave mirror was 19 μm and the mirror separation decreases with increasing piezo voltage. As well as the longitudinal mode we observe strong coupling between the exciton and all observed higher order transverse modes. (b) Spectral slice close to resonance between the ground Mode I and QW exciton. The blue dashed and dotted lines indicates the lower (LP_I) and upper (UP_I) polariton arising from exciton coupling with mode I with a splitting of 4.4 meV at zero detuning. The red indicates the lower (LP_{II}) and upper (UP_{II}) polariton branches arising from transverse mode II. The mirror separation L = 5 μm. (c) Rabi splitting at zero exciton-photon detuning as a function of mirror separation for concave mirror RoCs of 19 μm, 16 μm, 12 μm, 10 μm, 7.5 μm and 5.6 μm.

meV and the photonic linewidth is around 78 μeV. At the minimum cavity length, the maximum observed vacuum Rabi splitting at resonance is 5.8 meV which is comparable to the values obtained in monolithic 6 QW $3\lambda/2$ microcavities. In Fig. 3.4(c) we plot the Rabi splitting at zero exciton-photon detuning as a function of L for cavities formed with each of the concave RoCs. The splitting is expected to be inversely proportional to the square root of the cavity effective length L_{eff}, which is given by the ratio of the integrated electric energy density in the cavity divided by the density at the QWs [92]. At fixed energy L_{eff} is proportional to $L + C$ where L is the mirror separation and the constant C accounts for the fraction of the mode energy located in the DBRs and QW region. The fit in Fig. 3.4(c) corresponds to $\Omega_{Rabi} \propto 1/\sqrt{L + L_{DBRs}}$ with $L_{DBRs} \approx 7.6$ μm.

3.5 Polariton Wavefunction

Since polaritons couple out of the cavity through the emission of a photon, the emission intensity profiles directly correspond to that of the polariton wavefunction. By imaging the emitted light from the hemispherical cavity the nature of the photonic confinement on the beam profile can be assessed.

3.5.1 Imaging System

The open nature of the tunable cavity gives direct optical access to the intensity profile of the emitted light. Since the system is based upon a bath cryostat system, a mechanism is required to project the image from the optical table on top onto the slits of the spectrometer. Furthermore, added complexity is introduced since the system lies at the end of a 1.2 m tube - hence requiring any fourier plane imaging to form a fourier image >1.2 m above the primary plane. To enable imaging of the polariton modes, a wound fiber bundle consisting of a 4×4 mm array of single mode fibers was employed. Each single mode fiber

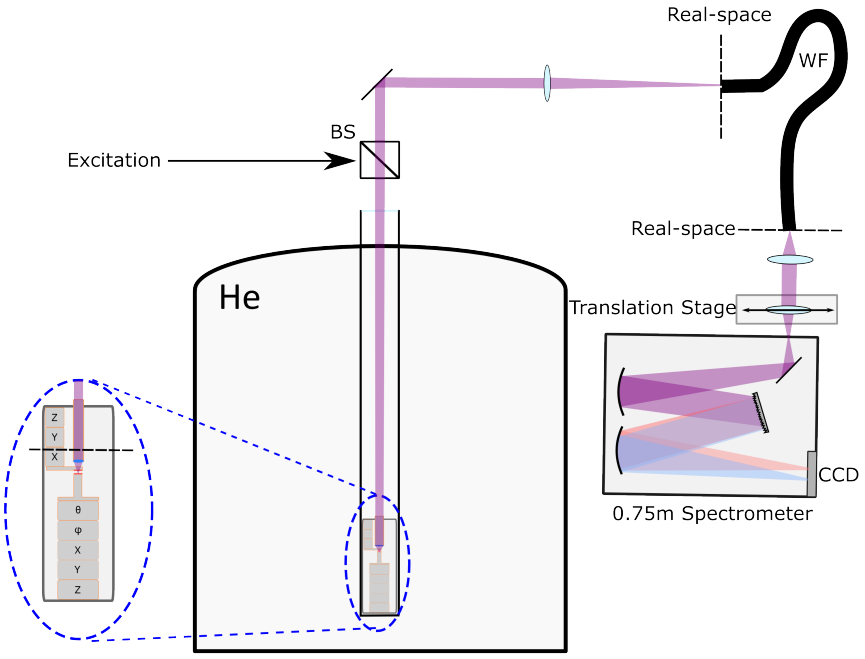

Figure 3.5: Real space imaging system. A wound fiber bundle (WF) is used to project the real space image from the optical table placed on the open cavity insert onto an optical bench where the image is scanned across the spectrometer slits to produce a tomographic image.

in the array acts like a single pixel, allowing the image focused on one end of the fiber to be emitted from the other end.

Fig 3.5 shows the real space imaging system used in the open cavity. A 0.55NA aspheric objective collimates the emitted light before being focused onto the end facet of a wound fibre bundle using a 50 cm lens. The total magnification in this set-up is 110X giving an image size of the 1.1 mm for a concave mirror with 10 μm diameter and RoC = 19 μm. If Fourier imaging is used a set of confocal lenses are placed within the cryostat tube to project the Fourier plane onto the optical table above. This is discussed in depth in Section 4.5.1 when Fourier imaging is employed. The image incident on the wounded fibre bundle is then imaged onto the spectrometer slits using a pair of confocal lenses. A translational stage on the final lens is used to scan the image across the slits to produce tomographic real space images. Reflected laser light is removed using a 700 nm long-pass filter placed before the fibre bundle.

3.5.2 Gaussian Mode Profiles

Fig. 3.6 (a) shows position-wavelength images of cavity modes when longitudinal mode I is negatively detuned with respect to the exciton. Here the emission intensities are plotted for different wavelengths versus position across the line going through the middle of the cavity. These spatial mode profiles correspond to the modes that we display spectrally in Fig. 3.3(b) at slightly larger negative detuning of -4.7Ω_{Rabi} = -24.4 meV and provide direct evidence of the micrometric sized confinement and spatial discretisation of modes. Fig. 3.6(b) shows the position-wavelength images of polariton modes when the longitudinal mode is close to resonance with the QW exciton. Here we can clearly see the imprinting of the photonic spatial distribution into the polariton modes UP_I and LP_I and UP_{II} and LP_{II}. Modes UP_I and LP_I are characterised by Gaussian spatial distribution, whereas modes UP_{II} and LP_{II} have two distinct maxima at ± 1 μm. For the longitudinal mode we measure a Gaussian beam waist size of 1.16 μm (FWHM = 1.36 μm) on the concave

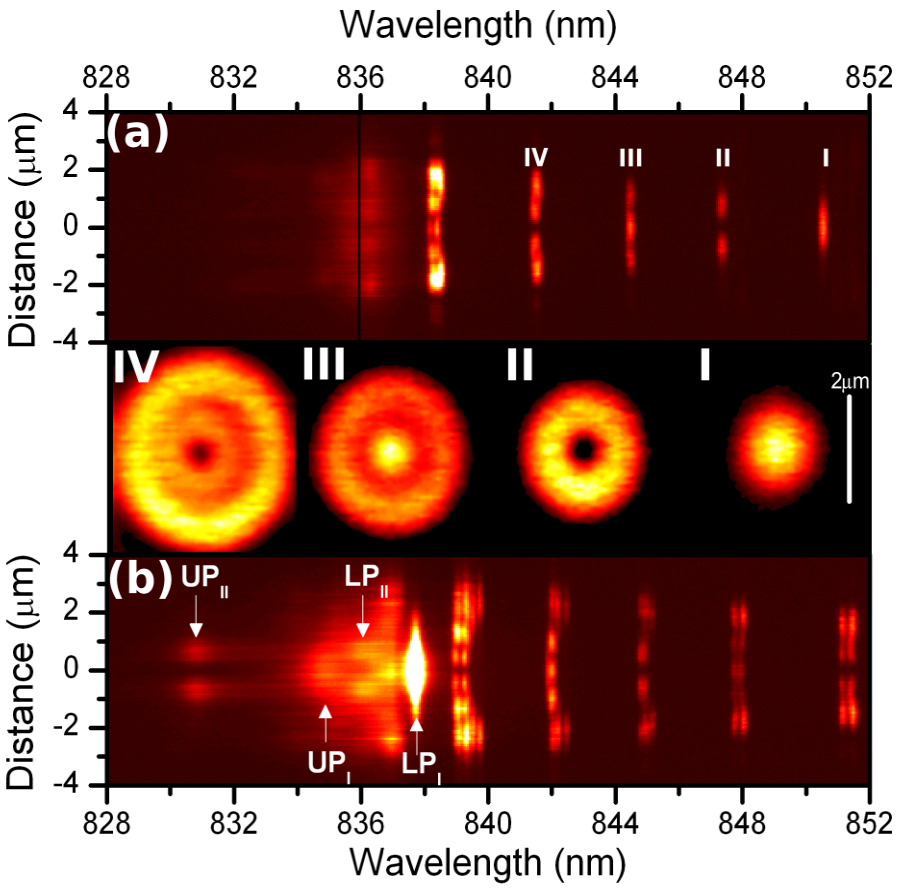

Figure 3.6: (a) Position-wavelength images of cavity modes when longitudinal mode I is at a very large negative exciton-photon detuning of around -5Ω_{Rabi} = -26 meV. The black vertical line indicates the QW exciton energy. The concave mirror RoC was 19 μm. Insets I-IV: Real space PL images of photonic modes revealing profiles for modes I, II, III and IV. (b) Position-wavelength images of cavity modes when ground mode I is close to resonance with the QW exciton. The formation of both UP_I /LP_I at resonance and UP_{II}/LP_{II} at a positive exciton-photon detuning of approximately 1.5Ω_{Rabi} = 7.8 meV are labelled. At longer wavelengths we see a number of high order transverse modes associated with another longitudinal mode at lower energy.

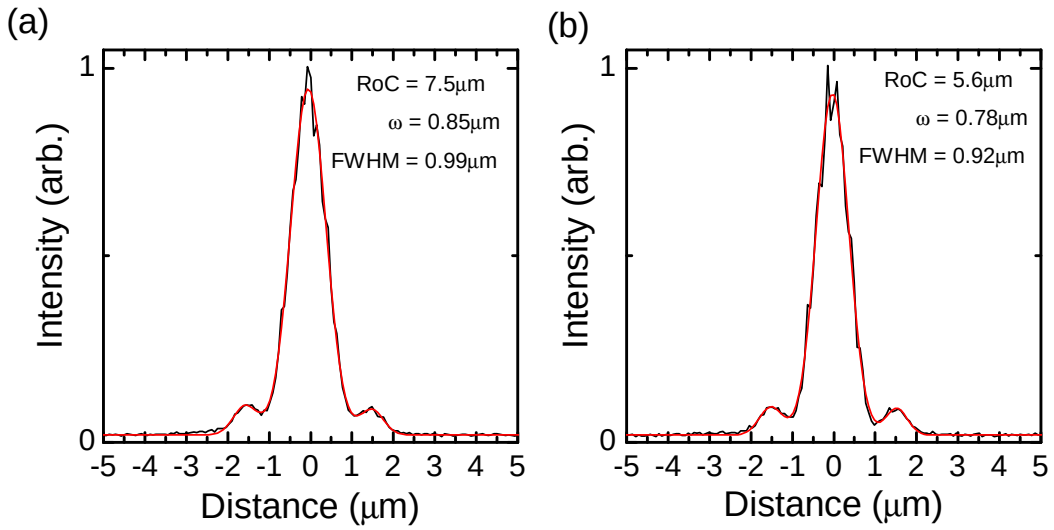

Figure 3.7: (a) Real space image slice of longitudinal modes for RoC = 7.5μm concave mirror. The Gaussian beam waist is 0.85 μm. The peaks either side of the main peak are due to diffraction. (b) Real space image slice of longintudinal mode for RoC = 5.6 μm concave mirror. The Gaussian beam waist is 0.78 μm.

mirror with RoC = 19 μm at $L \approx 1.7$ μm. For the RoCs of 7.5 μm and 5.6 μm the Gaussian beam waist sizes are 0.85 μm (FWHM = 0.99 μm) and 0.78 μm (FWHM = 0.92 μm) as shown in Fig 3.7. This is comparable to, or better than the confinement achieved in mesa [31, 93] or micropillar [32] structures. We note that the beam waist size on the planar semiconductor mirror is slightly smaller than the beam waist on the concave mirror when $L_{phys} \ll$ RoC [84].

The inset in Fig. 3.6 shows the real space PL images of photonic modes revealing profiles for modes-I, II, III and IV, which resemble helical Laguerre-Gaussian (LG) transverse modes. Formation of such modes is expected in a system with perfect cylindrical symmetry [94]. Nevertheless, spectrally resolved images reveal that the LG modes in our system actually are not the eigenstates and are split into a family of Mathieu and Ince-Gaussian modes most likely due to breaking of the cylindrical symmetry of the top mirror [85].

In order to resolve the splitting of the circularly symmetric Laguerre-Gaussian mode profiles that we see in Fig. 3.6 a higher order grating spectrometer of 1800 lines/mm was

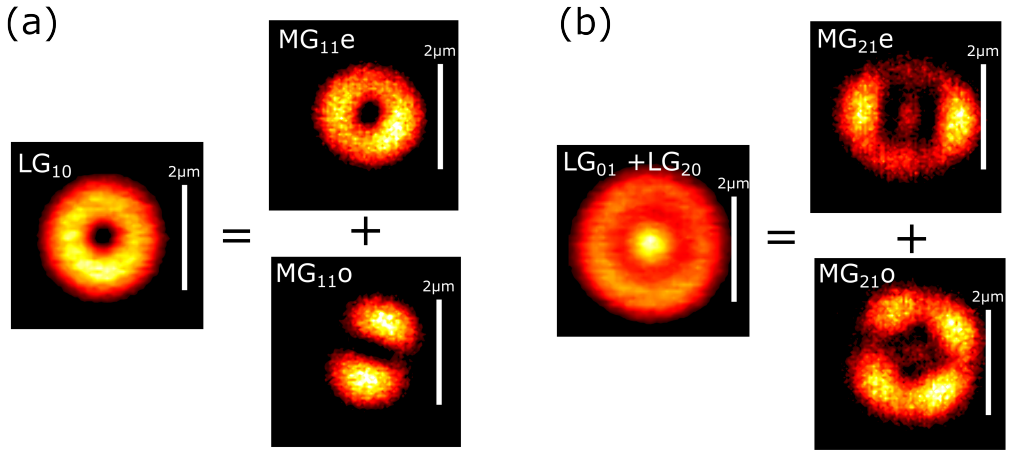

Figure 3.8: (a) The left hand side shows the real space image of the first transverse mode when close to resonance with the QW exciton. The right hand side shows tomographic images of the two peaks corresponding to this mode when resolved at large negative detuning. The mode profile shows an orthogonal lobe structure identified with Mathieu-Gaussian or Ince-Gaussian elliptical modes. (b) Second transverse mode corresponding to the LG_{10} and LG_{02} which are degenerate in energy.

used in conjunction with tomographic imaging. Here the spectral splitting of the modes can be resolved and the mode profile is constructed by scanning the real space image across the spectrometer slits. The spectrometer slit selects a y-slice through the image. Post-processing of a particular CCD pixel then allows the construction of the real space image from a series of y image slices. By selecting the CCD pixel which corresponds to a particular mode energy, the mode profile may be constructed.

Fig 3.8 (a) shows the splitting of mode-II observed at large negative detuning. Here, the largely photonic polariton inherits the coherence from the cavity photon leading to narrow linewidths of the modes. A splitting of the mode of around 1.3 meV is resolved and the tomographic images of the two modes is plotted in the right hand side of Fig 3.8 (a). These modes show clear lobes along orthogonal axes indicating a breaking of the cylindrical symmetry. This most likely arises due to a slight asymmetry in the concave mirror shape and are described by Mathieu-Gaussian (MG) mode profiles. The $MG_{11}e$ modes lobe structure is not as pronounced as the $MG_{11}o$ modes. Fig 3.8 (b) shows the splitting of

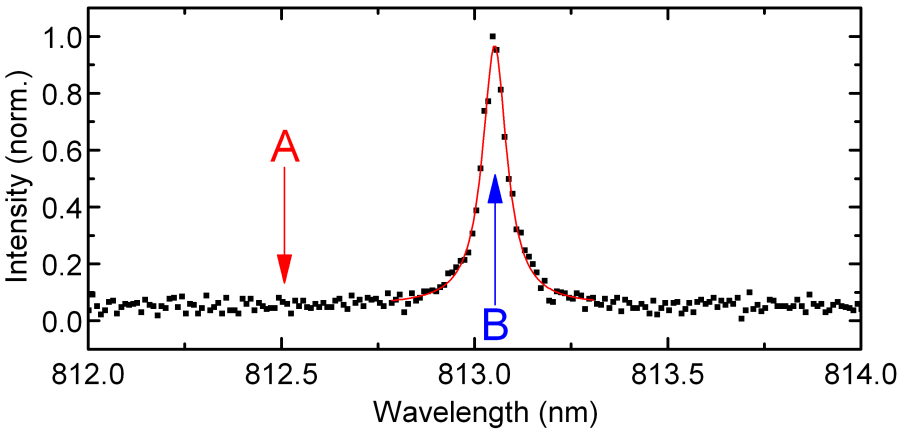

Figure 3.9: PL emission from cavity with a negative exciton-photon detuning. Point A corresponds to the tunable laser wavelength when pumping off resonance to extract the laser and electric noise. Point B corresponds to the resonant pumping configuration for extracting the electrical, laser and acoustic noise.

the 3rd transverse mode that consists of the superposition of the LG_{01} and LG_{20} modes which are degenerate in energy. The two resolved peaks on the right hand side correspond to the two Mathieu-Gaussian modes MG_{21}e and MG_{21}o. This mode splitting is discussed in detail in Chapter 4, where the large decrease in polariton linewidth above the polariton lasing threshold allows the underlying cavity structure to be fully revealed.

3.6 Open Cavity Stability

The open cavity is extremely sensitive to acoustic vibration. Vibrational amplitudes of only a few 10s of picometres are sufficient to cause broadening of the cavity linewidth. As such, this is most likely the limiting factor in the experimentally achieved Q-factors of 25,000 when L = 1 µm. The main sources of vibration can be categorised into internal and external sources. The external sources include environmental factors such as the acoustic vibrations that are coupled through the floor from the building and local conditions in the laboratory such as acoustic noise arising from laboratory equipment and fluctuations in temperature. In order to isolate the system from these external sources the entire Dewar is

housed in a thermal-acoustic chamber consisting of thermally insulating foam, lined with acoustic dampening tiles with a noise reduction coefficient rating of 0.85. Furthermore, the system sits on an small optical table with heavy duty passive isolation feet (Thorlabs PWA075) to isolate it from vibrations through the laboratory floor. The second sources of acoustic vibration which are internal, arise from bubbling due to helium boil off and pressure and vibration fluctuations travelling back along the helium recovery line. The system was isolated from pressure fluctuations using a custom valve to keep the open cavity Dewar pressure fixed at 1.5 psi - a pressure larger than that of the recovery line, ensuring that pressure fluctuations from the line do not travel back into the Dewar. In order to measure the frequencies of the acoustic vibrations, resonant excitation of the cavity mode was performed. This experiment was carried out with a single GaAs QW in a cavity region on the bottom semiconductor DBR. The resonant laser is first slightly detuned from the cavity resonance and the reflected laser signal collected using a fast photodiode corresponding to point A in Fig. 3.9. This signal was then processed using an oscilloscope to extract the time trace of the laser and electric noise of the reflected signal. A fast fourier transform (FFT) was then performed on the time trace in order to extract the frequencies of the electric and laser noise. The FFT amplitude is plotted in Fig. 3.10 (a) showing resonances corresponding to the electric noise at 50 Hz and higher order harmonics at multiples of 50 Hz. Next the laser is tuned into exact resonance with the longitudinal mode at point B in Fig 3.9. Here the noise in the reflected laser corresponds to the electric and laser noise as before but now includes the acoustic noise arising from the shift in the cavity mode due to acoustic vibrations. Fig. 3.10 (b) shows the traces with on resonance excitation at point B with the longitudinal mode when the mirrors are not touching. The cavity Q-factor was around 10,000. A number of broad features are present at frequencies around 170 Hz and 220 Hz which correspond to the main acoustic noise in the system. Fig. 3.10 (c) shows the FFT of the noise when the two mirrors are in contact with each other, and the excitation is in resonance with the longitudinal mode at point B. Previous experiments have shown that touching the mirrors slightly causes an increase in

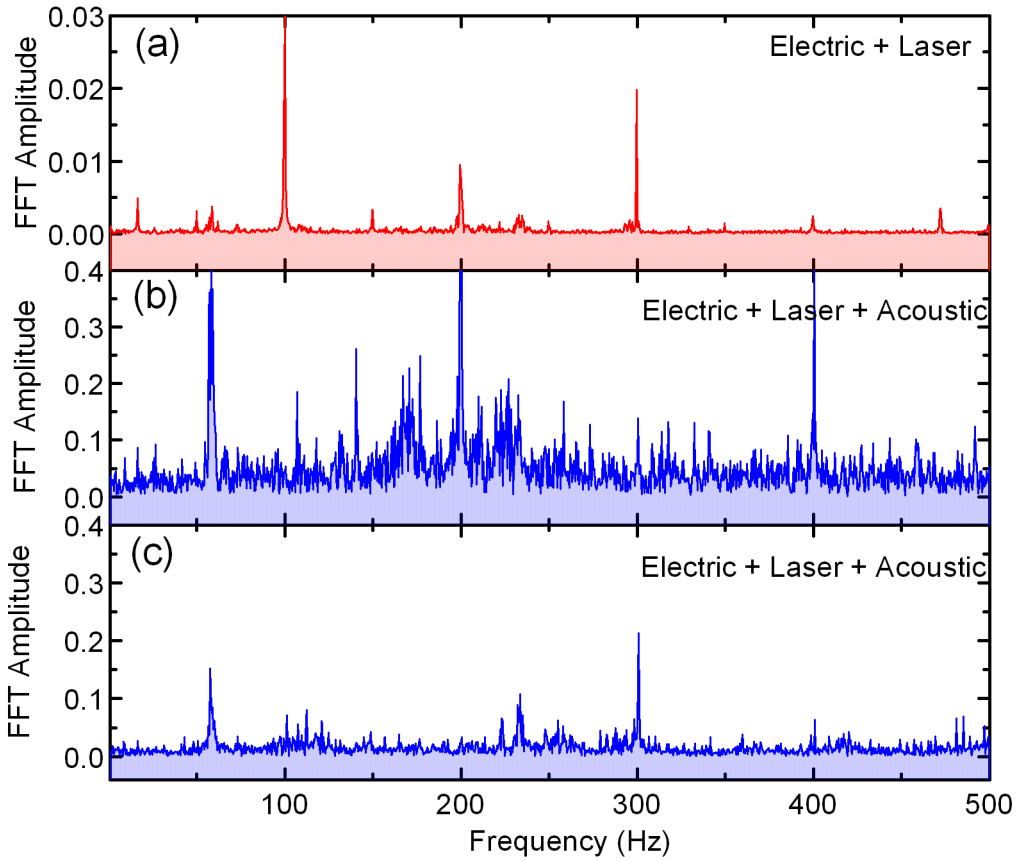

Figure 3.10: FFT amplitudes of reflected laser signal. (a) Non-resonant reflection showing the electrical and laser noise. (b) Resonant reflection with the mirrors out of contact. The trace reveals broad acoustic vibration resonances at 170 Hz and 220 Hz. (c) Resonant reflection with the mirrors in contact. A huge reduction in the vibrational amplitudes is observed with a broad feature at 260 Hz.

the Q-factor which we attribute to synchronisation of the acoustic vibration of the mirrors, dampening the independent vibrations. From this trace it is clear that the amplitude of the oscillations moves to slightly higher frequencies of 260 Hz along with a huge reduction in the FFT amplitude. This amplitude is directly proportional to the magnitude of the mirror movements. Although difficult to quantify the origin of these vibrations, the most likely source is the helium bubbling within the system, causing vibration of the bath cryostat insert which is transmitted to the nanopositioner stacks. This causes the two stacks to move out of phase with different frequencies and amplitudes. Putting the mirrors into contact synchronises these oscillations, leadings to higher Q-factors and stability of the system. It should be noted that when the two mirrors are in contact the system is still fully tunable and the contact is produced through introduction of a slight angle between the two mirrors.

3.7 Summary

In summary a system to achieve 3-dimensional polariton confinement with in-situ tuning of the cavity modes was presented. The mode profiles were shown to be elliptical Gaussian modes where an asymmetry in the concave mirror axes leads to a lifting of the degeneracy. When close to resonance, tomographic imaging shows circularly symmetric Laguerre-Gaussian mode profiles since the linewidth of the underlying mode structures is broader than the splitting. When the cavity was formed with concave DBRs with RoCs of 7.5 μm and 5.6 μm, submicron Gaussian beam waist sizes were measured. Combining the lateral confinement with very narrow lower polariton linewidths has the potential to lead to strong nonlinear interactions between polaritons and the observation of the polariton blockade effect [76] in single or coupled polariton boxes [5]. Finally, resonant excitation was used to extract the frequencies of the low frequency acoustic vibration which is most likely the limiting factor in observing higher Q-factors.

Chapter 4

Spin Vortices in Polariton Condensates

4.1 Introduction

Polariton condensation or lasing is a non-equilbilbrium process which leads to the emission of a coherent light beam. In contrast to conventional lasers, where the gain mechanism is stimulated emission and requires population inversion, polariton lasing is a spontaneous process, arising from the coherent emission of condensed polaritons and does not require population inversion between valance and conduction band electrons. As such, they have significantly lower thresholds than conventional semiconductor lasers [95]. In a polariton laser the coherence is determined by stimulated scattering to the ground state and by interactions within the condensate itself. Potential applications include high-speed optical polarisation switches [96] and novel compact sources of terahertz radiation [97]. The low threshold behaviour has the potential to a create a revolution in low power coherent light sources required for photonic chip integration and in the field of energy efficient optical devices. Besides the practical device applications, polaritons allow the study of the fundamental properties of condensation in the solid state. In particular, polariton

lasing is a phenomenon which lies in-between the extremes of full BEC, which is in thermodynamic equilibrium and the photon laser, which is completely out of thermodynamic equilibrium.

Quantized vortices are topological defects occurring in many physical systems in optics, condensed matter, cosmology and fundamental particles, characterized by a phase winding of an integer multiple of 2π around a vortex core. In semiconductor microcavities, quantized vortices [67, 75, 98] and vortex-antivortex pairs [99, 100, 101, 102] may form spontaneously in exciton-polariton superfluids and non-equilibrium polariton Bose-Einstein condensates (BECs). Much effort has been devoted to the development of methods to create orbital angular momentum (vortices) in polariton condensates, providing ways to study the fundamental physics of metastable currents or for potential use as quantum sensors [103] or information encoding devices [104]. Optical imprinting [105] of vortices as well as robust spontaneous vortices using chiral polaritonic lenses [106] have been demonstrated. Interestingly, the coherent coupling of the photon pseudo-spin (polarization) with vortex orbital angular momentum has been shown to lead to new types of topological entities, named spin vortices, characterised by quantised spin current instead of phase winding. Uncontrolled spontaneous spin vortices were reported in atomic spinor BECs [107] and in polariton condensates subject to structural disorder[108], although the exact origin of the polariton spin currents remains unclear. The degrees of freedom associated with both the orbital angular momentum and the polarization of a photon may find useful applications in quantum information processing [109, 110, 111].

Recently, considerable attention has been focused on the investigation of polariton spin-orbit (SO) coupling, i.e. the interaction between the polariton orbital motion and its spin due to the effective magnetic field induced by the transverse-electric transverse-magnetic (TE-TM) splitting characteristic of semiconductor microcavities [112]. In condensed matter SO coupling has led to significant physical phenomena such as the spin-Hall effect [113] and topologically protected conducting states [114], whereas in optical microcavities,

SO coupling of exciton-polaritons enables observations of interesting optical counterparts, including the optical spin-Hall effect [115], magnetic-monopole-like half-solitons [116] and possibly topological insulators [117, 118].

The experiments carried out in Chapter 3 demonstrated that tunable open cavities are suitable systems in which to study exciton-polaritons in the strong confinement regime. The lateral confinement was shown to support phase vortex transverse modes with energy spacings that are comparable or smaller than in competing confining systems such as mesas or micropillars [31, 32]. In this Chapter, evidence for polariton condensation is presented. Uniquely, in this system, the large mode spacing and tunability allows any arbitrary transverse mode to be placed close to resonance with the exciton. Above threshold, the increase in temporal coherence of the resulting coexisting polariton condensates allows the underlying modal structure to be resolved. This reveals spin vortices and complex spin textures in the coexisting polariton condensates. These spin vortices arise from the coherent coupling of the polaritonic pseudo-spin with vortex-like orbital momenta arising from the strong SO coupling in the open cavity system. These eigenstates are characterised by quantised spin current instead of phase winding, as in the case of phase vortices. The interplay between the the light-matter component of the polariton condensate (which determines the strength of SO interaction) and the anisotropy of the confinement potential is shown to significantly alter the condensate spin texture and leads to a transition from spin vortices to linearly polarised eigenmodes for increasing exciton fraction. Finally, the tunable cavity is shown to support the formation of stable 2-dimensional polaritons using planar-planar DBR regions, which undergo polariton condensation at high power, with full in-situ tunability of the exciton-photon detuning.

4.2 0-Dimensional Polariton Condensation

This section will present the experimental evidence for polariton condensation in the hemispherical cavities and the underlying SO coupling which determines the complex polari-

sation of the eigenmodes.

4.2.1 Strong Coupling

In order to increase the Rabi splitting and reduce the exciton density for a given excitation power, 12 GaAs QWs were used. The sample was grown by molecular beam epitaxy at the EPSRC National Centre for III-V Technologies, Sheffield and consists of a 31 paired $Al_{0.2}Ga_{0.8}As/Al_{0.95}Ga_{0.05}As$ DBR with a stopband centered at 780 nm. Three sets of four 7 nm QWs are embedded at electric field antinodes both in a cavity region and at E-field antinodes in the semiconductor DBR. Full cavities based upon a similar design have previously shown to have a Rabi splitting of 15 meV and have demonstrated polariton condensation under cw excitation [57]. The top sample is a dielectric SiO_2/TiO_2 11 paired DBR with an array of concave features. Fig. 4.1 shows the photoluminescence as a function of z-nanopositioner voltage at a mirror separation of around 1 μm and a concave mirror with a RoC of 20 μm showing a clear anticrossing between the cavity resonances and the exciton energy. Excitation is performed using a 630 nm laser diode coupled to a multimode fibre at a power of 10 μW and a spot size of around 30 μm using the same experimental set-up as in Fig. 3.5. Assuming a linear relationship between piezo voltage and change in cavity length, a fitting of the LPB using Eq. 1.19 cannot fully account for the curvature of the LPB of the ground state longitudinal mode due to the wavelength dependent phase shift and change in E-field overlap with the QWs as a function of air gap. The Rabi splitting also cannot be estimated from the LPB-UPB energy splitting at resonance since the UPB is not visible due to efficient relaxation. Instead the Rabi splitting is estimated from the planar-planar cavity case that is discussed in Section 4.5 where the angular resolved spectra can be fitted with the expected Rabi splitting of 15 meV.

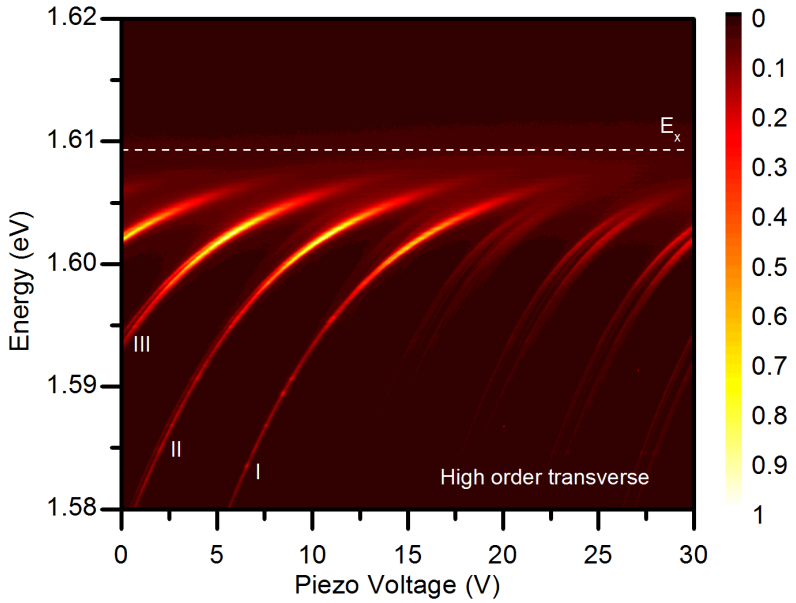

Figure 4.1: Anticrossing between the cavity modes and the QW exciton energy. The bare exciton energy is shown by the dashed horizontal line.

4.2.2 Power Dependence

Fig 4.2 shows the power dependence of the longitudinal mode in a cavity with a concave mirror with a RoC of 7 µm and a detuning of around $\delta = -8.3$ meV. A linear polariser was used in the collection path to select one of the orthogonally linearly polarised modes presented in Fig 3.3 (c). Non-resonant excitation was used at 630 nm close to a stopband minima using a multimode fibre with a spot size on the sample of around 30 µm - larger than the concave mirror diameter. Non-resonant excitation is often seen as a requirement in order to observe polariton condensation as the coherence of the laser is lost during relaxation and the polariton condensate is formed from an incoherent reservoir [7]. Here, the concave mirror had a RoC of 7 µm (smaller radii do not form stable modes due to the large penetration into the semiconductor DBR ($L_{phys} > RoC$)) and a diameter of 4 µm, but similar threshold behaviour of the longitudinal mode is observed for RoCs of 20 µm and 12 µm. A clear non-linear increase in intensity is observed at a threshold power of $P_{th} \approx 40$ mW associated with a buildup of coherence associated with a decrease in the

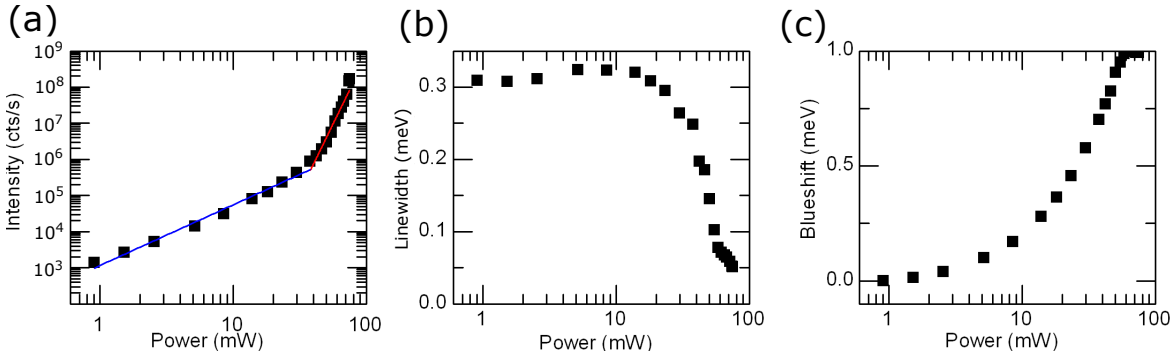

Figure 4.2: Power dependence of the longitudinal mode at resonance for a 7 μm radius of curvature cavity at a detuning of −8.3 meV. (a) Peak intensity showing a nonlinear increase at a threshold power of around 40mW. This is associated with an increase in coherence and drop in the linewidth from 300 μeV to around 50 μeV above threshold. (c) Polariton emission energy as a function of power showing the blueshift as a function of power. The bare cavity mode is 4.5 meV above the LP at low power compared with the 1 meV blueshift.

linewidth from 300 μeV to around 50 μeV - the resolution of the spectrometer. The total blueshift of the polariton energy is around 1 meV in comparison to the lower polariton - cavity mode splitting which is conservatively estimated to be around 4.5 meV. Very similar blueshifts of 1 meV have been reported for polariton condensates in GaAs micropillars [21]. This provides strong evidence that the strong coupling regime is preserved and that the observed nonlinearity is associated with polariton condensation. The laser power limited the range of accessible pump powers so the nonlinear regime is not fully traversed and prevented a second threshold associated with photonic lasing from being seen.

4.3 Spin-Orbit Coupling

The coupling between the spin of an electron and its orbital motion lie at the heart of a number of physical effects such as the spin Hall effect in semiconductors [113] and chiral edge states in topological insulators [119, 120]. Here, SO coupling of the polariton spin and angular motion is studied in transverse Gaussian modes revealing spin vortex and anti-vortex textures. Optically active microcavity polaritons inherit the spin of their

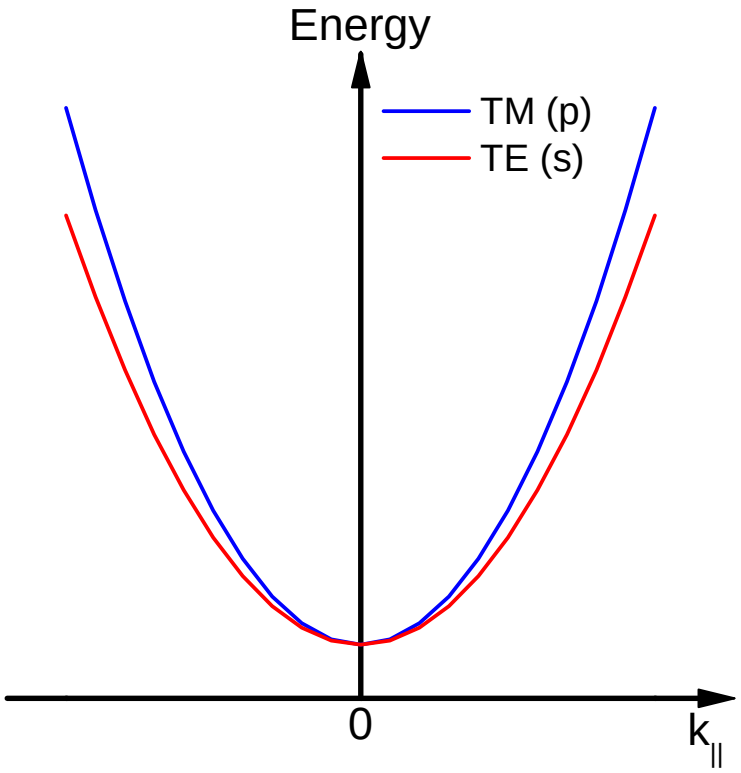

Figure 4.3: Dispersion relation of the TE-TM split cavity modes in a microcavity caused by the polarisation dependent phase reflection in the DBR mirrors.

excitonic components, which have total angular momentum of $J = \pm 1$. These bright $J = \pm 1$ states give rise to the spinor nature of polariton condensates since the condensate can consist of two components in the circular (σ^+/σ^-) polarisation basis. As we have seen in Section 3.5.2 the hemispherical cavity induces an almost harmonic confinement potential and supports mode profiles with a degree of cylindrical symmetry. This gives rise to transverse modes which carry a non-zero topological charge ($l \neq 0$) and have an orbital angular momentum of $\pm l\hbar$. This corresponds to a phase rotation of $2\pi l$ which can rotate clockwise (vortex) or anticlockwise (anti-vortex) around the mode core. We can write the azimuthal part of the vector LG modes as φ_{ls} where the spin momenta of the cavity polariton is denoted by $s = 1$ for σ^+ polarisation and $s = -1$ for σ^- polarisation. Considering the first excited manifold (FEM) associated with LG_{01}, and neglecting SO coupling, we can write the four degenerate eigenstates in the Jones vector formalism in

polar coordinates as:

$$
\begin{aligned}
LG_{01}^{\sigma^+} &= C(r)\varphi_{11}(\theta) = C(r)\begin{pmatrix} e^{i\theta} \\ 0 \end{pmatrix} \\
LG_{01}^{\sigma^-} &= C(r)\varphi_{-11}(\theta) = C(r)\begin{pmatrix} 0 \\ e^{i\theta} \end{pmatrix} \\
LG_{0-1}^{\sigma^+} &= C(r)\varphi_{1-1}(\theta) = C(r)\begin{pmatrix} e^{-i\theta} \\ 0 \end{pmatrix} \\
LG_{0-1}^{\sigma^-} &= C(r)\varphi_{-1-1}(\theta) = C(r)\begin{pmatrix} 0 \\ e^{-i\theta} \end{pmatrix},
\end{aligned}
$$

where θ is the real space angle and the circular polarisation basis is given by $\begin{pmatrix} 1 \\ 0 \end{pmatrix}$ and $\begin{pmatrix} 0 \\ 1 \end{pmatrix}$ representing σ^+ and σ^- polarisation respectively and $C(r)$ is the radial part of the normalized Laguerre-Gauss mode with $l \pm 1$. Polarisation dependent splitting in the cavity (TE-TM splitting) gives rise to an effective magnetic field [121] which couples the polariton pseudospin to its angular momentum, leading to an effective spin-orbit coupling. An example 2-dimensional cavity dispersion is shown in Fig 4.3 where the phase dependent reflection gives rise to two non-degenerate dispersions with different effective masses which gives rise to an effective magnetic field. Transfer matrix simulations show that for open cavities the large index contrast between the air gap and the semiconductor mirror gives rise to significantly larger TE-TM splitting in comparison to monolithic cavities. Hence a large SO coupling is expected. As discussed in Sala et al. [122], this SO coupling renders the total momentum $J = l + s$ a conservative quantity and thereby breaks the degeneracy among the φ_{ls} states, generating spin vortices. For the first co-rotating spin and angular momentum case, the total angular momentum is $J = \pm 2$, while for the second case of

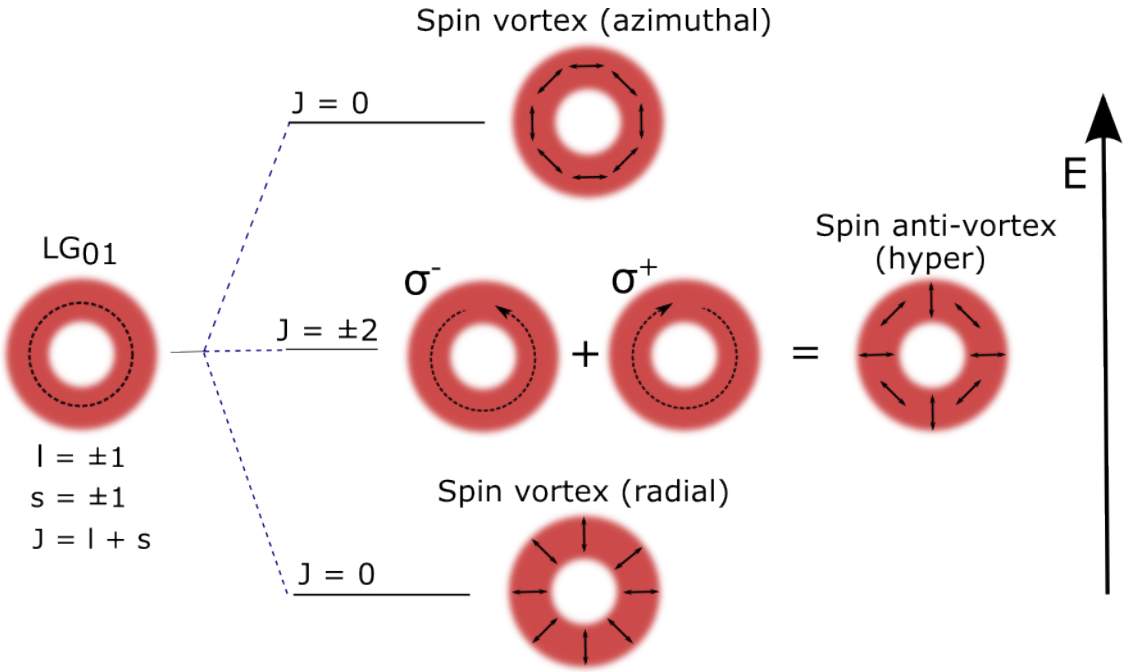

Figure 4.4: The splitting of the helical LG_{01} mode due to spin-orbit coupling. The introduction of TE-TM splitting in the cavity introduces SO coupling and lifts the degeneracy of the modes leading to three energy levels corresponding to $J = 1$ radial and azimuthal spin vortices, which are affected by the coupling, and the $J = \pm 2$ hyper spin anti-vortex which remains at the central energy.

counter rotating spin and angular momentum, $J = 0$. The introduction of a polarisation dependent splitting in the cavity lifts the degeneracy of the $J = 0$ cases due to an effective SO coupling [122] as shown in Fig. 4.4. The physical description of this effect was first presented by Foster et al. [123] where the mixing of LG phase vortices is caused by the polarisation dependent phase reflection in DBR mirrors [112].

Analytical simulations of the confined polariton system were developed and carried out by Dr. E. Cancellieri based upon the numerical solutions of a modified Gross-Piteavski equation (GPE). The modified GPE for the polariton wavefunction in a confinement potential can be written as:

$$i\hbar\frac{\partial\psi_{\pm}^{LP}}{\partial t} = -\frac{\hbar^2}{2m_{LP}^*}\bigtriangledown^2\psi_{\pm}^{LP} + V\psi_{\pm}^{LP} + \beta\left(\frac{\partial}{\partial x} \mp i\frac{\partial}{\partial y}\right)^2\psi_{\mp}^{LP} - \frac{\Omega}{2}e^{\mp i\theta}\psi_{\mp}^{LP} \tag{4.1}$$

where $\psi_{\pm}$ is the polariton wavefunction corresponding to σ^+/σ^- circularly polarised light, m^*_{LP} is the lower polariton effective mass, $V = \frac{1}{2}m^*_{LP}\omega^2(Ax^2 + By^2)$ is the confinement potential which is parabolic when $A = B$. The third term in Eq 4.1 determines the TE-TM splitting in the cavity and hence the strength of the SO coupling through the parameter $\beta = \hbar^2(1/m^{*TE}_{LP} - 1/m^{*TM}_{LP})/2$. β can be positive or negative depending on whether $m^{*TM}_{LP} > m^{*TE}_{LP}$ or $m^{*TE}_{LP} > m^{*TM}_{LP}$ where $m^{*TE/TM}$ are the effective masses in TE and TM dispersions. The final term adds birefringence to the model (TE-TM splitting at k = 0). In the most simple case we set the potential to be parabolic (A=B=1) and the birefringence to zero ($\Omega = 0$). The analytical solutions, treating the TE-TM splitting term as a perturbation, reveal four eigenstates of the system that are associated with the LG_{01} eigenmode with eigenenergies given by:

$$E_1 = E_0 - \frac{2\beta}{\sigma^2}$$
$$E_2 = E_3 = E_0$$
$$E_4 = E_0 + \frac{2\beta}{\sigma^2}$$

where $\sigma = \sqrt{\hbar/m_{LP}\omega}$ and determines the size of the harmonic confinement potential and E_0 is the energy of the LG_{01} mode. The basic model of a parabolic potential with TE-TM splitting predicts three energy levels with equidistant spacing for the first transverse mode manifold. In the circular polarisation basis the corresponding eigenfunctions can be written as:

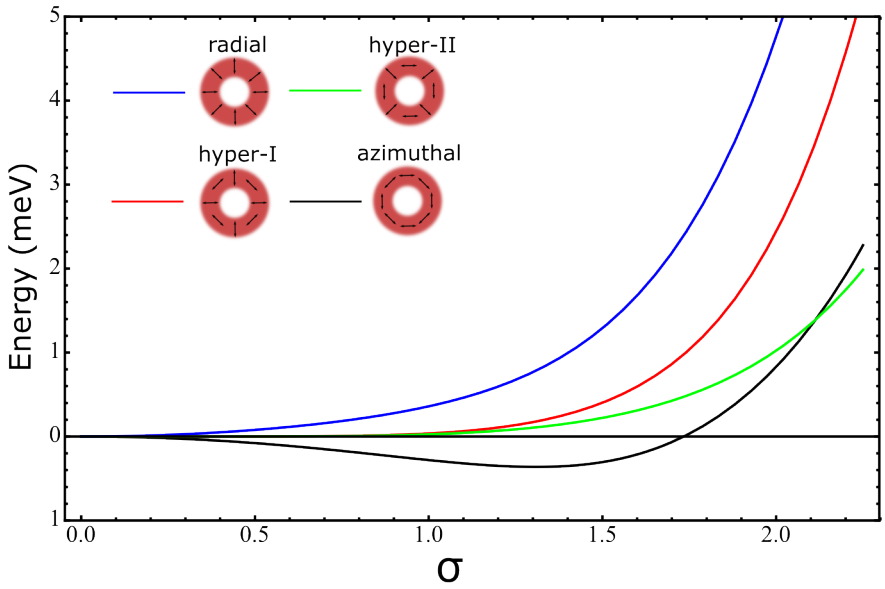

Figure 4.5: Eigenmode energies as a function of σ. The energy separation is determined by the complex interplay between $\beta = 0.1$, $A/B = 1.15$ and $\Omega = 0.05$ as a function of σ.

$$\begin{aligned}
\psi_1(r,\theta) &= \frac{1}{\sqrt{2}} C(r)[\varphi_{1-1}(\theta) + \varphi_{-11}(\theta+\pi)] \\
\psi_2(r,\theta) &= \frac{1}{\sqrt{2}} C(r)[\varphi_{11}(\theta) + \varphi_{-1-1}(\theta] \\
\psi_3(r,\theta) &= \frac{1}{\sqrt{2}} C(r)[\varphi_{11}(\theta) + \varphi_{-1-1}(\theta-\pi)] \\
\psi_4(r,\theta) &= \frac{1}{\sqrt{2}} C(r)[\varphi_{1-1}(\theta) + \varphi_{-11}(\theta)]
\end{aligned} \tag{4.2}$$

The eigenfunctions ψ_1 and ψ_4 are azimuthal and radial spin vortices respectively and have counter-rotating spin and angular momentum ($J = 0$) and are shown in Fig 4.4. These eigenmodes correspond to the 'TE' and 'TM' equivalent in helical transverse modes. Depending on the sign of β the position in energy of the radial and azimuthal spin vortices can switch. The $J = \pm 2$ case consisting of the degenerate eigenmodes ψ_2 and ψ_3, do not feel the SO coupling since the total angular momentum is not conserved ($J = \pm 2$). The coherent superposition of the $J = \pm 2$ modes then gives rise to a hyper-spin vortex if the

initial phase between the two components is fixed.

The previous discussion applies only to the case of a perfectly circular cavity where the confinement can be described by a harmonic potential. In reality, slight errors in fabrication will introduce an ellipticity into the potential which needs to be taken into account along with an additional birefringent term. The eigenfunctions of the GPE in the presence of an elliptical potential and birefringence become altered. The highest and lowest energy eigenmodes remain the azimuthal and radial spin vortices but the eigenmodes which do not feel the TE-TM splitting become mixed. This gives rise to two central hyper-spin anti-vortices as shown in the inset of Fig 4.5. Furthermore, the mode spacing becomes significantly altered through the additional structure. Fig 4.5 shows the eigenenergies as a function of σ. The energy spacing between the eigenmodes is no longer uniform as in the parabolic potential case and depending on the potential size it is possible for modes to switch position in energy. This non-uniformity in energy spacing is observed in Fig. 4.6 but only three spin vortices are observed experimentally. Detailed theoretical discussion of the eigenstates in the presence of both an elliptical potential and birefringence can be found in Appendix A.

4.4 Spin Vortices and Anti-vortices

In this section, the experimental observation of polariton spin-vortices is presented. The reduction in linewidth due to polariton condensation is required to resolve the modes presented in Fig 4.4. The same experimental set-up was used as for the case of the longitudinal mode (Section 4.2.2).

4.4.1 First Excited Manifold

The transverse mode spacing depends upon the degree of lateral confinement in the cavity. In the case of hemispherical resonators studied in this work, the lateral confinement is

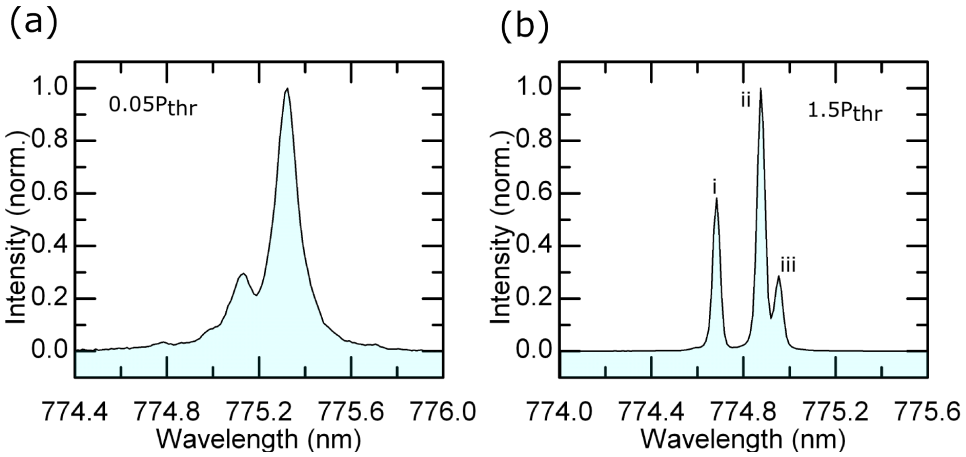

Figure 4.6: PL spectrum of the first excited manifold below threshold at with a photonic fraction of 64% (a) and above threshold (b). Three peaks become resolved due to the increased temporal coherence.

quantified by the beam waist size on the planar mirror. This in turn, is determined by the radius of curvature of the top mirror and the mirror separation. For the concave mirror radii of curvature of 20 μm and 7 μm the transverse mode spacing is around 14 meV and 22 meV when the mirror separation is around 1 μm. As such it is possible to tune any transverse mode close to resonance with the exciton and observe polariton condensation. The first excited manifold (FEM) associated with the transverse mode LG_{01}, carries a topological charge of $l = 1$, so corresponds to phase vortex or anti-vortex and as such, is expected to show complex spin textures due to SO coupling in the underlying mode structure as presented in the previous section. At low excitation power at a detuning corresponding to a photonic fraction of 64%, two broad peaks are present within the spectra as shown in Fig 4.6 (a). At a power of around 40 mW, a nonlinear increase in intensity is observed, which is associated with the build up in coherence as the linewidth drops from 270 μeV to the spectral resolution of the spectrometer of 50 μeV. This increase in coherence reveals further underlying structure as the low energy peak splits into a doublet - giving rise to a triplet of modes labelled i, ii and iii, as shown in Fig 4.6 (b). The energy splitting of ~ 0.56 meV observed between modes i and iii indicates strong SO interaction, consistent with transfer matrix simulations performed for the case of a planar

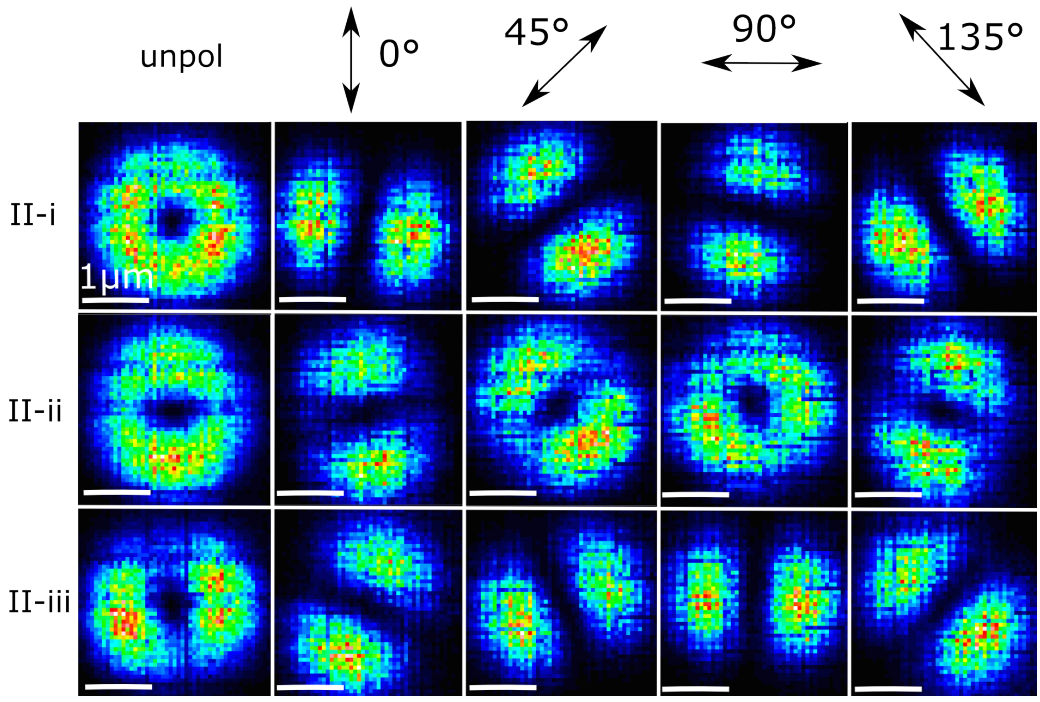

Figure 4.7: Tomographic images of the FEM polariton modes above threshold for unpolarised, 0°, 45°, 90° and 135° linear polarisations. Rotation of the intensity distribution with linearly polarised detection is present in all three of the modes. Scale bar is 1 μm.

open cavity revealing values of TE-TM splitting at high momenta of ~ 0.56 meV. The splitting between the three modes is not uniform, with modes i and iii having a splitting of 560 μeV compared to a splitting of 50 μeV between modes ii and iii. As presented in Fig. 4.5 this non-uniform spacing can be caused by the interplay between TE-TM splitting, cavity ellipticity and material birefringence. The i-iii energy splitting of 0.56 meV, along with $\sigma = 0.65$ μm obtained from the size of the spin-vortices indicates a SO coupling parameter $\beta = 0.06$ meV. μm^2. This value is around 3 times larger than that reported for monolithic cavities [116, 124, 115].

Tomographic Images

Fig. 4.7 shows the tomographic images of the three modes corresponding to the three modes of the FEM that are revealed above threshold. The pixel of the CCD selected to

construct the images corresponds to the centre of each of the three emission lines in the triplet. The unpolarised image of mode II-i displays perfect cylindrical symmetry and has the expected intensity profile of the LG_{01} eigenmode. Modes II-i and II-ii, which have a much smaller splitting of 50 μeV, show two lobes along orthogonal directions to each other. This contrasts with the mode profiles observed in Fig. 3.8 where broader linewidths prevent the underlying structure of the modes to be resolved.

Polarisation dependent collection, using a linear polariser and a quarter wave plate, was then introduced, allowing the measurement of the intensity distribution in the horizontal (0°) and vertical (90°) basis, the diagonal basis (45° and 135°) and the circular (σ^+/σ^-) basis. Fig 4.7 shows the clear rotation of the intensity distribution as a function of linearly polarised collection. Modes II-i and II-iii show orthogonally placed lobes as a function of polarised detection with a rotation in the clockwise direction. The central mode II-ii rotates in the anti-clockwise direction. The spatial polarisation can be further quantified by the linear polarisation angle.

Polarisation Maps

The linear polarisation angle is defined by $\phi = \arctan(S_2/S_1)$, where S_1 and S_2 are the Stokes parameters for linear and diagonal polarisations as defined in Section 1.3.1. This is related to the real space polarisation angle by $\theta = \phi/2$. Fig. 4.8 (a)(c)(e) show the linear polarisation angle in real space of mode II-i, II-ii and II-iii respectively, constructed from the Stokes parameters and (b)(d)(f) show the corresponding linear polarisation angle plotted against winding angle around the circular slice given by the white dashed line. The linear polarisation degree $\sqrt{S_1^2 + S_2^2} \approx 0.95$ is high for all modes. The 0° winding angle corresponds to the vertical white lines and rotates clockwise. This is in parallel to the 0° defined by the linear polariser axis. Hence, a clockwise rotation of the linear polarisation angle as a function of winding angle corresponds to a spin vortex and an anti-clockwise rotation corresponds to an anti-vortex.

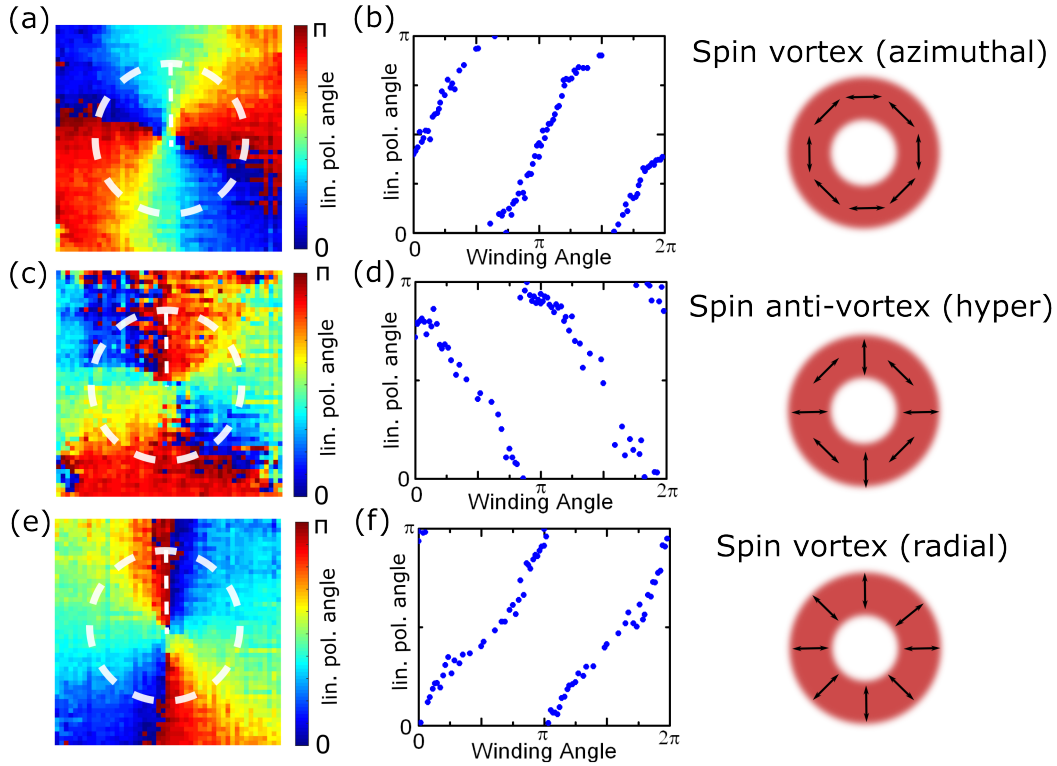

Figure 4.8: (a)(c)(e) Linear polarisation angle of modes II-i, II-ii and II-iii constructed from the Stokes parameters. (b)(d)(f) Linear polarisation angle vs winding angle. The winding angle is defined by the white dashed circle where 0° is defined as the vertical.

Mode II-i and II-iii show a clear 2π clockwise rotation of the linear polarisation angle around the core (Fig. 4.8(a) and (e)) indicating that the spin current is quantised and the eigenmodes are, in fact, spin vortices. The linear polarisation angle plots in Fig. 4.8(b) and (f) show a $\pi/2$ shift in the value of $\Delta = \phi - \theta$. These correspond to the azimuthal and radial spin vortices which arise from the SO coupling of the $J = 0$ eigenstates. The polarisation textures are sketched in the third column of Fig. 4.8. The central mode of the triplet shows an anti-clockwise winding (Fig. 4.8(d)), corresponding to a spin anti-vortex. The polarisation map reveals a hyperbolic-spin anti-vortex topography constructed from the coherent superposition of the $J = \pm 2$ eigenstates. As $J = \pm 2$ states are degenerate in energy, their phases can be pinned by structural defects inside the cavity or spontaneous symmetry breaking above the condensation threshold. Furthermore, ellipticity in the potential can couple the $J = \pm 2$ eigenstates to form new spin anti-vortex eigenstates as discussed in Section 4.3, but here we only observe a single spin anti-vortex as expected from the solutions of the GPE with a parabolic potential.

The tunability of the cavity allows full control of the exciton-photon detuning. When mode-II is tuned to more excitonic detunings, increasing the excitation power leads to condensation in the ground state mode-I, which is at a negative detuning. This limited the range of detunings of mode-II in which the modal structure above threshold could be studied. By using a smaller concave mirror radius of curvature of 7 μm, the transverse mode spacing is significantly increased, allowing threshold behaviour of mode-II to be observed at more excitonic detunings.

4.4.2 Excitonic Component Influence

Fig. 4.9 displays the spectra of the mode II components in a cavity with a 7 μm RoC concave mirror above condensation threshold. The mode splitting in the most photonic detuning corresponding to a photonic fraction of 82% is 1.02 meV between modes II-i and II-ii and 0.13 meV between modes II-ii and II-iii. In the most excitonic case where polari-

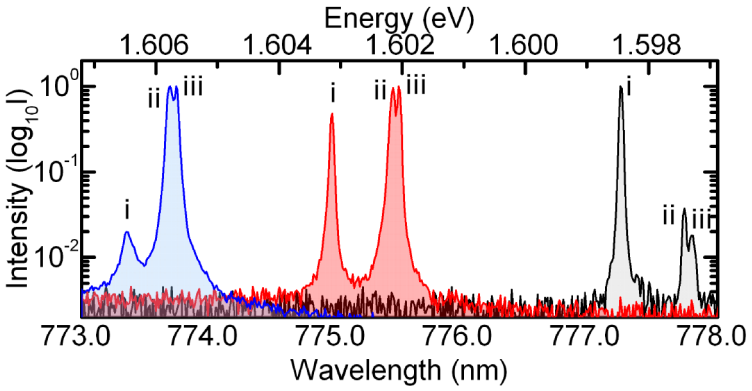

Figure 4.9: PL spectra at P = $2P_{th}$ for three detunings above threshold. The three photonic components are 42% (blue), 61% (red) and 82% (black).

ton lasing was observed, the splitting above threshold is reduced between modes II-i and II-ii to 0.71 meV and 0.11 meV between modes II-ii and II-iii. This provides conclusive evidence that the strong coupling is preserved above threshold as this reduction in the photonic splitting between modes is a direct consequence of the excitonic component of the polariton. The SO coupling is a photonic effect so becomes suppressed with increasing exciton fraction of the polariton. The detuning of the modes also leads to different preferential stimulated relaxation in either mode II-i, in the most photonic case, or into modes II-ii and II-iii in the most excitonic case. At an intermediate detuning between the two extremes, the three peaks have comparable intensities and no mode is preferentially selected up to the maximum pump power of P = $2P_{th}$.

The tomographic images of the three modes corresponding to modes II-i, II-ii and II-iii at the largest photonic component of 82% above threshold (black trace Fig. 4.9) are shown in Fig. 4.10 (a)(d)(g). These images are comparable to those shown in the case of a cavity formed with 20 μm RoC in Fig. 4.7 where the high energy mode shows a cylindrically symmetric helical LG_{01} and the low energy modes II-ii and II-iii have orthogonal lobe profiles. As in the case of the 20 μm RoC cavity, the three modes show a spatially dependent linear polarisation. The linear polarisation angle is plotted in Fig 4.10 (b)(e)(h) along with the corresponding dependence on the winding angle (c)(f)(i). The high energy

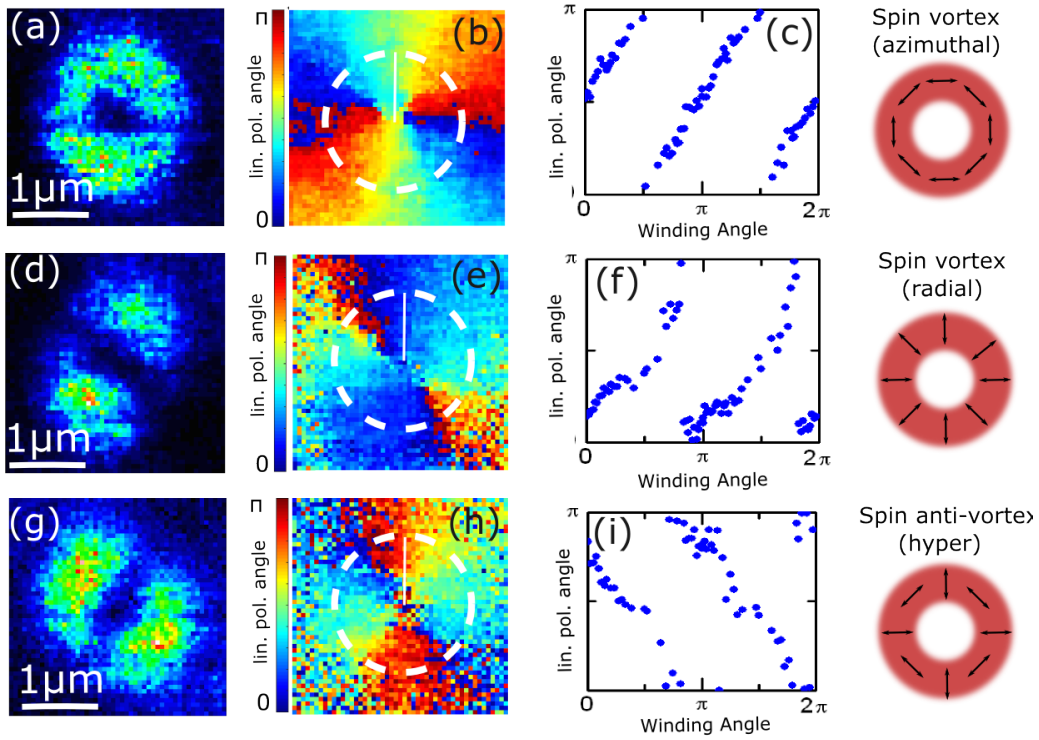

Figure 4.10: (a)(d)(g) Real space tomographic images of modes i, ii and iii corresponding to the mode in the black trace in Fig. 4.9. (b)(e)(h) Spatial colourmap of the linear polarisation angle for each mode and the corresponding angular windings (c)(f)(i) for the the largest photonic component of 82%.

member of the triplet again shows a clockwise rotation in linear polarisation angle with an azimuthal spin vortex structure ($J = 0$). In contrast to the 20 μm RoC case, the low energy mode II-iii corresponds to the $J = \pm 2$ hyper-spin anti-vortex while the central mode II-ii corresponds to the radial spin vortex ($J = 0$). The experimental observations show that this mode is shifted relative to the central position in the case of RoC = 20 μm and shifted to an energy below the radial spin vortex for the RoC = 7 μm case. The shifting of the relative eigenenergies is related to the interplay between SO coupling, ellipticity of the concave mirror and birefringence as shown in Fig. 4.5 which can change between different concave mirrors due to fabrication imperfections. In all experimental cases only three modes are present within the spectra as expected in the case of a parabolic potential (Fig. 4.4), and not four as expected from the GPE solutions including cavity ellipticity (Fig. 4.5), but the modes have a non-uniform energy spacing as expected from the latter case. This discrepancy is not currently accounted for but may be related to the relaxation competition between the different modes which preferentially scatter into the the observed eigenmodes.

As discussed in the previous section, the increased mode spacing in the 7 μm RoC cavity of around 20 meV allows polariton lasing to be observed a photonic fraction of 42%. This is because there is a particular range of polariton energies below exciton level where polariton relaxation is the most efficient [125, 59]. The increased mode spacing places the longitudinal mode at a very large negative detuning where relaxation is inefficient and threshold behaviour cannot be observed. As such, a more excitonic polariton for mode II can be studied above threshold. Fi.g 4.11 (a)(d)(g) show the tomographic images of the mode II peaks above polariton lasing threshold observed at the most excitonic detuning with a photonic fraction of 42%. These correspond to the blue spectrum in Fig. 4.9. As seen in Fig. 4.11 (b) and (c), mode II-i remains an azimuthal spin vortex. In contrast to this, modes II-ii and II-iii show non-trivial changes in comparison to the photonic case. Instead the lobe structure of the mode is pinned vertically in the case of mode II-ii (Fig. 4.11(d)) and horizontally in the case of mode II-iii (Fig. 4.11(g)). Furthermore, the

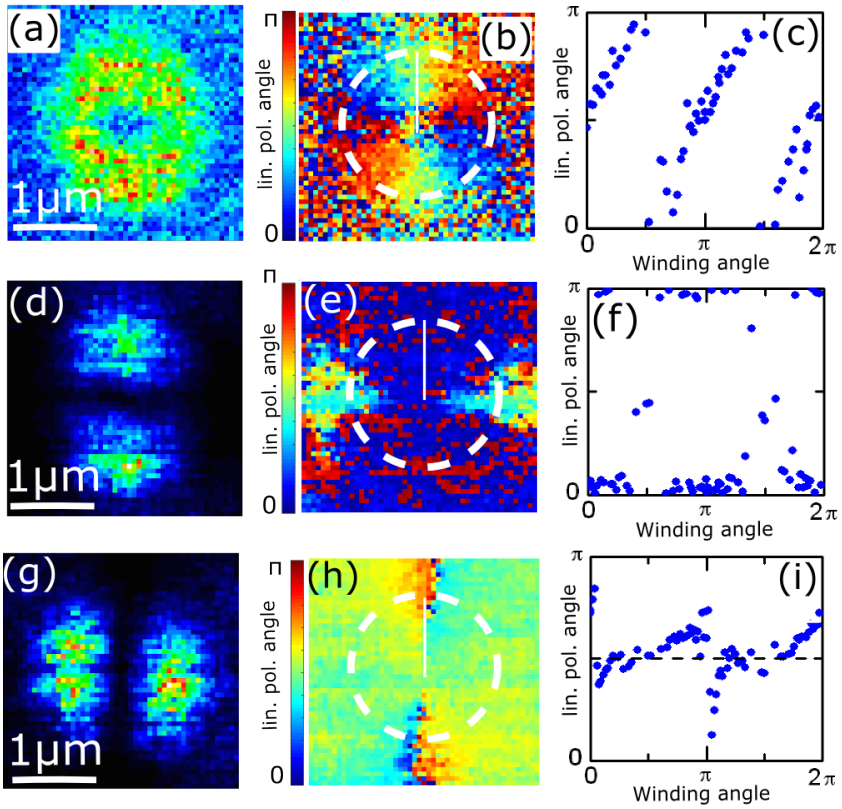

Figure 4.11: (a)(d)(g) Tomographic images of modes II-i, II-ii and II-iii with a photonic component of 42% corresponding to the blue spectrum in Fig 4.9. (b)(e)(h) Spatial colourmap of linear polarisation angle for the corresponding modes. (c)(f)(i) Linear polarisation angle for mode II-i, II-ii and II-iii showing where the polarisation is lost for the case of II-ii and II-iii.

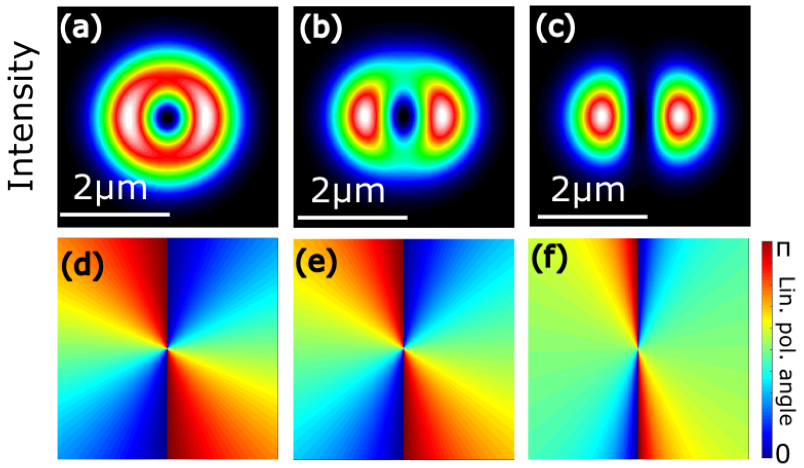

Figure 4.12: (a)(b)(c) Theoretical intensity distribution of the radial spin vortex in the presence of an elliptical potential for decreasing SO-coupling parameter (β). (d)(e)(f) Corresponding linear polarisation angle. A transition from spin vortex to linear polarisation occur when the TE-TM splitting becomes reduced. Experimentally, this is observed when at more excitonic detunings.

linear polarisation angles shown in Fig. 4.11 (f) and (i) show that the spatial rotation of the polarisation angle is lost in the areas of maximum intensity and instead corresponds to a flat angle of $0(\pi)$ for mode II-iii and $\pi/2$ for mode II-iii (Fig. 4.11 (h) and (i)). Hence the increased excitonic component of the polariton condensate leads to the formation of linearly polarised states in the lowest energy states, which are the eigenstates of elliptical cavities.

The loss of the spin vortex structure can be understood through a reduction of the SO coupling. Since it is a purely photonic effect, increasing the excitonic component of the polariton condensate reduces the splitting due to SO coupling allowing the ellipticity of the harmonic potential to dominate and produce linearly polarised modes. Experimentally we see this reduction in SO coupling from the i-iii splitting which decrease from 1.02 meV at 82% photonic fraction to 0.71 meV at 42% photonic fraction. Fig. 4.12 shows both the theoretical intensity distribution (a)(b)(c) and corresponding linear polarisation angle (d)(e)(f) of the radial polarisation vortex for decreasing SO coupling (β) in the presence

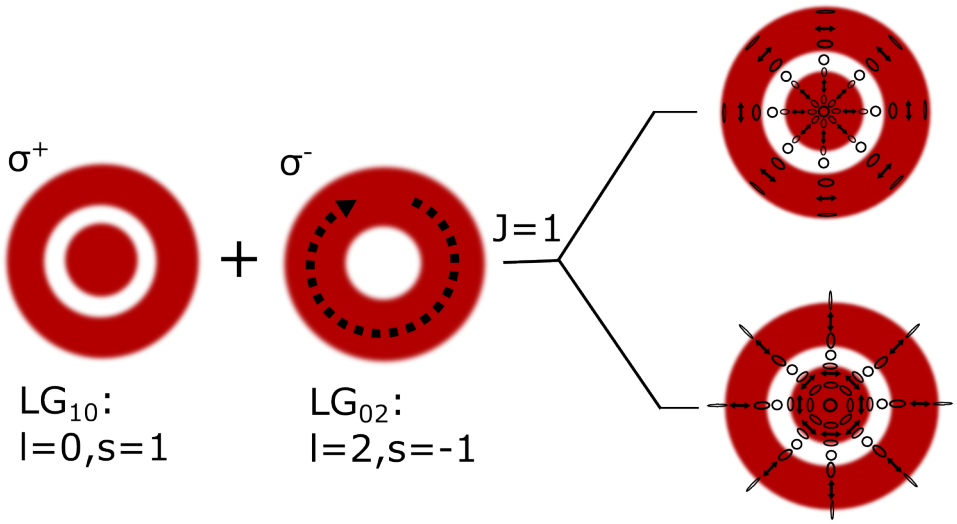

Figure 4.13: Mode III consists of the degenerate LG_{02} 4π phase vortex and the LG_{10} non vortex. The superposition of the $J = 1$ states $\sigma^{-}LG_{02}$ spin vortex and the $\sigma^{+}LG_{10}$ give rise to two new eigenstates with an azimuthal (radial) spin vortex in the outer core with a radial (azimuthal) rotation in the central region.

of an elliptical potential. A reduction in SO coupling results in a clear transition from a radial spin vortex to a linearly polarised mode mode, in agreement with experiment. This indicates that the spin texture of the condensate is strongly linked to its polaritonic nature, rather than being an entirely photonic effect.

4.4.3 Second Excited Manifold

One advantage of using a tunable system is the ability to arbitrarily select higher order transverse LG modes. The 2^{nd} transverse mode in a cylindrically symmetric system consists of two modes; LG_{02} and LG_{10}, which are degenerate in energy since $2p+|l|$ is the same for both modes [126]. In this case, the LG_{02} mode carries angular momentum with a topological charge $l = |2|$, corresponding to a phase winding of $\pm 4\pi$, and LG_{10} is azimuthally uniform in phase ($l = 0$) but with a π-phase shift at the radial node. Similarly to the LG_{01} case, modes which carry the same total angular momentum J, become coupled and form new eigenstates due to SO coupling. We refer to these modes as the second excited manifold (SEM). Fig. 4.13 plots this for the $J = 1$ case where the coherent combination of

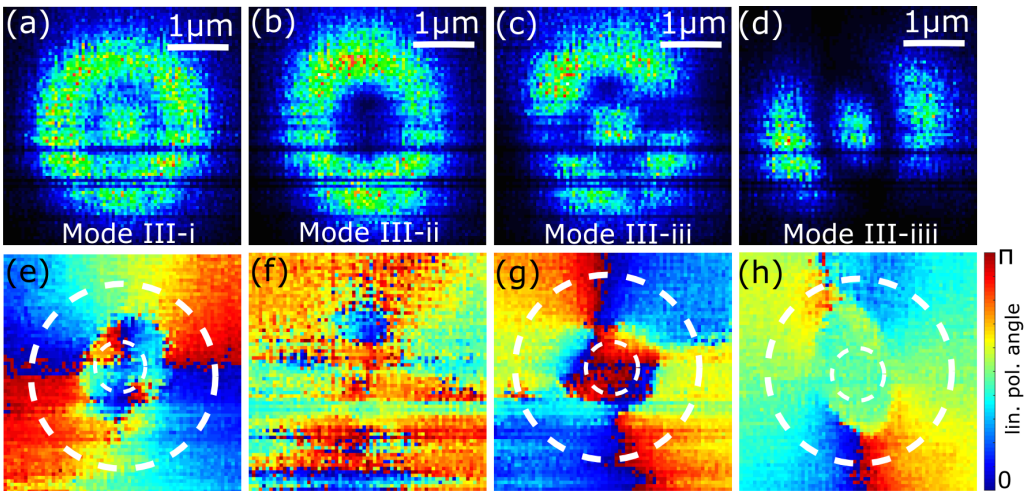

Figure 4.14: (a)(b)(c)(d) Tomographic images of the four modes resolved above threshold for SEM. (e)(f)(g)(h) Corresponding linear polarisation angle colourmap for each mode.

$\sigma^+ LG_{10}(l=0)$ and $\sigma^- LG_{02}(l=2)$ modes gives rise to a mode with a spin pattern which consists of and outer linear polarisation winding which is offset by $\Delta = \phi - \theta = \pi/2$. In general, the new eigenmodes have an azimuthal (radial) spin vortex in the outer core and a radial (azimuthal) spin vortex in the inner core along with elliptical and circularly polarised components along their radii as shown in Fig. 4.13.

Fig. 4.14 (a)(b)(c)(d) show experimental tomographic images of the the four constituents of mode-III above condensation threshold at negative detuning. Below threshold the modes cannot all be resolved. Fig. 4.14 (a) shows the expected intensity profile for the superposition of LG_{02} and LG_{10} consisting of an outer ring and an inner maximum. The second mode shown in Fig 4.14 (b) shows a slightly elliptical ring which appears to correspond to LG_{02}. The two lowest energy modes show elliptical features of the $MG_{2,1}o$ modes in (c) and the $MG_{2,1}e$ mode in (d) which is related to the elliptical cavity potential.

The linear polarisation angle is plotted for each mode in Fig 4.14 (e)(f)(g)(h). Mode III-i, plotted in Fig. 4.14 (e), shows two windings of the linear polarisation angle. The outer rotation corresponds to the azimuthal spin vortex , while the inner shows a radial

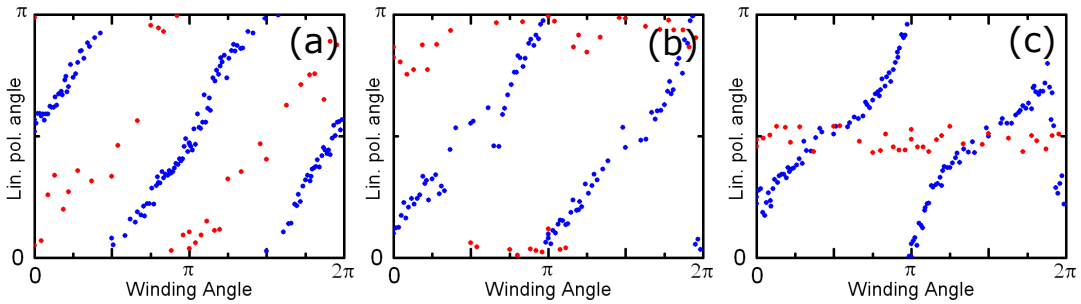

Figure 4.15: Linear polarisation angles around the outer core (blue trace) and inner core (red trace) in Fig 4.14. (a) Mode III-i. (b) Mode III-iii (c) Mode III-iiii.

spin vortex as presented theoretically in Fig. 4.13. The two linear polarisation angles are plotted in Fig. 4.15, where the blue trace corresponds to the outer winding and the red trace to the inner. Fig. 4.14 (f) shows the same plot for mode III-ii. Here there is no rotation of the polarisation angle and the mode does not correspond to a polarisation vortex.

Both mode III-iii and III-iiii (Fig. 4.14 (g) and (h)) have the same outer linear polarisation angle windings shifted by $\pi/2$ in comparison to the high energy mode III-i. These profiles are radial spin vortices. Interestingly, the central region of mode III-iii shows a linear vertical polarisation while the central region of mode III-iiii shows a horizontally polarised region (Fig. 4.14 (b) and (c)). The imperfection of the spatial profile and polarisation winding in the inner core compared to mode III-i is likely linked to the ellipticity of the cavity since MG features are present in the spatial intensity distribution of mode III-iii and III-iiii but not in III-i.

4.5 2-Dimensional Polaritons

The open cavity system supports the formation of 2-dimensional polaritons through use of the area surrounding the concave mirror arrays. By removing the concave areas from the optical path the planar-planar DBR areas of the top and bottom samples can be used to form a planar Fabry-Perot type cavity with full tunability. There is translational

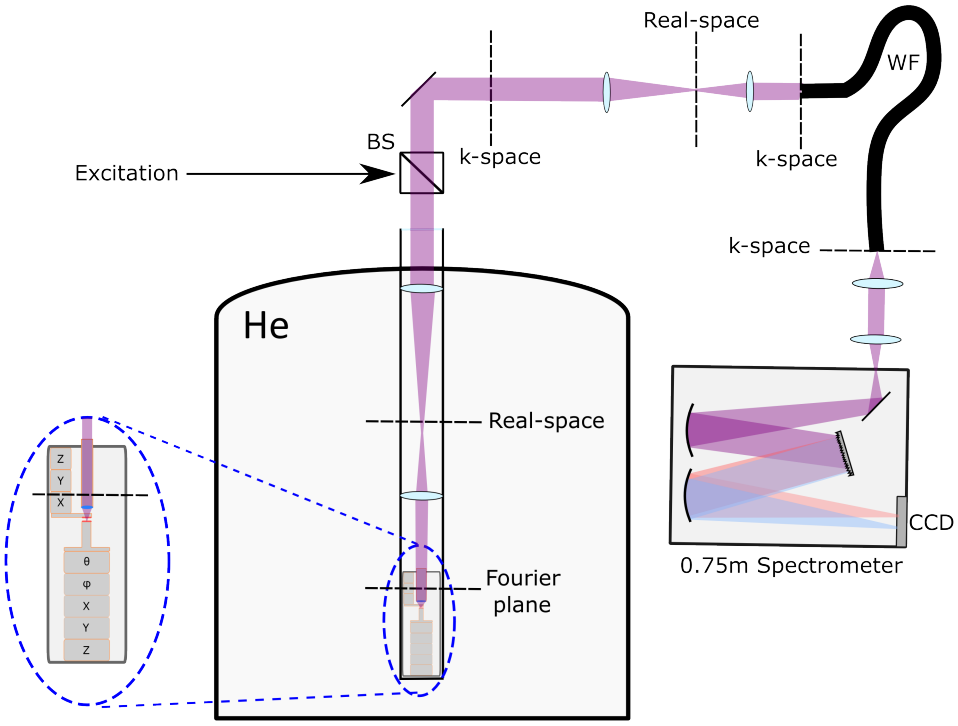

Figure 4.16: Fourier imaging set-up. Two confocal lenses are placed within the cryostat tube in order to image and project the Fourier plane onto the optical table above. A second set of confocal lenses then form the k-space image onto the end facet of a wound fibre bundle. The k-space image is then re-imaged on the other end of the WF and focused onto the spectrometer slits.

symmetry in the direction perpendicular to the growth giving rise to 2-dimensional cavity modes. The top and bottom DBRs are the same as used in the previous sections and consist of a 12 GaAs QW bottom semiconductor DBR and a top dielectric concave DBR. Typically, a very high degree of parallelism is required between the top and bottom mirrors in order to form high Q-factor 2-dimensional modes where the beam walk off has been minimised. This is achievable in the cavity system due to the ability to perform in-situ tuning in the relative angle between mirrors (ϕ and θ).

Fig. 4.16 shows the Fourier imaging system used to perform angular resolved spectroscopy on the planar-planar open cavity. Two confocal lenses are placed inside the bath cryostat to first image the Fourier plane and then to project this image onto the small optical

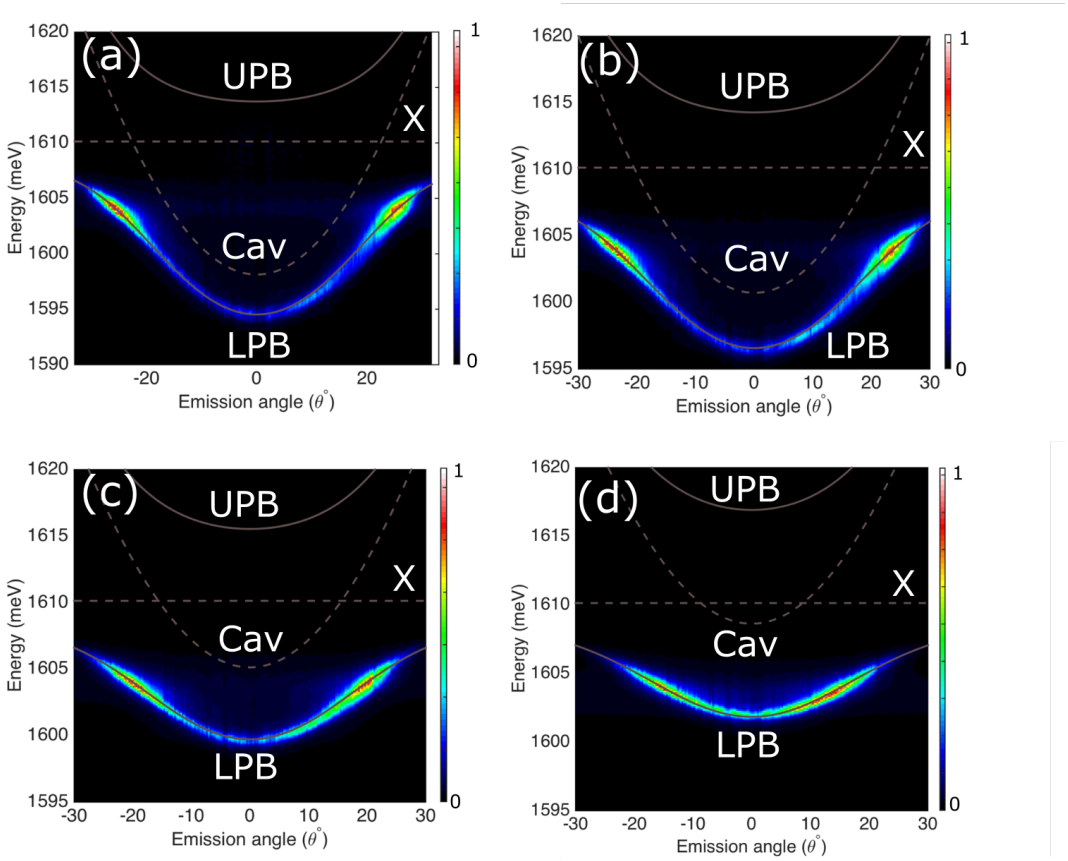

Figure 4.17: Angular resolved spectra of lower polariton branches for detuning of (a) $\delta = -12$ meV, (b) $\delta = -9.4$ meV, (c) $\delta = -5$ meV and (d) $\delta = -1.5$ meV. The Rabi splitting is 15 meV.

table placed above. A second set of confocal lenses then re-image the Fourier plane onto the end facet of the wound fibre bundle. A real space image of the opposite end facet is then formed on the slits of the spectrometer which corresponds to the k-space polariton dispersion. Non-resonant excitation is performed using a 630 nm laser diode with a spot size on the sample of around 30 μm.

4.5.1 Polariton Dispersion

Fig. 4.17 shows the angular resolved spectra of lower polariton branches for detuning of (a) $\delta = -12$ meV, $\delta = -9.4$ meV (b), $\delta = -5$ meV (c) and (d) $\delta = -1.5$ meV at low

pumping power. The mirror separation is around 1 μm and the Rabi splitting is 15 meV at zero detuning. The ability to select the exciton-photon detuning in-situ is performed through applying a DC voltage to the bottom z-nanopositioner. This reduces the mirror separation and shifts the cavity mode to higher energy; increasing the excitonic component of the lower polariton branch. In Fig. 4.17 (a) (b) and (c) the accumulation of polaritons occurs at an angle of 20 - 25°. This was discussed in Section 1.3.3 where the lifetime of the polaritons becomes too short for efficient relaxation, leading to a bottleneck effect at finite k-vector. This regime is known as the kinetic regime, where relaxation is difficult due to the phonon assisted relaxation time being larger than the polariton lifetime. This causes the system to be strongly out of thermal equilibrium. Crucially for condensation, a larger photonic component of the polariton leads to a smaller polariton effective mass, which lowers the required critical density required for condensation. In the case close to resonance with a detuning of $\delta = -1.5$ meV shown in Fig. 4.17 (d), the bottleneck effect is suppressed and relaxation towards k = 0 is more efficient since the relaxation time approaches the polariton lifetime. This is due to the larger excitonic component, which increases the polariton lifetime and reduces the depth of the LPB branch. Hence fewer scattering events are required to populate the low k-vector states. In this regime, quasi-thermodynamic equilibrium can be achieved where the polaritonic system can have a well defined temperature which is not necessarily the same as the surrounding lattice temperature [7].

The ability to observe 2-dimensional polaritons along with strongly confined 0-dimensional polaritons on the same sample with complete spectral tunability significantly increases the possible experimental applications of the tunable cavity system. In the next section strong evidence for 2-dimensional polariton condensation is presented.

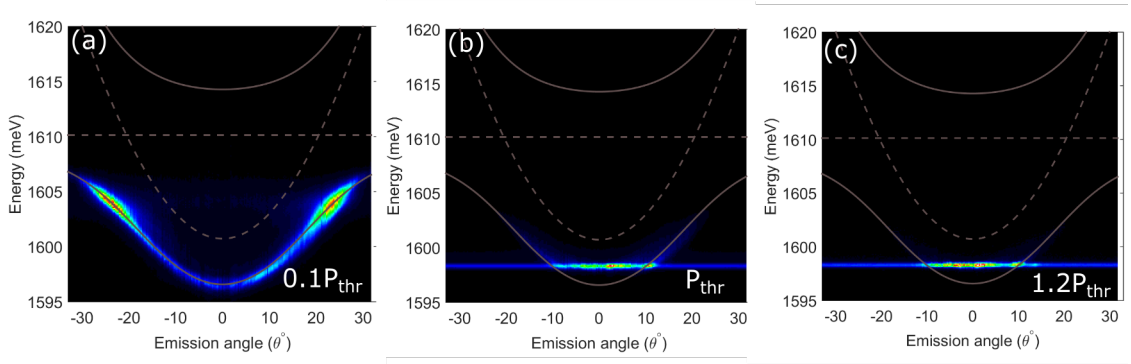

Figure 4.18: Angular resolved 2-dimensional polariton dispersion at $\delta = -9.4$ meV. (a) P = 0.1 P_{thr}. (b) P = P_{thr}. (c) P = 1.2 P_{thr}. A condensate centred around k = 0 is observed above threshold with some contribution form $k \neq 0$ states. The horizontal line outside of the condensate is an optical artefact arising from the CCD readout without a shutter.

4.5.2 2-dimensional Polariton Condensation

The angular resolved spectra of the lower polariton branch is shown in Fig 4.18 (a) at a detuning of δ = -9.4 meV (- 0.6 Ω_{Rabi}). The pump power in this case is 2 mW, which corresponds to the low excitation density regime, so the bottleneck effect at an angle of around ± 25° is clearly evident as discussed in Section 1.3.3. As the pump power is increased, polaritons begin to accumulate at 0° slightly blueshifted from the bare LPB dispersion due to polariton-polariton interaction. Fig. 4.18 (b) shows the angular dispersion at the threshold power of around 50 mW. Here the condensate is centred around $\theta = 0°$ but extends out to the LPB dispersion, ± 11°. It has been shown theoretically that condensation can occur in momentum space with $k \neq 0$ due to a combination of excitation spot size and localised states in disordered cavities [127] or due to ballistic propagation of polaritons out of the high density region determined by the pump spot [128]. In our case the condensate forms close to $k = 0$ with some contribution at $k \neq 0$ states. Similar behavior was observed in GaAs condensates at negative detunings and was attributed to the weaker nonlinear interactions in more photonic condensates and the deeper trap, preventing efficient relaxation to $k = 0$ [57]. The low intensity dispersion that is visible at threshold has the same curvature of the dispersion observed at lower power in Fig 4.18 (a).

Crucially, the non-parabolic nature combined with the point of inflection at high angle indicates that the strong coupling regime is preserved. Increasing the power further leads to non-linear increase in intensity from the condensate and the polariton dispersion is no longer observed. Fig 4.18 (c) shows the angular resolved spectrum at 1.2 P_{thr} where only the condensate is visible. It extends to an angle of $\pm$ 11°, corresponding to the edges of the bare polariton dispersion, shown in Fig. 4.18 (a). Similar condensation behaviour was observed at more positive detunings of -55 and -1.5 meV as shown in where the increased interaction strength due to the larger excitonic component allows efficient relaxation to $k = 0$ giving rise to a narrow condesate in k-space.

Power Dependence

The power dependence extracted from Fig. 4.18 is shown in Fig. 4.19. At k = 0, clear threshold behaviour is observed at a power of 50 mW and is associated with a nonlinear increase in intensity. At threshold, the linewidth decreases from 1 meV to 200 μeV. Finally, the total blueshift of around 1.8 meV is much smaller than the LPB-bare cavity separation of 5.3 meV, providing further evidence that the nonlinear increase in intensity and associated build up of temporal coherence is associated with polariton condensation. The pumping laser limited the accessible powers so that the full non-linear intensity increase could not be fully passed.

4.6 Summary

In this chapter, polariton condensation in strongly confined transverse modes was presented where the increased temporal coherence reveals the spontaneous formation of coexisting spin vortices. These spin vortices and other textures arise from an effective SO coupling which couples states of the same total angular momentum. This SO coupling is a result of TE-TM splitting in the microcavity due to the difference in reflection phase for

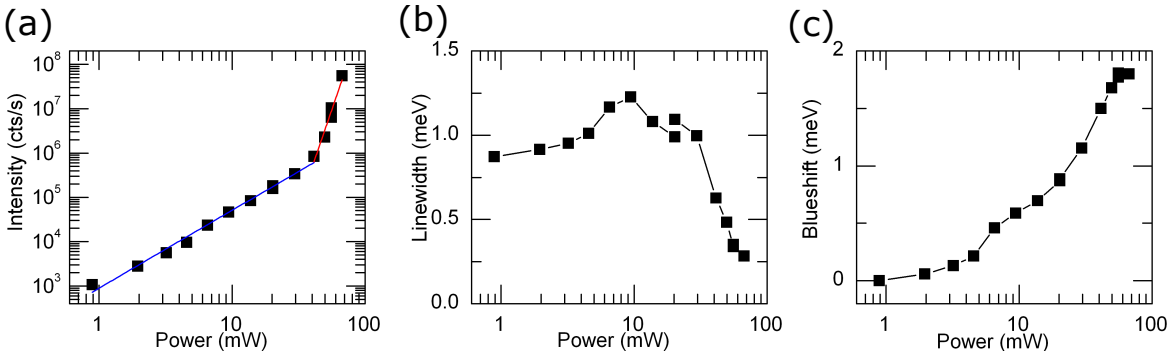

Figure 4.19: Power dependence at k = 0 with $\delta = -9.4$ meV. (a) Nonlinear increase in intensity at around P = 50 mW. (b) Build up of temporal coherence corresponding to a drop in linewidth from 1 meV to 200 μeV at threshold. (c) Blueshift of LPB to a maximum of 1.8 meV. In contrast to the 5.7 meV distance to the bare cavity mode.

different polarisations, which is increased in systems containing an air gap in comparison to monolithic cavities. The exciton fraction of the polariton condensate was found to significantly alter the spin texture, causing a transition from spin vortices/anti-vortices to linearly polarised MG modes. The ability to flexibly manipulate the polariton condensate through both the spin and angular momentum by changing the excitonic component in-situ, will potentially bring rich physical insights when operating at the single particle level [76, 5]. Finally, evidence of polariton condensation in negatively detuned 2-dimensional modes was also presented.

Chapter 5

Tunable Polaritonic Molecules

5.1 Introduction

Photonic molecules are two or more coupled electromagnetically interacting microcavities. To form a photonic molecule, two microcavities are brought together so that their photonic modes interact, leading to a hybridisation and the formation of bonding (symmetrical) and anti-bonding (anti-symmetrical) modes and the formation of a photonic molecule [1]. This splitting is analogous to the electronic states found in diatomic molecules such as H_2, where the coulomb interaction between the atoms causes a splitting of the degenerate atomic orbitals into bonding and anti-bonding electron orbitals. In the atomic case, the bonding strength is determined by the degree of the coulomb interaction between the nuclei and the electrons. In photonic molecules, the interaction between the coupled cavities is due to the electromagnetic field overlap. This is determined by the geometry of the cavities themselves and can be controlled through the design of the coupling channel. For the coupled open cavities described in this chapter, the coupling is due to modal overlap which is determined by the centre-to-centre distances between adjacent cavities. To date, applications in the field of polaritonics have been polariton condensation in diatomic photonic molecules based upon coupled micropillars [2] and the observation of Josephson

oscillations between two linked polariton condensates [129]. Furthermore, coupled cavities which contain a weak nonlinearity are expected to show strong photon antibunching as discussed in Section 1.6.4 [5, 130].

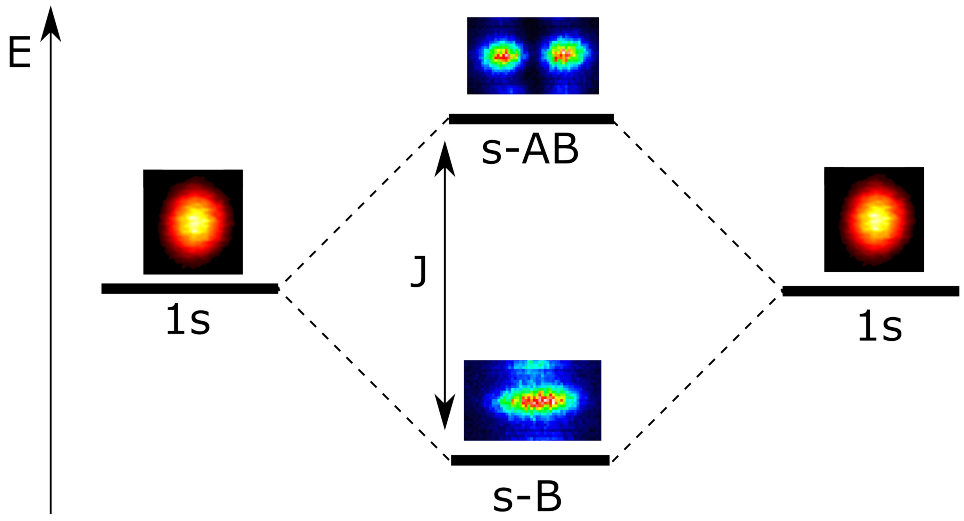

Figure 5.1: Lifting of degeneracy in a photonic molecule due to formation of bonded and anti-bonded photonic modes with coupling strength J.

In this Chapter, tunable diatomic photonic molecules with strong lateral confinement are studied. These cavities are in the strong coupling regime and are hence termed polaritonic molecules. The cavity resonance energy of the individual coupled cavities can be arbitrarily tuned through both the mirror separation and the relative angle between the top and bottom mirrors. The transition from coupled to uncoupled cavities is demonstrated through tomographic imaging, revealing a transition from bonding/anti-bonding modes to the independent longitudinal cavity modes. A large polarisation splitting is observed leading to two non-degenerate linearly polarised pairs of bonding/anti-bonding eigenmodes when the individual cavities are tuned into resonance. These linearly polarised states are the experimental demonstration of the coupled cavity system in the theoretical proposal in Bamba *et al.* (2010) where the polarisation degree of freedom in coupled cavities with a weak nonlinearity is neglected in the theoretical explanation of photon antibunching.

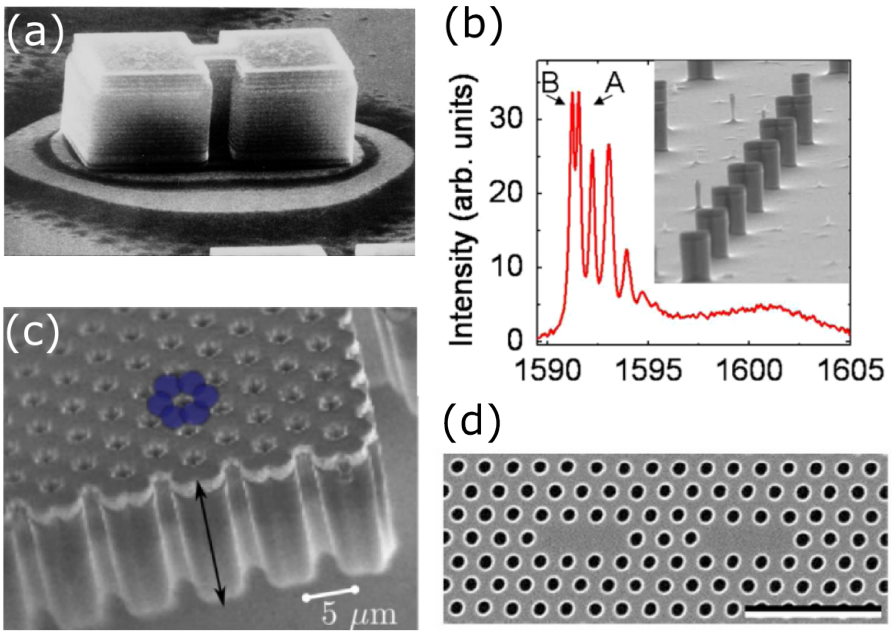

Figure 5.2: SEM images of photonic molecules. (a) Coupled square micropillars [1]. (b) Coupled cylindrical micropillars [2]. (c) Honeycomb lattice of coupled micropillars [3]. (d) Coupled L3 photonic crystal cavities [4].

5.2 State of the Art

In the most simple case, two microcavities are brought together so that their photonic modes interact, leading to hybridisation and the formation of bonding and anti-bonding modes with an energy splitting determined by the tunnelling strength J, as shown in Fig. 5.1. The interaction between the photonic modes is determined by the geometry of the constituent cavities, and for micropillars, can be conventionally controlled through the centre-to-centre distance which determines the modal overlap between the cavities [131]. The initial demonstrations of lithographically fabricated photonic molecules coupled two adjacent cavities, leading to a direct analogy with a simple diatomic molecule, shown in Fig. 5.2 (a) [1]. More complicated structures have since been developed such as a honeycomb lattice, where the structure of the coupled cavity array supports confined modes comparable to that of the molecular orbitals of its chemical counterpart (Fig. 5.2 (c)) [3].

Alternative typical configurations of photonic molecules exist such as cylindrical coupled cavities (Fig. 5.2 (b)) [2]; coupled defects in photonic crystal membranes (Fig. 5.2 (d)) [4]; whispering-gallery microdisks, coupled via a small air gap [132]; and planar Fabry-Perot cavities, coupled through a partially transparent DBR [133]. In all the mentioned cases, the cavity energy and the tunnelling strength is fixed through fabrication, limiting the ability to tune the cavity modes into resonance with an emitter as well as in-situ tuning of the cavity tunnelling rate. Moreover, it is not possible to simultaneously achieve submicron confinement and narrow polariton linewidths in micropillars. In 3 μm micropillars, 15 quantum wells were required to obtain a lower polariton linewidth of 200 μeV. Such large numbers of quantum wells significantly reduce the nonlinear polariton-polariton interaction strength which scales with $1/N$. In open cavities with polariton confinement, we are able to demonstrate polaritons with linewidths of 150 μeV in a sample containing a single quantum well. In this respect, the demonstration of polaritonic molecules with open microcavities allows the achievement of both high Q-factors and strong lateral confinement in a sample with a single quantum well, paving the way towards studies of quantum polaritons.

5.3 Polaritonic Molecule Characterisation

As discussed in Chapters 2 and 3, the open cavity system consists of two individual stacks of attocube xyz-nanopositioners, allowing full spectral and spatial control over the two DBRs [134]. To reach submicron mirror separations, two goniometer nanopositioners are used to control the relative angle between the two samples in both θ and ϕ and achieve a high degree of parallelism. In order to couple two microcavities, confinement is required and is introduced by the hemispherical cavity geometry [134]. The planar semiconductor mirror consists of a 31 paired $Al_{0.85}GaAs/GaAs$ DBR with a single $In_{0.04}GaAs$ QW surrounded by $GaAs$ barriers in a λ cavity region at an E-field antinode as shown in Figure 5.3.

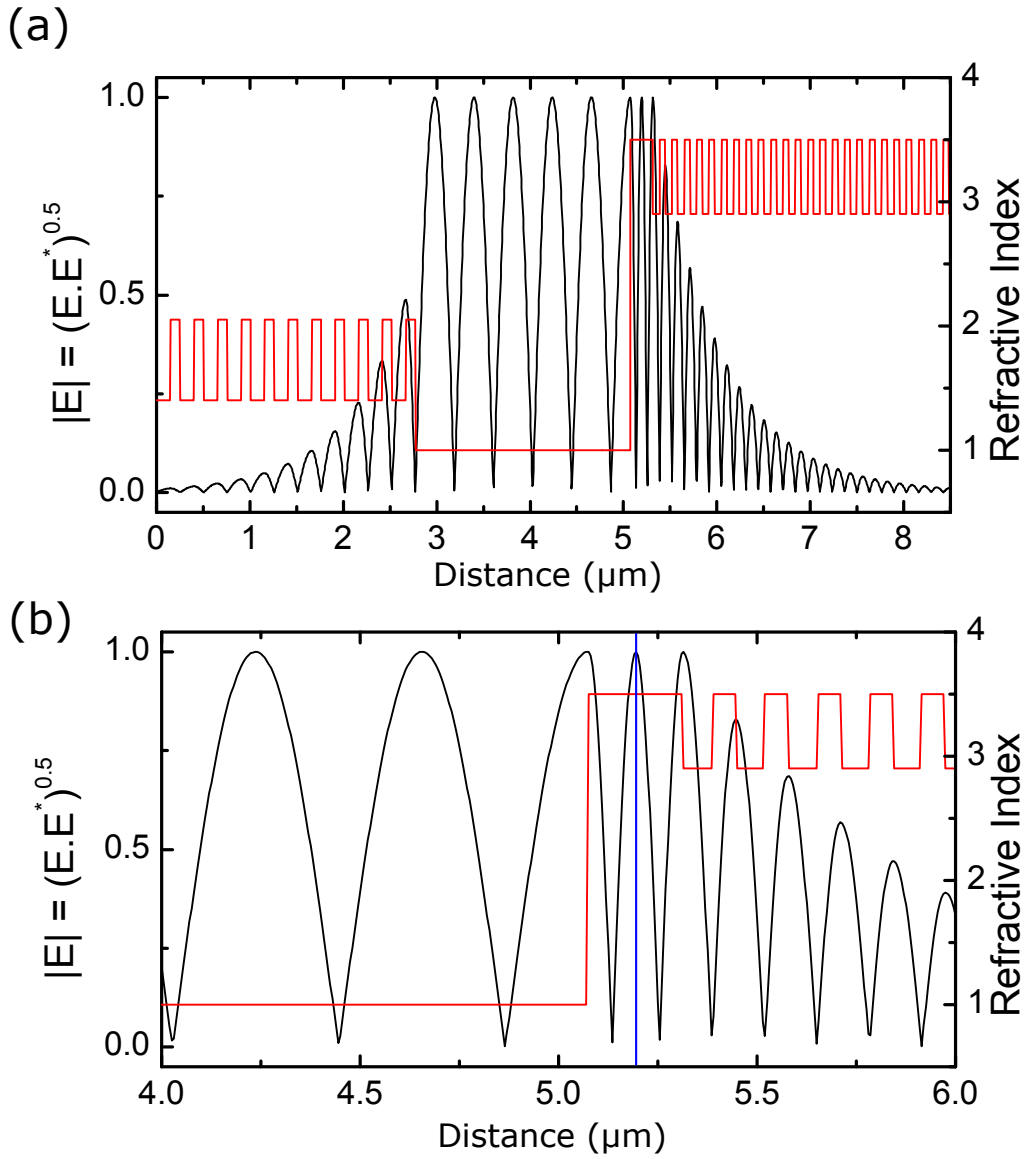

Figure 5.3: (a) E-field profile in the open cavity consisting of a 11 paired SiO_2/TiO_2 top mirror and a bottom 31 paired $Al_{0.85}GaAs/GaAs$ DBR. (b) Close up of GaAs cavity region containing a single InGaAs QW (blue line) at an E-field antinode.

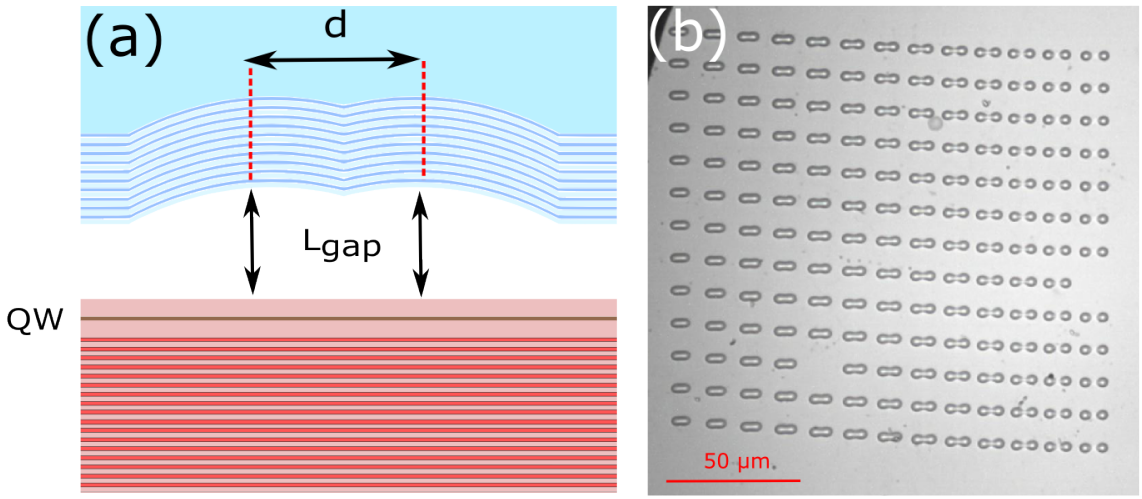

Figure 5.4: (a) Schematic cross-section of the coupled cavity. (b) Microscope image of the coupled cavity sample. The centre-to-centre distance incrementally decreases from 10 µm to 7 µm. The diameter and RoC of the individual concave mirrors are 4.8 µm and 6 µm.

In-situ characterisation of the QW was performed by moving the top DBR sample out of the optical path using the nanopositioners. At low excitation power of 10 µW the inhomogeneously broadened exciton linewidth is 650 µeV. The fabricated coupled cavity shape is determined by reducing the centre-to-centre distance between two adjacent concave depressions with textures defined by the isophase surface of a Gaussian mode profile. The individual hemispherical cavities confine the photonic field giving rise to 0-dimensional Gaussian modes. These couple as the distance between cavities them is reduced, leading to modal overlap and the formation of new symmetric and antisymmetric eigenmodes. The radius of curvature (RoC) of the single cavity concave feature was chosen to be 6 µm and the targeted physical cavity length to be 3 µm, with an expected Gaussian beam waist at the QW position of around 0.89 µm. The top sample consists of a 13x13 array of concave pairs with an incrementally decreasing centre-to-centre distance from 10 µm to 7 µm, transitioning from uncoupled to coupled cavities. An optical microscope image of the array is shown in Fig. 5.4 (b). Fig. 5.4 (a) shows a schematic of the formed coupled cavity. The concave mirrors are fabricated through FIB milling into a silica substrate before being

coated with 11 pairs of SiO_2/TiO_2 quarter wavestacks [41]. In contrast to concave mirrors fabricated using CO_2 laser ablation, FIB milling allows full morphological control of the milled sample and is inherently scalable to produce more complex photonic structures such as the coupled cavities discussed in this work. The fabrication of the concave features was carried out by Dr. A. Trichet at the Photonic Nanomaterials group at the University of Oxford.

5.3.1 Polaritonic Molecule Hamiltonian

For coupled polaritonic cavities the Hamiltonian describing the exciton-photon coupling Ω and the cavity-cavity coupling strength J can be written as

$$H = \begin{pmatrix} E_X & \Omega/2 & 0 & 0 \\ \Omega/2 & E_c & J/2 & 0 \\ 0 & J/2 & E_c & \Omega/2 \\ 0 & 0 & \Omega/2 & E_X \end{pmatrix} \tag{5.1}$$

where E_X and E_c are the exciton and bare cavity energies. The eigenenergies of the Hamiltonian are given by

$$E_{UP/LP} = \frac{(E_X + E_c \mp J/2)}{2} \pm \frac{1}{2}\sqrt{(\Delta \mp J/2)^2 + \Omega^2} \tag{5.2}$$

where Δ is the cavity-exciton detuning in each cavity. The red splitting is due to coupling between the photonic modes and the blue due to the exciton-photon coupling. Equation 5.2 is plotted in Fig. 5.5 (a) with $\Omega = 4$ meV and $J = 2$ meV and E_X set to zero. The cavity-cavity coupling strongly varies as a function of detuning due to the varying exciton/photon fraction as shown in Fig. 5.5 (b) which provides a degree of freedom in which to control the coupling strength in-situ.

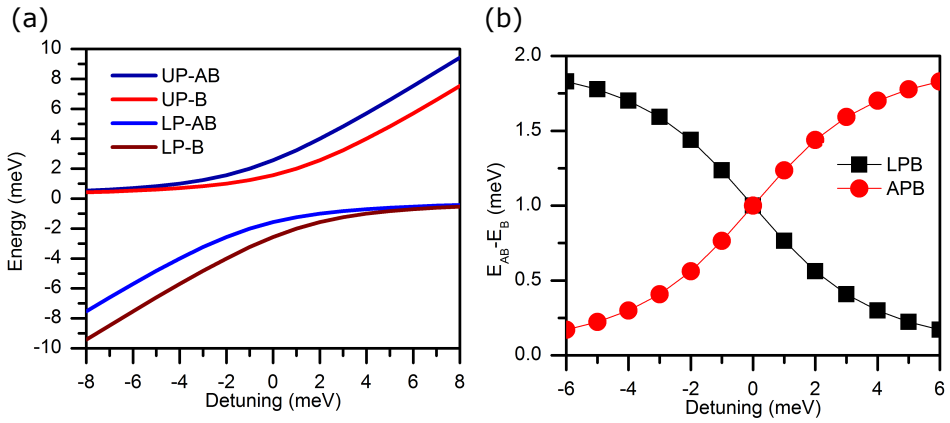

Figure 5.5: Eigenenergies of the coupled upper and lower polariton modes as described in Eqn. 1.16 plotted against exciton-photon detuning $\Delta = E_x - E_{ph}$ setting $\Omega = 4$ meV and $J = 2$ meV. (b) AB-B splitting as a function of detuning

5.4 Strong Coupling

Fig. 5.6 shows the anti-crossing between the coupled cavity eigenmodes when tuned through resonance with the QW exciton by applying a voltage to the bottom z-nanopositioner, reducing the mirror separation. Excitation is at 630 nm, close to a minima of the top dielectric DBR stopband. The spectra are measured using a 0.75m spectrometer with a resolution of 50 μeV. As discussed previously [134], the Rabi splitting is maximised when the cavity mirror separation is minimised. Here the mirror separation is ≈ 1 μm and at zero exciton-photon detuning the Rabi splitting is 3.3 meV. In this case, for a coupled cavity with a centre-to-centre distance of 7.7 μm, the tunnelling strength decreases as a function of exciton-photon detuning from 1 meV in the photonic case, to 0 meV at very positive detuning, consistent with Eqn 1.16. The bonding - anti-bonding energy separation is plotted in Fig. 5.7 (a) as a function of detuning. An approximately linear decrease in the cavity-cavity coupling strength is observed as a function of detuning decreasing from 800 μeV to zero spitting at a positive detuning of 3 meV. This is consistent with Eqn. 5.2 where the detuning, which determines the exciton/photon fraction of the polariton, changes the cavity-cavity coupling strength and is approximately linear close to resonance as shown in Fig.5.5 (b). Since the detuning can be arbitrarily chosen in-situ in the open cavity system,

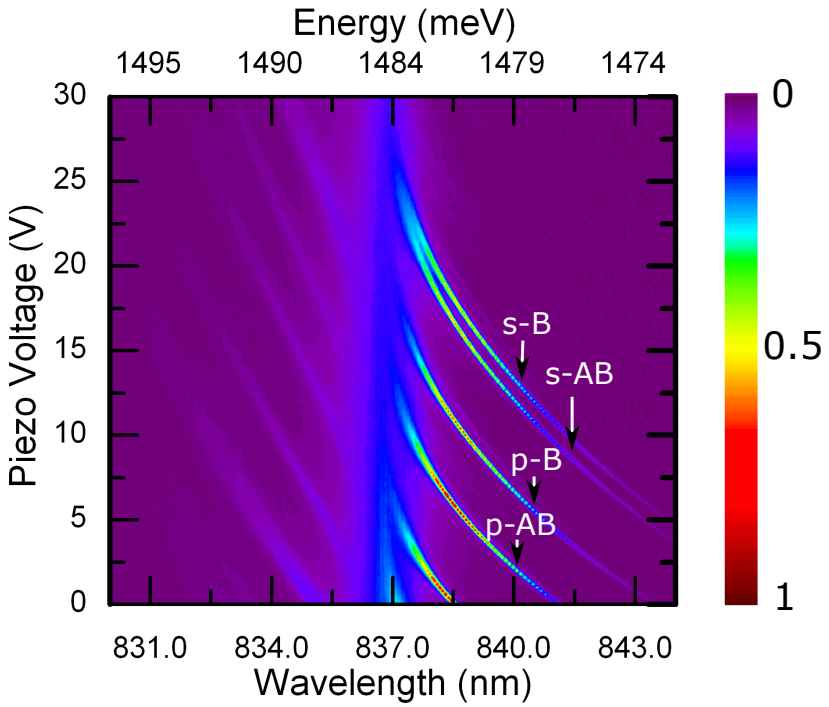

Figure 5.6: Avoided crossing when the cavity resonances are tuned through resonance with the QW exciton. A linear polariser was used to collect only the eigenmodes corresponding to the modes linearly polarised along the long axis of the photonic molecule. The mirror separation is around 1 µm and the Rabi splitting at zero detuning is 3.3 meV. The states labelled p-B and p-AB correspond to the bonding and anti-bonding modes that arise from the coupling of the first transverse modes in the constituent cavities.

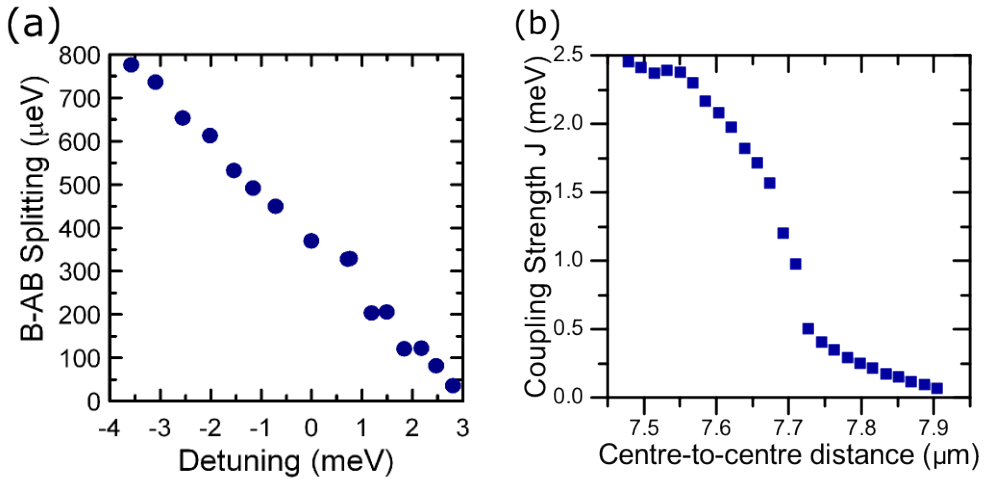

Figure 5.7: (a) B-AB splitting as a function of detuning extracted from Fig. 5.6. (b) The tunnelling strength J of the longitudinal mode as a function of centre-to-centre distance of the coupled cavities at a detuning of ≈ -10 meV. In each case the angle between top and bottom mirrors is adjusted so that the two cavities are in resonance. The splitting varies from 50 μeV for cavities with a centre-to-centre distance of 8 μm to a splitting of 2.5 meV for cavities with a centre-to-centre distance of 7.4 μm.

this provides a basic method of tuning of the cavity coupling strength by increasing or decreasing the excitonic fraction of the polariton.

5.5 Photonic Cavity Coupling

The coupling strength of the coupled longitudinal modes is plotted against centre-to-centre distance in Fig. 5.7 (b). Due to the very small lateral beam waist of the longitudinal modes of the uncoupled cavities, the transition between uncoupled and coupled cavities occurs abruptly when the centre-to-centre distance is smaller than 8 μm. Here the splitting between the bonding and anti-bonding modes, when tuned into resonance using the angle between the top and bottom mirrors, is at a minimum value of 50 μeV. As we decrease the centre-to-centre distance, we see a rapid increase in the coupling strength reaching a maximum value of 2.5 meV when the centre-to-centre distance is 7.4 μm. This non-linear increase at intermediate separations is attributed to the Gaussian beam profile of

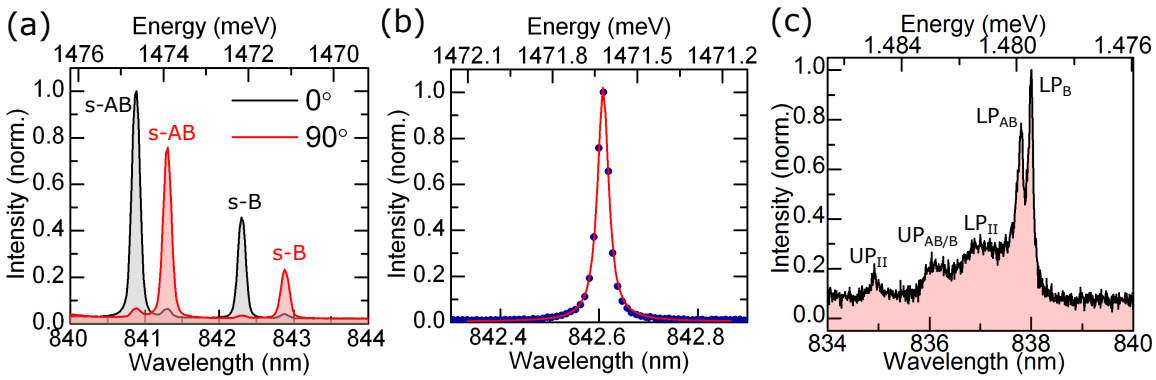

Figure 5.8: (a) Typical spectra of the coupled cavity emission under non resonant excitation and a large negative exciton-photon detuning. The asymmetric structure leads to a large linear polarisation splitting in the coupled bonding and anti-bonding eigenmodes. (b) Exemplary bonding eigenmode at large negative exciton-photon detuning of -10 meV. The lorentzian fit to the mode yields a linewidth of 26.75±0.03 pm (60 μeV) corresponding to a photonic Q-factor of 31,500. (c) Spectrum at zero exciton-photon detuning. A fit to the lower bonding polariton yields a very narrow polariton linewidth of 150 μeV.

the bare cavity mode which leads to a rapid increase in coupling as the degree of wavefunction overlap increases through the Gaussian profile of the electric-field on the concave DBR.

5.6 Coupled Cavity Photoluminescence

A typical spectrum of a coupled cavity is shown in Fig. 5.8 (a). Two sets of bonding and anti-bonding modes are present due to a polarisation splitting in the cavity due to the elliptical shape. The black and red spectra correspond to the linearly polarised photoluminescence for the orthogonal polarisations of 0° and 90°. We now turn our attention to the linewidths that can be achieved in the current system. Fig. 5.8 (b) shows the bonding state at large negative detuning of −5 meV with a mirror separation of around 1 μm. A Lorentzian fit yields a FWHM of 60 μeV corresponding to a photonic Q-factor of around 31,500. This is most likely limited by the stability of the system due to low frequency acoustic vibrations [40], as discussed in Section 3.6 and by leakage of the cavity mode

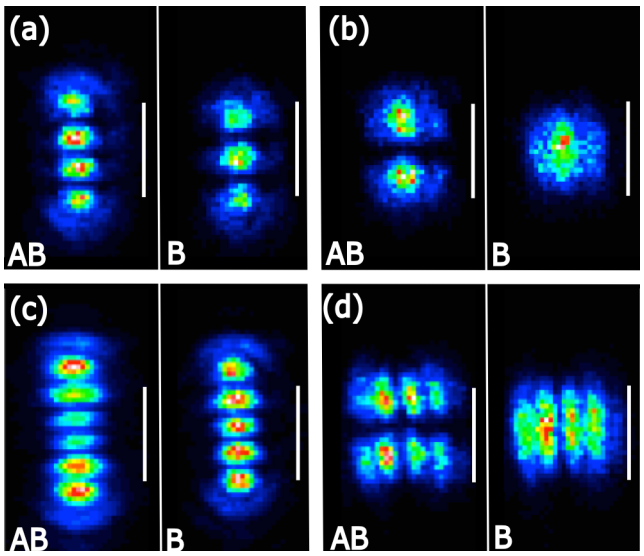

Figure 5.9: Tomographic images of the lowest 8 energy modes of the photonic molecule with centre-to-centre distance of 7.46 μm. (a) s-bonding (RHS) and s-anti-bonding (LHS) modes due to the coupling between the ground state longitudinal modes. (b) p-bonding (RHS) and p-anti-bonding (LHS) modes due to the coupling of the first transverse modes. (c) due to the coupling of the second transverse modes. (d) due to the coupling between the fourth transverse modes. Scale bar is 2 μm.

through the interface between concave and planar regions on the top DBR [82]. Fig. 5.8 (c) shows the lower polariton bonding and anti-bonding states at zero exciton-photon detuning. Fitting the bonding LP state reveals very narrow polariton linewidths of 150 μeV. Significant improvement of this value is expected for a semiconductor half cavity containing a QW with less inhomogeneous broadening.

5.7 Mode Profiles

The hemispherical cavities support transverse modes as discussed in Section 3.5.2. The spatial extent of these modes is larger, leading to increased cavity-cavity coupling. Fig. 5.9 shows tomographic images of the pairs of bonding and anti-bonding of the lowest energy eigenmodes when the coupled cavities are tuned into resonance. In Fig. 5.9 (a) the coupled longitudinal modes are visible corresponding to the ground state bonding and anti-bonding

modes as discussed in the previous section. Fig. 5.9 (b) shows the bonding/anti-bonding modes due to the coupling between the first transverse mode corresponding to LG_{01}. Higher order bonding/anti-bonding modes are shown in Fig. 5.9 (c) and (d). Fig. 5.9 (c) shows spatial lobes in the horizontal direction corresponding to the coupling between py-type modes.

5.8 Angular Tunability

The reproducibility in the fabrication of adjacent cavities is within around 1 nm in the depth of the concave depressions. This is significantly large to shift the modal wavelength by a few meV, shifting the two cavities out of resonance when the mirrors are perfectly parallel. The ability to tune the relative angle between the two mirrors introduces another degree of freedom in which to tune the cavity mode as a small angle between the two mirrors causes a shift in the resonance energy of adjacent hemispherical cavities. The tunnelling strength J' can then be further controlled through the cavity-cavity detuning $\delta = E_{c1} - E_{c2}$ where

$$J' = \sqrt{\delta^2 + J^2} \tag{5.3}$$

Fig. 5.10 (a) shows the energy of the ground state bonding and anti-bonding modes as a function of angle of the goniometer nanopositioner where 0° is defined as the angle which puts the two adjacent cavities in perfect resonance i.e. $E_{c1} = E_{c2}$. This angle introduces a relative gradient in energy across the two samples as the mirror separation is varied, in the same fashion as the incorporation of a wedged cavity region in monolithic cavities. Therefore the inherent detuning between the adjacent cavities due to fabrication procedure can be compensated for. This allows the two adjacent cavities to be put into exact resonance to form a photonic molecule. Fig. 5.10 (b)(c)(d) show tomographic images of the ground state bonding and anti-bonding states corresponding to various angular detunings from Fig. 5.10 (a). The spatial intensity distribution of the modes reflects

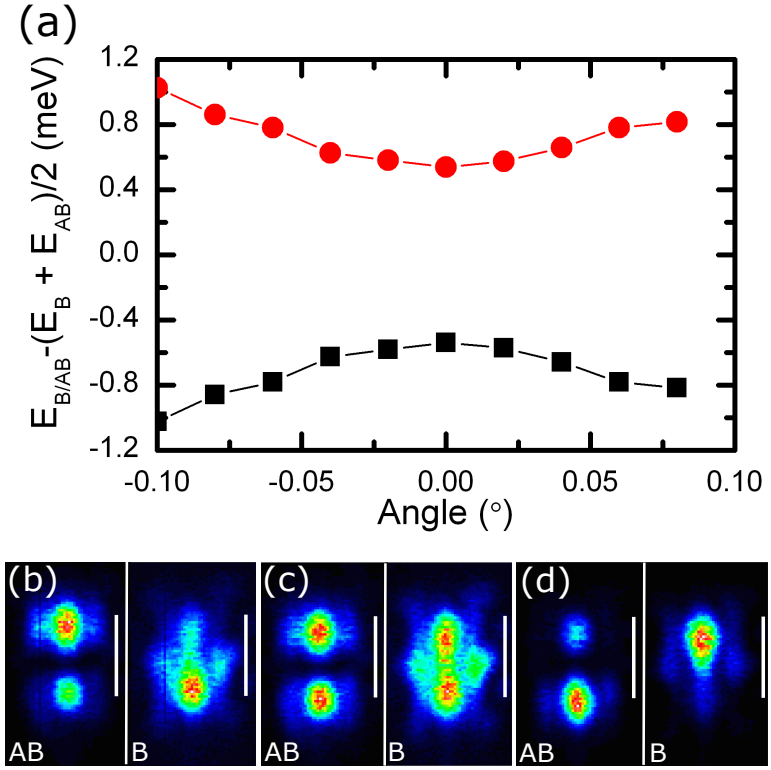

Figure 5.10: (a) Anticrossing between the low energy bonded mode (black) and the higher energy antibonded mode (red) as a function of goniometer nanopositioner angle. Angle = 0° is defined when the bare cavity energies are in resonance. The scale bar is 2 μm. (b) Tomographic images of bonded (RHS) and anti-bonded (LHS) modes at an angle of −0.1°. (c) At resonance. (d)At an angle of +0.08°.

the degree of detuning between the adjacent cavities. A transition was observed from a decoupled state at negative angles where the maximum intensity of the s-B and s-AB lies in the separate cavities, to a fully equal intensity distribution in bonding and anti-bonding states at resonance and back to an asymmetric intensity distribution as we tune through resonance to positive angles. This provides a unique ability to perform in-situ tuning of the cavity coupling strength.

5.9 Summary

In summary coupled polaritonic cavities with strong lateral confinement were presented. Full tunability of the cavity coupling strength was carried out through controlled fabrication of the centre-to-centre distance, angular tuning of the relative parallelism between the top and bottom mirrors and controlling the exciton-photon detuning. We speculate a number of applications where this tunability is of practical use; such as the coupling of both the exciton and biexciton line of a single QD to the optical modes of the photonic molecule in an efficient manner, leading to an ultra bright source of entangled photon pairs [135]. This is advantageous in comparison to other systems such as coupled micropillars, since this tunability is combined with very high photonic Q-factors and submicron lateral confinement which cannot be achieved in micropillar systems due to surface recombination effects when the diameter is reduced. In polaritonics, there are a number of possible applications of the coupled tunable cavity system. These include polariton AC Josephson oscillations [129] and the potential to observe the polariton blockade effect in coupled polariton boxes [5]. Finally, the strong lateral confinement combined with the inherent scalability in fabrication has the potential to realise photon fermionisation [9] and the polariton Mott insulator transition in 1-dimensional and 2-dimensional coupled cavity arrays.

Chapter 6

Conclusions and Outlook

6.1 Summary

The main goal of this thesis was to develop and demonstrate a fully tunable microcavity with strong lateral photonic confinement. By separating the two mirrors, independent fabrication of the mirrors was performed. This allowed the fabrication by FIB milling of a concave feature before coating with dielectric quarter wavestacks. The bottom semiconductor DBR was fabricated by conventional molecular beam epitaxy and contained a cavity region grown on top of the DBR. This cavity region contained one or more QWs at the electric field antinodes of the formed microcavity. Crucially, the concave-planar cavity introduces lateral photonic confinement, since the wavefronts must match the concave mirror radius of curvature. The beam waist is at its minimum when intersecting the QWs leading to submicron 3-dimensional polariton confinement. As seen in Chapter 3, this allowed unprecedented lateral confinement on submicron scales with very high photonic Q-factors of 31,000 at micron size mirror separations (Chapter 5). In contrast to alternative fabrication methods such as laser ablation, the use of FIB milling allows much smaller dimensions of the concave mirrors where the confinement is significantly increased. In this thesis, radii of curvature from 20 μm to 5.6 μm were demonstrated, where the latter is the

limit imposed by the stable resonator condition due to the large penetration into the semiconductor DBR. In Chapter 4 strong evidence of polariton condensation was presented using a bottom DBR containing 12 GaAs QWs. The large transverse mode spacing, due to the strong lateral confinement, combined with the ability to perform in-situ tuning of the cavity resonances, allowed the observation of condensation in transverse modes which carry orbital angular momentum. The coherence of the condensate allowed the underlying spin-orbit coupling of the mode to be revealed where complex spin and phase textures are imprinted into the polariton system from their photonic component. Tomographic imaging of the modes revealed the formation of radial and azimuthal spin vortices and hyper-spin anti-vortices. The light-matter nature of the condensate was shown to significantly effect the spin texture and cause a transition to linearly polarised eigenmodes for more excitonic condensates. Nonlinear emission was also demonstrated in planar-planar cavities where angular resolved PL revealed threshold behaviour consistent with polariton condensation. In the final experimental chapter, coupled cavities were formed through FIB milling of concave features with varying centre-to-centre distances. Full control of the coupling strength was performed through control of the centre-to-centre distance between coupled cavities. Furthermore, in-situ tuning of the cavity coupling strength was demonstrated through control of the exciton-photon detuning via the mirror separation and the cavity-cavity detuning through the ability to introduce a relative angle between the top and bottom mirrors.

6.2 Future Directions

The work presented in this thesis paves the way for future studies of strongly confined polaritons in tunable optical cavities. The following sections present the future research directions which build upon the experiments performed in the previous chapters.

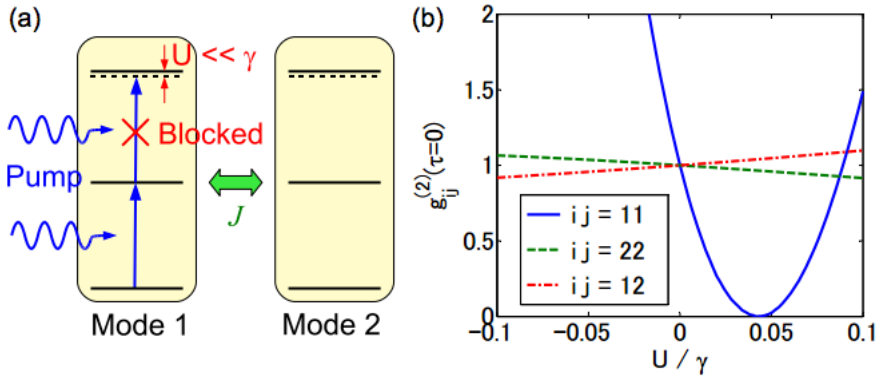

Figure 6.1: Figure taken from [5]. (a) Schematic of coupled cavities with coupling strength J. (b) $g^2(t=0)$ plotted as a function of nonlinearity.

6.2.1 Polariton Blockade

As discussed in Section 1.6, polariton blockade remains a theoretical proposal where the presence of a single polariton in a cavity prevents the resonant injection of a second polariton due to the polariton-polariton interaction [76]. This leads to single photon emission at GHz rates due to the short polariton lifetime, which is significantly faster than competing systems such as micropillar QDs where the lifetime is around 1ns. The main experimental requirement to observe blockade is that the lower polariton linewidth be smaller than the single polariton-polariton interaction induced blueshift. This blueshift is estimated to be around 9 μeV.μm^2 in micropillars [32]. In comparison, the lowest recorded polariton linewidths at zero exciton-photon detuning are around 80 μeV, which are significantly larger than the interaction. As previously discussed in Section 1.3.4, one way to increase the polariton interaction strength is to increase the overlap of the exciton wavefunction by decreasing the lateral size of the cavity through the fabrication of micropillars, mesa or photonic crystals. However, the polariton linewidth becomes significantly degraded due to issues with surface recombination, scattering and quenching of the QW exciton when the lateral size is reduced to around 1 μm. This is the main technological obstacle preventing the observation of blockade.

As presented in this thesis, the use of a hemispherical cavity allows unprecedented lateral photonic confinement of the polariton without any degradation of the polariton linewidth. In this case the main factor limiting the polariton linewidth is the inhomogeneously broadened QW linewidth, and the photonic Q-factor which is limited by the stability of the tunable cavity. Furthermore, the stringent linewidth criteria is significantly reduced when utilising a subtle quantum interference effect in coupled polariton boxes.[5] In this case almost perfect antibunching is expected when the nonlinear interaction, $U = 0.0428\gamma$, where γ is the lower polariton linewidth. This reduction in the required linewidth comes at the price of oscillations in the $g^{(2)}$ function with a period determined by the cavity coupling rate J. Experimentally, a streak camera is required to resolve the photon antibunching in the $g^{(2)}$ function and coupled cavities with coupling times exceeding 2 ps are required. In this thesis, the system of photonic molecules demonstrated in Chapter 5 fulfil all of the requirements in order to observe unconventional polariton blockade in coupled cavities such as; enhanced polariton-polariton interaction due to submicron lateral confinement; tunable cavity coupling times controlled through cavity centre-to-centre distance and angular tunability; and narrow polariton linewidths at zero detuning currently of 150 μeV. Recently, Xu et al. [130] extended the theoretical discussion of photon antibunching in coupled cavities to photonic molecules, where photon antibunching can be expected in both the bonding and antibonding eigenmodes under resonant excitation due to a similar quantum inteference effect as presented in [5]. Further reduction of the polariton linewidth is expected for QW samples with reduced inhomogeneous broadening. Photon autocorrelation measurements under resonant excitation are currently planned.

6.2.2 Surface Acoustic Waves

The fabrication of interdigital transducers (IDTs) on the surface of monolithic microcavities allow the modulation of both the exciton and cavity energies through the formation of propagating surface acoustic waves (SAWs). Confinement can be introduced in a sin-

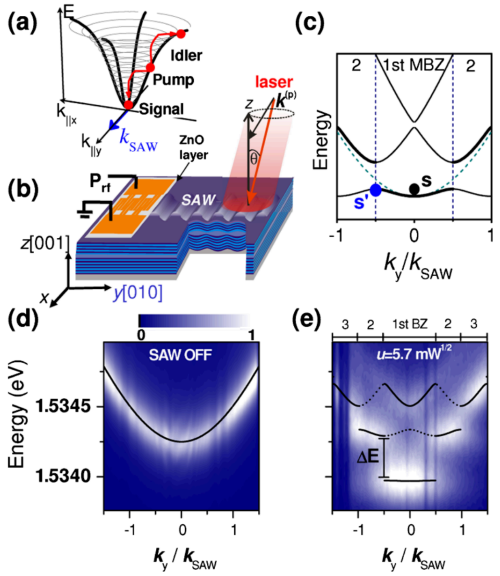

Figure 6.2: Figure taken from [25]. (a) Schematic of optical parametric oscillator (b) Sample schematic with SAWs propagating along the y[010] direction. (c) Folding of the LPB dispersion due to SAW. (d)(e) LPB dispersion under weak optical excitation without and with the presence of a SAW.

gle direction using a single propagating non piezo-electric SAW [136] as shown in Fig 6.2 or in 2-dimensions through the use of cross-propagating SAWs.[137] To date, the SAW wavelength is limited to around 8 μm due to the poor penetration through the top DBR at higher frequencies. In the open cavity, the mirrors are grown separately, allowing the IDTs to be directly fabricated onto the cavity region on the bottom semiconductor DBR. This will allow significantly larger frequencies of > 2 GHz to be applied. By using cross-propagating SAWs a 2-dimensional confinement lattice can be formed where the polariton-polariton interaction is greatly increased. If the nonlinear interaction, U becomes greater than the tunnelling between potential minima, J, a transition from a superfluid to the polaritonic Mott insulator state may be achievable where each potential minima has single polariton occupancy. Such transitions are described by the Bose-Hubbard model and have been reported in atomic physics using optical lattices.[10]

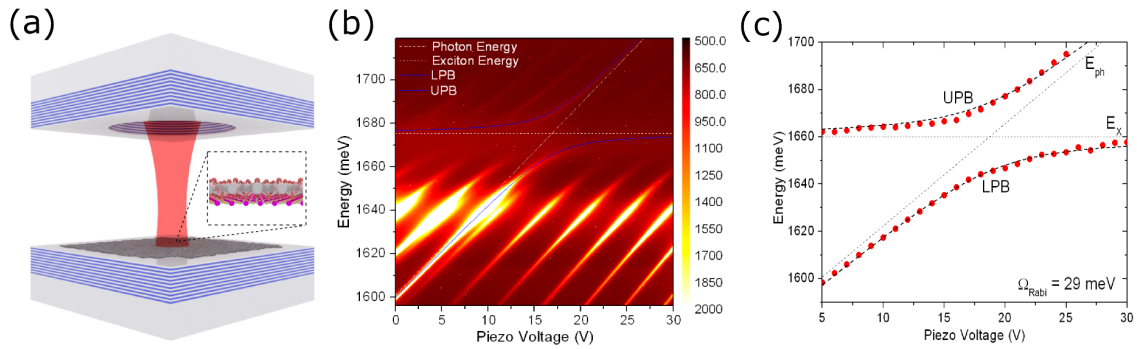

Figure 6.3: (a) Schematic of the tunable cavity. Inset: $MoSe_2$ monolayer on hBN film. (b) PL as a function of piezo voltage for the single monolayer. The Rabi splitting of the longitudinal mode is 20 meV. (c) Double QW heterostructure longitudinal mode peak energy as a function of piezo voltage. The Rabi splitting is 29 meV.

6.2.3 Monolayer Heterostuctures

Monolayer films of transition metal dichalcogenides (TMDCs) are direct band gap semiconductors where excitons with large binding energies (300 meV) and small Bohr radius (1 nm) give the materials an enormous oscillator strength. Such thin films have great potential for development of novel flexible optoelectronic devices. In studies not included in this thesis we report strong exciton-photon coupling with these materials using a tunable microcavity. TMDCs can be embedded into the cavity via standard transfer methods of mechanically exfoliated monolayer sheets on to the bottom planar DBR. A single monolayer of molybdenum diselenide ($MoSe_2$) was placed on a 3 monolayer thick sheet of hexagonal boron nitride (hBN) at an electric field antinode at the planar DBR surface (Fig 6.3) and a double quantum well (QW) heterostructure was produced by placing a second monolayer of $MoSe_2$, separated by 3nm thick hBN, on top of the first monolayer sheet. A characteristic anticrossing between the tunable cavity mode resonances with the neutral exciton energy for both the single and double QWs at 4K was observed. For a single monolayer a vacuum Rabi splitting of 20 meV was recorded, which is increased to around 29 meV for the double QW heterostructure displaying the expected $\Omega_{rabi} \propto \sqrt{N_{QW}}$ dependence, as shown in Fig 6.3 (b) and Fig 6.3 (c). This work opens a new avenue in the field of

polaritonics in a new material system of van der Waal crystals.

6.3 Final Remarks

The work included in this thesis has set the ground work in tunable microcavity systems with strong polariton confinement. This paves the way for future studies of strongly interacting polaritonic systems where there is further exciting work to be done.

Chapter 7

Appendices

7.1 Appendix A: Theoretical Model of Spin Vortices

Here the theoretical calculations performed to interpret the experimental data presented in Chapter 4 are presented. Degenerate perturbation theory is used to find the eigenmodes of the polariton system in the case of low polariton densities, where nonlinearities play a negligible role, in the presence of SO coupling, elliptical shape of the top concave mirror and birefringence from the anisotropy of the refractive index of the top mirror. Taking the eigenvectors $\begin{pmatrix}1\\0\end{pmatrix}$ and $\begin{pmatrix}0\\1\end{pmatrix}$ to represent σ^+/σ^- circularly polarised polaritons, the 2x2 Hamiltonian describing the LPB in the linear regime can be written as:

$$H = \begin{pmatrix} -\frac{\hbar^2\nabla^2}{2m_{LP}} + V & \beta\left(\frac{\partial}{\partial x} - i\frac{\partial}{\partial y}\right)^2 + \Omega e^{i\theta}/2 \\ \beta\left(\frac{\partial}{\partial x} + i\frac{\partial}{\partial y}\right)^2 + \Omega e^{-i\theta}/2 & -\frac{\hbar^2\nabla^2}{2m_{LP}} + V \end{pmatrix}, \tag{7.1}$$

where m_{LP} is the lower-polariton effective mass. The terms depending on $\beta = \hbar^2(1/m_{TE} - 1/m_{TM})/4$ [138], where $m_{TE/TM}$ are the lower-polariton masses in the TE/TM polarizations, describe the TE-TM splitting. As pointed out in [134] the top concave mirror induces a strong near-harmonic lateral confinement potential. $V = \frac{1}{2}m_{LP}\omega_{HO}^2[x^2(1+\delta)+y^2(1-\delta)]$,

where ω_{HO} is the strength of the harmonic confinement. The terms $\pm a = \pm\frac{1}{2}m_{LP}\omega_{HO}^2\delta$ account for an elliptical asymmetry of the top circular mirror with the long axis either aligned along the x or y directions. As birefringence may arise in both the top and bottom mirrors due to strain, the terms $\Omega e^{\pm i\theta}/2$ account for a birefringence that induces a shift at $k = 0$ between the TE-TM branches and tends to align the field polarization along the direction θ.

Due to the strong harmonic confinement the theoretical approach treats the SO coupling, birefringence and the asymmetry as perturbations. To study a 2-dimensional harmonic oscillator several equivalent eigenvector bases can be used: Laguerre-Gauss modes $LG_{pl}^{\sigma^\pm}$ (where p and l are radial and azimuthal quantum numbers) and Hermite-Gauss modes $HG_{sr}^{\sigma^\pm}$ (where r and s are quantum numbers along the x and y axes). While the basis of LG modes allows a more intuitive understanding of the shape of the spin vortices, the basis of the HG modes allows an easier evaluation of the matrix elements needed to determine the perturbed eigenenergies and eigenmodes. For this reason, and since the perturbed eigenmodes and eigenenergies do not depend on the basis of the Hilbert space used to evaluate them, we use the basis of the HG modes to apply perturbation theory. In the case of the first transverse mode the four relevant HG modes are:

$$\psi_1(x,y) = \frac{xe^{-\frac{x^2+y^2}{2\sigma^2}}}{\sqrt{\sigma^4\pi/2}}\begin{pmatrix}1\\0\end{pmatrix} \qquad \psi_2(x,y) = \frac{xe^{-\frac{x^2+y^2}{2\sigma^2}}}{\sqrt{\sigma^4\pi/2}}\begin{pmatrix}0\\1\end{pmatrix}$$
$$\psi_3(x,y) = \frac{ye^{-\frac{x^2+y^2}{2\sigma^2}}}{\sqrt{\sigma^4\pi/2}}\begin{pmatrix}1\\0\end{pmatrix} \qquad \psi_4(x,y) = \frac{ye^{-\frac{x^2+y^2}{2\sigma^2}}}{\sqrt{\sigma^4\pi/2}}\begin{pmatrix}0\\1\end{pmatrix}.$$

Using these modes as basis, the new perturbed eigenenergies and eigenmodes of the system are obtained by diagonalising the following matrix:

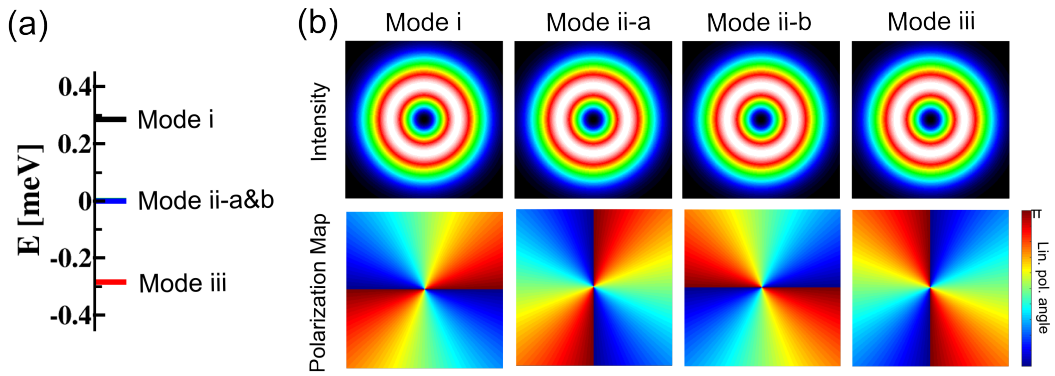

Figure 7.1: Case for no mirror ellipticity and birefringence equal to zero. (a) Simulated energy levels: mode i (black), mode iia (blue), mode iib (green), and mode iii (red), the energy is evaluated with respect to the unperturbed mode. (b) Simulated polariton density (first row) and angle of linear polarization $arctan(S_2/S_1)$ (second row). To obtain both the spectra and the eigenmodes the following parameters are used: $\beta = 0.06\ meV \cdot \mu m^2$, $\sigma = 0.65\ \mu m$. All graphs are $3\mu m \times 3\mu m$ in size.

$$M = \begin{pmatrix} a\sigma^2 & -\frac{\beta}{\sigma^2} + \frac{1}{2}e^{i\theta}\Omega & 0 & \frac{i\beta}{\sigma^2} \\ -\frac{\beta}{\sigma^2} + \frac{1}{2}e^{-i\theta}\Omega & a\sigma^2 & -\frac{i\beta}{\sigma^2} & 0 \\ 0 & \frac{i\beta}{\sigma^2} & -a\sigma^2 & \frac{\beta}{\sigma^2} + \frac{1}{2}e^{i\theta}\Omega \\ -\frac{i\beta}{\sigma^2} & 0 & \frac{\beta}{\sigma^2} + \frac{1}{2}e^{-i\theta}\Omega & -a\sigma^2 \end{pmatrix} \tag{7.2}$$

where $\sigma = \sqrt{\hbar/m_{LP}\omega_{HO}}$. For the case of zero birefringence and no asymmetry in the harmonic confinement, the energy spectra, the polariton density and the polarization angle for the four eigenmodes are plotted in figure 7.1. As expected, the higher (black) and the lower (red) eigenmodes are azimuthal and radial spin vortices. The two remaining central modes (green and blue) are spin anti-vortices in agreement with the experimental observations in Fig 4.8 in Chapter 4.

The case of non-zero asymmetry and birefringence is plotted in Fig. 7.2. These additional terms lift the degeneracy among the two central spin anti-vortex modes, thus breaking the symmetry of the spectra and inducing polaritons to polarise along a preferred direction. This is consistent with experimental observations, although in the experiments the shape of the high-energy mode is generally less deformed by the asymmetry and birefringence

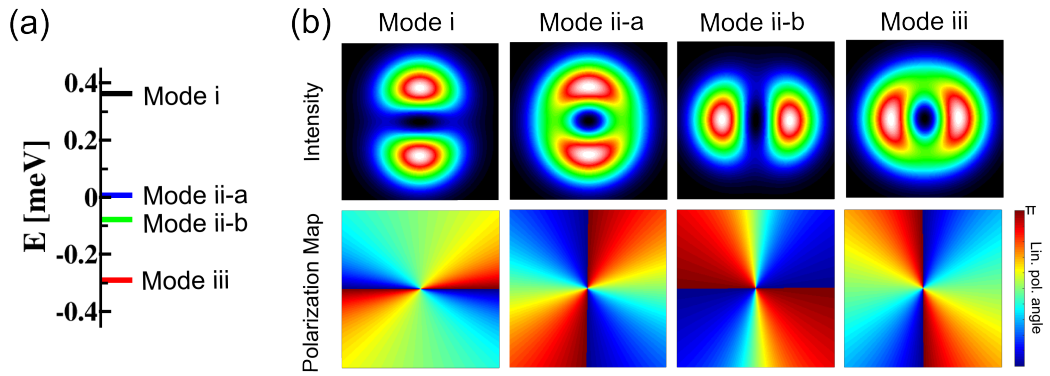

Figure 7.2: Case with mirror ellipticity and birefringence different from zero. (a) Simulated energy levels: mode i (black), mode iia (blue), mode iib (green), and mode iii (red), the energy is evaluated with respect to the unperturbed mode. (b) Simulated polariton density (first row) and angle of linear polarization $arctan(S_2/S_1)$ (second row). The following parameters are used: $\beta = 0.06\ meV \cdot \mu m^2$, $\sigma = 0.65\ \mu m$, $\Omega = 0.125\ meV$, $\theta = 0.01\pi$, and $a = -0.25\ meV$to obtain both the spectra and the eigenmodes. All graphs are $3\mu m \times 3\mu m$ in size.

than the low-energy modes. A possible explanation for this is that our theoretical model is based on the approximation of quadratic dispersion while in the polariton system the dispersion is strongly dependent on k. Since the modes are strongly confined, high k vectors are likely to play an important role. In addition exciton-exciton interactions and pump-decay mechanisms, both of which are not included in the model, may also lead to experimental/theory differences in the details of the patterns.

Bibliography

[1] M. Bayer, T. Gutbrod, J. P. Reithmaier, A. Forchel, T. L. Reinecke, P. A. Knipp, A. A. Dremin, and V. D. Kulakovskii, "Optical modes in photonic molecules," *Phys. Rev. Lett.*, vol. 81, pp. 2582–2585, 1998.

[2] M. Galbiati, L. Ferrier, D. Solnyshkov, D. Tanese, E. Wertz, A. Amo, M. Abbarchi, P. Senellart, I. Sagnes, A. Lemaitre, E. Galopin, G. Malpuech, and J. Bloch, "Polariton condensation in photonic molecules," *Phys. Rev. Lett.*, vol. 108, p. 126403, 2012.

[3] T. Jacqmin, I. Carusotto, I. Sagnes, M. Abbarchi, D. D. Solnyshkov, G. Malpuech, E. Galopin, A. Lemaitre, J. Bloch, and A. Amo, "Direct observation of dirac cones and a flatband in a honeycomb lattice for polaritons," *Phys. Rev. Lett.*, vol. 112, p. 116402, 2014.

[4] K. A. Atlasov, K. F. Karlsson, A. Rudra, B. Dwir, and E. Kapon, "Wavelength and loss splitting in directly coupled photonic-crystal defect microcavities," *Opt. Express*, vol. 16, no. 20, pp. 16255–16264, 2008.

[5] M. Bamba, A. Imamoğlu, I. Carusotto, and C. Ciuti, "Origin of strong photon antibunching in weakly nonlinear photonic molecules," *Phys. Rev. A*, vol. 83, p. 021802, 2011.

[6] C. Weisbuch, M. Nishioka, A. Ishikawa, and Y. Arakawa, "Observation of the coupled exciton-photon mode splitting in a semiconductor quantum microcavity," *Physical Review Letters*, vol. 69, no. 3314, 1992.

[7] J. Kaspzak, M. Richard, S. Kundermann, A. Baas, P. Jeambrun, J. Keeling, F. Marchetti, M. Szymanska, R. Andre, and J. S. et al, "Bose-einstein condensation of exciton polaritons," *Nature*, vol. 443, no. 409, 2006.

[8] A. Amo, J. Lefrere, S. Pigeon, C. Abrados, C. Cuiti, I. Carusotto, R. Houdre, E. Giacobino, and A. Bramati, "Superfluidity of polaritons in semiconductor microcavities," *Nature Physics*, vol. 5, pp. 805–810, 2009.

[9] I. Carusotto, D. Gerace, H. E. Tureci, S. De Liberato, C. Ciuti, and A. Imamoğlu, "Fermionized photons in an array of driven dissipative nonlinear cavities," *Phys. Rev. Lett.*, vol. 103, p. 033601, 2009.

[10] M. Greiner, O. Mandel, T. Esslinger, T. W. Hansch, and I. Bloch, "Quantum phase transition from a superfluid to a mott insulator in a gas of ultracold atoms," *Nature*, vol. 415, no. 6867, pp. 39–44, 2002.

[11] J. Singh, *Electronic and Optoelectronic Properties of Semiconductor Structures*. Cambridge University Press, 2003. Cambridge Books Online.

[12] M. Born and E. Wolf, *Principles of Optics: Electromagnetic Theory of Propagation, Interference and Diffraction of Light*. Cambridge University Press, 7th ed., 1999.

[13] J. J. Hopfield, "Theory of the contribution of excitons to the complex dielectric constant of crystals," *Physical Review*, vol. 112, pp. 1555–1567, 1958.

[14] V. Savona, L. Andreani, P. Schwendimann, and A. Quattropani, "Quantum well excitons in semiconductor microcavities: Unified treatment of weak and strong coupling regimes," *Solid State Communications*, vol. 93, no. 9, pp. 733 – 739, 1995.

[15] A. Amo, D. Sanvitto, F. P. Laussy, D. Ballarini, E. del Valle, M. Martin, A. Lemaitre, J. Bloch, D. Krizhanovskii, and M. S. et al, "Collective fluid dynamics of polariton condensate in a semiconductor microcavity," *Nature*, vol. 457, no. 291, 2009.

[16] M. Sich, D. N. Krizhanovskii, M. S. Skolnick, A. V. Gorbach, R. Hartley, D. V. Skyrabin, E. A. Cerda-Mendez, K. Biermann, R. Hey, and P. V. Santos, "Observation of bright polariton solitons in a semiconductor microcavity," *Nature Photonics*, vol. 6, no. 50-55, 2012.

[17] F. Tassone, C. Piermarocchi, V. Savona, A. Quattropani, and P. Schwendimann, "Bottleneck effects in the relaxation and photoluminescence of microcavity polaritons," *Phys. Rev. B*, vol. 56, pp. 7554–7563, 1997.

[18] A. I. Tartakovskii, M. Emam-Ismail, R. M. Stevenson, M. S. Skolnick, V. N. Astratov, D. M. Whittaker, J. J. Baumberg, and J. S. Roberts, "Relaxation bottleneck and its suppression in semiconductor microcavities," *Phys. Rev. B*, vol. 62, pp. R2283–R2286, 2000.

[19] R. Houdre, J. Gibernon, P. Pellandini, R. Stanley, U. Oesterle, C. Weisbuch, J. O'Gorman, B. Roycroft, and M. Ilegems, "Saturation of the strong coupling regime in a semiconductor microcavity: Free-carrier bleaching of cavity polaritons," *Phys. Rev. B*, vol. 52, no. 7810, 1995.

[20] F. Jahnke, M. Kira, S. Koch, G. Khitrova, E. Lindmark, T.R.Nelson, D. Wick, J. Berger, O. Lyngnes, and e. a. H.M. Gibbs, "Excitonic nonlinearities of semiconductor microcavities in the nonperturbative regime," *Phys. Rev. Lett.*, vol. 77, no. 5257, 1996.

[21] D. Bajoni, P. Senellart, E. Wertz, I. Sagnes, A. Miard, A. Lemaitre, and J. Bloch, "Polariton laser using single micropillar gaas-gaalas semiconductor cavities," *Phys. Rev. Lett.*, vol. 100, p. 047401, 2008.

[22] R. M. Stevenson, V. N. Astratov, M. S. Skolnick, D. M. Whittaker, M. Emam-Ismail, A. I. Tartakovskii, P. G. Savvidis, J. J. Baumberg, and J. S. Roberts, "Continuous wave observation of massive polariton redistribution by stimulated scattering in semiconductor microcavities," *Phys. Rev. Lett.*, vol. 85, pp. 3680–3683, 2000.

[23] J. J. Baumberg, P. G. Savvidis, R. M. Stevenson, A. I. Tartakovskii, M. S. Skolnick, D. M. Whittaker, and J. S. Roberts, "Parametric oscillation in a vertical microcavity: A polariton condensate or micro-optical parametric oscillation," *Phys. Rev. B*, vol. 62, pp. R16247–R16250, 2000.

[24] J. Bloch, *Polariton Condensates in Low Dimensional Cavities*, vol. 177 of *Springer Series in Solid-State Sciences*. Springer, 2013.

[25] E. A. Cerda-Méndez, D. N. Krizhanovskii, M. Wouters, R. Bradley, K. Biermann, K. Guda, R. Hey, P. V. Santos, D. Sarkar, and M. S. Skolnick, "Polariton condensation in dynamic acoustic lattices," *Phys. Rev. Lett.*, vol. 105, no. 116402, 2010.

[26] E. A. Cerda-Méndez, D. Sarkar, D. N. Krizhanovskii, S. S. Gavrilov, K. Biermann, M. S. Skolnick, and P. V. Santos, "Exciton-polariton gap solitons in two-dimensional lattices," *Phys. Rev. Lett.*, vol. 111, p. 146401, 2013.

[27] V. Negoita, D. W. Snoke, and K. Eberl, "Stretching quantum wells: A method for trapping free carriers in gaas heterostructures," *Applied Physics Letters*, vol. 75, no. 14, 1999.

[28] R. Balili, V. Hartwell, D. Snoke, L. Pfeiffer, and K. West, "Bose-einstein condensation of microcavity polaritons in a trap," *Science*, vol. 316, no. 5827, pp. 1007–1010, 2007.

[29] C. W. Lai, N. Y. Kim, S. Utsunomiya, G. Roumpos, H. Deng, M. D. Fraser, T. Brynes, P. Recher, N. Kumada, T. Fujisawa, and Y. Yamamoto, "Coherent zero-state and pi-state in an exciton-polariton condensate array," *Nature*, vol. 450, pp. 529–532, 2007.

[30] N. Y. Kim, k. Kusudo, C. Wu, N. Masumoto, A. Loffler, S. Hofling, N. Kumada, L. Worschech, A. Forchel, and Y. Yamamoto, "Dynamical d-wave condensation of exciton-polaritons in a two-dimensional square-lattice potential," *Nature Physics*, vol. 7, pp. 681–686, 2011.

[31] O. E. Daif, A. Baas, T. Guillet, J. P. Brantut, R. I. Kaitouni, J. L. Staehli, F. Morier-Genoud, and B. Deveaud, "Polariton quantum boxes in semiconductor microcavities," *App. Phys. Lett.*, vol. 88, no. 061105, 2006.

[32] L. Ferrier, E. Wertz, R. Johne, D. D. Solnyshkov, P. Senellart, I. Sagnes, A. Lemaitre, G. Malpuech, and J. Bloch, "Interactions in confined polariton condensates," *Phys. Rev. Lett.*, vol. 106, no. 126401, 2011.

[33] S. Azzini, D. Gerace, M. Galli, I. Sagnes, R. Braive, A. Lemaître, J. Bloch, and D. Bajoni, "Ultra-low threshold polariton lasing in photonic crystal cavities," *App. Phys. Lett.*, vol. 99, no. 111106, 2011.

[34] R. J. Barbour, P. A. Dalgarno, A. Curran, K. M. Nowak, H. J. Baker, D. R. Hall, N. G. Stoltz, P. M. Petroff, and R. J. Warburton, "A tunable microcavity," *Journal of Applied Physics*, vol. 110, no. 5, 2011.

[35] T. Steinmetz, Y. Colombe, D. Hunger, T. W. Hänsch, A. Balocchi, R. J. Warburton, and J. Reichel, "Stable fiber-based fabry-pérot cavity," *Applied Physics Letters*, vol. 89, no. 11, pp. –, 2006.

[36] Y. Colombe, T. Steinmetz, G. Dubois, F. Linke, D. Hunger, and J. Reichel, "Strong atom-field coupling for bose-einstein condensates in an optical cavity on a chip," *Nature*, vol. 450, pp. 272–276, 2007.

[37] A. Muller, E. B. Flagg, M. Metcalfe, J. Lawall, and G. S. Solomon, "Coupling an epitaxial quantum dot to a fiber-based external-mirror microcavity," *Applied Physics Letters*, vol. 95, no. 17, 2009.

[38] D. Hunger, C. Deutsch, R. J. Barbour, R. J. Warburton, and J. Reichel, "Laser micro-fabrication of concave, low-roughness features in silica," *AIP Advances*, vol. 2, no. 1, 2012.

[39] J. Miguel-Sánchez, A. Reinhard, E. Togan, T. Volz, A. Imamoglu, B. Besga, J. Reichel, and J. Estève, "Cavity quantum electrodynamics with charge-controlled quantum dots coupled to a fiber fabry–perot cavity," *New Journal of Physics*, vol. 15, no. 4, p. 045002, 2013.

[40] L. Greuter, S. Starosielec, D. Najer, A. Ludwig, L. Duempelmann, D. Rohner, and R. J. Warburton, "A small mode volume tunable microcavity: Development and characterization," *Applied Physics Letters*, vol. 105, no. 12, 2014.

[41] P. R. Dolan, G. M. Hughes, F. Grazioso, B. R. Patton, and J. M. Smith, "Femtoliter tunable optical cavity arrays," *Opt. Lett.*, vol. 35, no. 21, 2010.

[42] M. Trupke, E. A. Hinds, S. Eriksson, E. A. Curtis, Z. Moktadir, E. Kukharenka, and M. Kraft, "Microfabricated high-finesse optical cavity with open access and small volume," *Applied Physics Letters*, vol. 87, no. 21, 2005.

[43] G. Cui, J. M. Hannigan, R. Loeckenhoff, F. M. Matinaga, M. G. Raymer, S. Bhongale, M. Holland, S. Mosor, S. Chatterjee, H. M. Gibbs, and G. Khitrova, "A hemispherical, high-solid-angle optical micro-cavity for cavity-qed studies," *Opt. Express*, vol. 14, no. 6, pp. 2289–2299, 2006.

[44] M. H. Anderson, J. R. Ensher, M. R. Mathews, C. E. Wieman, and E. A. Cornell, "Observation of bose-einstein condensation in dilute atomic vapor," *Science*, vol. 269, pp. 198–201, 1995.

[45] K. B. Davis, M. O. Mewes, M. R. Andrews, N. J. van Druten, D. S. Durfee, D. M. Kurn, and W. Ketterle, "Bose-einstein condensation in a gas of sodium atoms," *Phys. Rev. Lett.*, vol. 75, pp. 3969–3973, 1995.

[46] S. N. Bose, "Plancks law and light quantum hypothesis," *Z. Phys*, pp. 26–178, 1924.

[47] A. Einstein, "Quantum theory of ideal monatomic gases," *Sitzber. Preuss. Akad. Wiss.*, vol. 23, no. 3, 1925.

[48] P. Kapitza, "Viscosity of liquid helium below the lambda-point," *Nature*, vol. 141, no. 74, 1938.

[49] J. F. Allen and A. D. Misener, "Flow of liquid helium ii," *Nature*, vol. 141, no. 75, 1938.

[50] F. London, "The lambda-phenomenon of liquid helium and the bose-einstein degeneracy," *Nature*, vol. 141, no. 643, 1938.

[51] N. N. bogoliubov, "On the theory of superfluidity of helium ii," *J. Phys (USSR)*, vol. 11, no. 23, 1947.

[52] L. D. Landau, "The theory of superfluidity of helium ii," *J. Phys (USSR)*, vol. 5, no. 71, 1941.

[53] R. Feynman, "Atomic theory of the 2-fluid model of liquid helium," *Phys. Rev.*, vol. 94, no. 262, 1954.

[54] A. Imamoglu, R. J. Ram, S. Pau, and Y. Yamamoto, "Nonequilibrium condensates and lasers without inversion: Exciton-polariton lasers," *Phys. Rev. A*, vol. 53, pp. 4250–4253, 1996.

[55] L. D. Landau and E. M. Lifshitz, *Statistical Physics, vol. 5 of Course of Theoretical Physics*. Butterworth-Heinemann, 3rd ed., 1980.

[56] H. Deng, D. Press, S. Gotzinger, G. Soloman, R. Hey, K. Ploog, and Y. Yamamoto, "Quantum degenerate exciton-polaritons in thermal equilibrium," *Physical Review Letters*, vol. 97, no. 146402, 2006.

[57] E. Wertz, L. Ferrier, D. D. Solnyshkov, P. Senellart, D. Bajoni, A. Miard, A. Lemaître, G. Malpuech, and J. Bloch, "Spontaneous formation of a polariton condensate in a planar gaas microcavity," *Applied Physics Letters*, vol. 95, no. 5, pp. –, 2009.

[58] T.-C. Lu, Y.-Y. Lai, Y.-P. Lan, S.-W. Huang, J.-R. Chen, Y.-C. Wu, W.-F. Hsieh, and H. Deng, "Room temperature polariton lasing vs. photon lasing in a zno-based hybrid microcavity," *Opt. Express*, vol. 20, no. 5, pp. 5530–5537, 2012.

[59] F. Li, L. Orosz, O. Kamoun, S. Bouchoule, C. Brimont, P. Disseix, T. Guillet, X. Lafosse, M. Leroux, J. Leymarie, M. Mexis, M. Mihailovic, G. Patriarche, F. Réveret, D. Solnyshkov, J. Zuniga-Perez, and G. Malpuech, "From excitonic to photonic polariton condensate in a zno-based microcavity," *Phys. Rev. Lett.*, vol. 110, p. 196406, 2013.

[60] S. Christopoulos, G. B. H. von Högersthal, A. J. D. Grundy, P. G. Lagoudakis, A. V. Kavokin, J. J. Baumberg, G. Christmann, R. Butté, E. Feltin, J.-F. Carlin, and N. Grandjean, "Room-temperature polariton lasing in semiconductor microcavities," *Phys. Rev. Lett.*, vol. 98, p. 126405, 2007.

[61] P. Bhattacharya, T. Frost, S. Deshpande, M. Z. Baten, A. Hazari, and A. Das, "Room temperature electrically injected polariton laser," *Phys. Rev. Lett.*, vol. 112, p. 236802, 2014.

[62] S. Kena-Cohen and S. R. Forrest, "Room-temperature polariton lasing in an organic single-crystal microcavity," *Phys. Rev. Lett.*, pp. 371–375, 2010.

[63] K. S. Daskalakis, S. A. Maier, R. Murray, and S. Kena-Cohen, "Nonlinear interactions in an organic polariton condensate," *Nature Materials*, vol. 13, pp. 271–278, 2014.

[64] K. G. Lagoudakis, B. Pietka, M. Wouters, R. Andre, and B. Deveaud-Pledran, "Coherent oscillations in an exciton–polariton josephson junction," *Physical Review Letters*, vol. 105, no. 120403, 2010.

[65] S. Utsunomiya, L. Tian, G. Roumpos, C. W. Lai, N. Kumada, T. Fujisawa, M. Kuwata-Gonokami, A. Loffler, S. Hofling, and e. a. A. Forchel, "Observation of bogoliubov excitations in exciton–polariton condensates," *Nature Physics*, vol. 4, no. 700, 2008.

[66] V. Kohnle, Y. Leger, M. Wouters, M. Richard, M. T. Portella-Oberli, and B. Deveaud-Pledran, "From single particle to superfluid excitations in a dis- sipative polariton gas," *Physical Review Letters*, vol. 106, no. 255302, 2011.

[67] K. G. Lagoudakis, M. Wouters, M. Richard, A. Baas, I. Carusotto, R. Andre, L. S. Dang, and B. Deveaud-Pledran, "Quantized vortices in an exciton– polariton condensate," *Nature Physics*, vol. 4, no. 706, 2008.

[68] D. Sanvitto, F. M. Marchetti, M. H. Szymanska, G. Tosi, M. Baudisch, F. P. Laussy, D. N. Krizhanovskii, M. S. Skolnick, L. Marrucci, and e. a. A. Lemaitre, "Persistent currents and quantized vortices in a polariton superfluid," *Nature Physics*, vol. 6, no. 527, 2010.

[69] A. Amo, S. Pigeon, D. Sanvitto, V. G. Sala, R. Hivet, I. Carusotto, F. Pisanello, G. Lemenager, R. Houdre, and e. a. E. Giacobino, "Polariton superfluids reveal quantum hydrodynamic solitons," *Science*, vol. 332, no. 1167, 2011.

[70] A. Imamoḡlu, H. Schmidt, G. Woods, and M. Deutsch, "Strongly interacting photons in a nonlinear cavity," *Phys. Rev. Lett.*, vol. 79, pp. 1467–1470, 1997.

[71] T. A. Fulton and G. J. Dolan, "Observation of single-electron charging effects in small tunnel junctions," *Phys. Rev. Lett.*, vol. 59, pp. 109–112, 1987.

[72] M. A. Kastner, "The single-electron transistor," *Rev. Mod. Phys.*, vol. 64, pp. 849–858, 1992.

[73] P. Renucci, T. Amand, X. Marie, P. Senellart, J. Bloch, B. Sermage, and K. V. Kavokin, "Microcavity polariton spin quantum beats without a magnetic field: A

manifestation of coulomb exchange in dense and polarized polariton systems," *Phys. Rev. B*, vol. 72, p. 075317, 2005.

[74] C. Ciuti, V. Savona, C. Piermarocchi, A. Quattropani, and P. Schwendimann, "Role of the exchange of carriers in elastic exciton-exciton scattering in quantum wells," *Phys. Rev. B*, vol. 58, pp. 7926–7933, 1998.

[75] G. Nardin, Y. Léger, B. Piętka, F. Morier-Genoud, and B. Deveaud-Plédran, "Coherent oscillations between orbital angular momentum polariton states in an elliptic resonator," *Journal of Nanophotonics*, vol. 5, no. 1, pp. 053517–053517–7, 2011.

[76] A. Verger, C. Ciuti, and I. Carusotto, "Polariton quantum blockade in a photonic dot," *Phys. Rev. B.*, vol. 73, no. 193306, 2006.

[77] C. Chin, R. Grimm, P. Julienne, and E. Tiesinga, "Feshbach resonances in ultracold gases," *Rev. Mod. Phys.*, vol. 82, pp. 1225–1286, 2010.

[78] M. Wouters, "Resonant polariton-polariton scattering in semiconductor microcavities," *Phys. Rev. B*, vol. 76, p. 045319, 2007.

[79] I. Carusotto, T. Volz, and A. Imamoğlu, "Feshbach blockade: Single-photon nonlinear optics using resonantly enhanced cavity polariton scattering from biexciton states," *EPL (Europhysics Letters)*, vol. 90, no. 3, p. 37001, 2010.

[80] N. Takemura, S. Trebaol, M. Wouters, M. Portella-Oberli, and B. Deveaud, "Polaritonic feshbach resonance," *Nature Physics*, vol. 10, pp. 500–504, 2014.

[81] T. C. H. Liew and V. Savona, "Single photons from coupled quantum modes," *Phys. Rev. Lett.*, vol. 104, p. 183601, 2010.

[82] S. Schwarz, S. Dufferwiel, P. M. Walker, F. Withers, A. A. P. Trichet, M. Sich, F. Li, E. A. Chekhovich, D. N. Borisenko, N. N. Kolesnikov, K. S. Novoselov, M. S. Skolnick, J. M. Smith, D. N. Krizhanovskii, and A. I. Tartakovskii, "Two-dimensional metal–chalcogenide films in tunable optical microcavities," *Nano Letters*, vol. 0, no. 0, p. null, 0. PMID: 25375802.

[83] Z. Di, H. V. Jones, P. R. Dolan, S. M. Fairclough, M. B. Wincott, J. Fill, G. M. Hughes, and J. M. Smith, "Controlling the emission from semiconductor quantum dots using ultra-small tunable optical microcavities," *New Journal of Physics*, vol. 14, no. 10, p. 103048, 2012.

[84] A. E. Siegman, *Lasers*. University Science Books, 1986.

[85] G. Nardin, Y. Léger, B. Pietka, F. Morier-Genoud, and B. Deveaud-Plédran, "Phase-resolved imaging of confined exciton-polariton wave functions in elliptical traps," *Phys. Rev. B*, vol. 82, p. 045304, 2010.

[86] A. Oskooi, D. Roundy, M. Ibanescu, P. Bermel, J. Joannopoulos, and S. Johnson, "Meep: A flexible free-software package for electromagnetic simulations by the fdtd method," *Computer Physics Communications*, vol. 181, pp. 687–702, 2010.

[87] P. R. Dolan, *Ultra-small open access microcavities for enhancement of the light-matter interaction*. Dphil, University of Oxford, 2012.

[88] E. A. Cerda-Méndez, D. Krizhanovskii, K. Biermann, K. Guda, R. Bradley, R. Hey, P. V. Santos, and M. S. Skolnick, "One dimensional confinement of microcavity polaritons using non-piezoelectric surface acoustic waves," *Physica E*, vol. 42, pp. 2548–2551, 2010.

[89] D. Hunger, T. Steinmetz, Y. Colombe, C. Deutsch, T. W. Hänsch, and J. Reichel, "A fiber fabry–perot cavity with high finesse," *New Journal of Physics*, vol. 12, no. 6, p. 065038, 2010.

[90] A. Muller, E. B. Flagg, J. R. Lawall, and G. S. Solomon, "Ultrahigh-finesse, low-mode-volume fabry-perot microcavity," *Opt. Lett.*, vol. 35, no. 13, pp. 2293–2295, 2010.

[91] V. Savona and C. Piermarocchi, "Microcavity polaritons: Homogeneous and inhomogeneous broadening in the strong coupling regime," *Physica Status Solidi (a)*, vol. 164, no. 1, pp. 45–51, 1997.

[92] A. V. Kavokin, J. J. Baumberg, G. Malpuech, and F. P. Laussy, *Microcavities*. Series on Semiconductor Science and Technology, Oxford University Press, 2007.

[93] G. Nardin, T. Paraïso, R. Cerna, B. Pietka, Y. Léger, O. El Daif, F. Morier-Genoud, and B. Deveaud-Plédran, "Probability density optical tomography of confined quasiparticles in a semiconductor microcavity," *Applied Physics Letters*, vol. 94, no. 18, p. 181103, 2009.

[94] R. Meucci, A. Labate, and M. Ciofini, "Polarization properties of low-order laguerre - gauss modes in a laser," *Quantum and Semiclassical Optics: Journal of the European Optical Society Part B*, vol. 9, no. 4, p. L31, 1997.

[95] I. Iorsh, M. Glauser, G. Rossbach, J. Levrat, M. Cobet, R. Butté, N. Grandjean, M. A. Kaliteevski, R. A. Abram, and A. V. Kavokin, "Generic picture of the emission

properties of iii-nitride polariton laser diodes: Steady state and current modulation response," *Phys. Rev. B*, vol. 86, p. 125308, 2012.

[96] A. Amo, T. C. H. Liew, C. Adrados, R. Houdre, E. Giacobino, A. V. Kavokin, and A. Bramati, "Exciton-polariton spin switches," *Nat Photon*, vol. 4, no. 6, pp. 361–366, 2010.

[97] A. V. Kavokin, I. A. Shelykh, T. Taylor, and M. M. Glazov, "Vertical cavity surface emitting terahertz laser," *Phys. Rev. Lett.*, vol. 108, p. 197401, 2012.

[98] D. Sanvitto, S. Pigeon, A. Amo, D. Ballarini, M. De Giorgi, I. Carusotto, R. Hivet, F. Pisanello, V. G. Sala, P. S. S. Guimaraes, R. Houdre, E. Giacobino, C. Ciuti, A. Bramati, and G. Gigli, "All-optical control of the quantum flow of a polariton condensate," *Nat Photon*, vol. 5, no. 10, pp. 610–614, 2011.

[99] J. Keeling and N. G. Berloff, "Spontaneous rotating vortex lattices in a pumped decaying condensate," *Phys. Rev. Lett.*, vol. 100, p. 250401, 2008.

[100] E. Cancellieri, T. Boulier, R. Hivet, D. Ballarini, D. Sanvitto, M. H. Szymanska, C. Ciuti, E. Giacobino, and A. Bramati, "Merging of vortices and antivortices in polariton superfluids," *Phys. Rev. B*, vol. 90, p. 214518, 2014.

[101] R. Hivet, E. Cancellieri, T. Boulier, D. Ballarini, D. Sanvitto, F. M. Marchetti, M. H. Szymanska, C. Ciuti, E. Giacobino, and A. Bramati, "Interaction-shaped vortex-antivortex lattices in polariton fluids," *Phys. Rev. B*, vol. 89, p. 134501, 2014.

[102] G. Christmann, G. Tosi, N. G. Berloff, P. Tsotsis, P. S. Eldridge, Z. Hatzopoulos, P. G. Savvidis, and J. J. Baumberg, "Polariton ring condensates and sunflower ripples in an expanding quantum liquid," *Phys. Rev. B*, vol. 85, p. 235303, 2012.

[103] N. B. G. Franchetti and J. Baumberg, "Exploiting quantum coherence of polaritons for ultra sensitive detectors," *Arxiv*, 2012.

[104] K. T. Kapale and J. P. Dowling, "Vortex Phase Qubit: Generating Arbitrary, Counterrotating, Coherent Superpositions in Bose-Einstein Condensates via Optical Angular Momentum Beams," *Physical Review Letters*, vol. 95, no. 17, p. 173601, 2005.

[105] D. N. Krizhanovskii, D. M. Whittaker, R. A. Bradley, K. Guda, D. Sarkar, D. Sanvitto, L. Vina, E. Cerda, P. Santos, K. Biermann, R. Hey, and M. S. Skolnick, "Effect of Interactions on Vortices in a Nonequilibrium Polariton Condensate," *Physical Review Letters*, vol. 104, no. 12, p. 126402, 2010.

[106] R. Dall, M. D. Fraser, A. S. Desyatnikov, G. Li, S. Brodbeck, M. Kamp, C. Schneider, S. Höfling, and E. A. Ostrovskaya, "Creation of orbital angular momentum states with chiral polaritonic lenses," *Phys. Rev. Lett.*, vol. 113, p. 200404, 2014.

[107] L. E. Sadler, J. M. Higbie, S. R. Leslie, M. Vengalattore, and D. Stamper-Kurn, "Spontaneous symmetry breaking in a quenched ferromagnetic spinor bose-einstein condensate.," *Nature*, vol. 443, pp. 312–315, 2006.

[108] F. Manni, Y. Léger, Y. G. Rubo, R. André, and B. Deveaud, "Hyperbolic spin vortices and textures in exciton–polariton condensates," *Nat Commun*, vol. 4, 2013.

[109] A. Mair, A. Vaziri, G. Weihs, and A. Zeilinger, "Entanglement of the orbital angular momentum states of photons," *Nature*, vol. 412, no. 6844, pp. 313–316, 2001.

[110] E. Nagali, F. Sciarrino, F. De Martini, L. Marrucci, B. Piccirillo, E. Karimi, and E. Santamato, "Quantum Information Transfer from Spin to Orbital Angular Momentum of Photons," *Physical Review Letters*, vol. 103, no. 1, p. 013601, 2009.

[111] A. Z. Khoury, C. E. R. Souza, A. R. Vieira, and M. O. Hor-Meyll, "Quantum information processing with spin-orbit laser modes," in *SPIE NanoScience + Engineering* (H.-J. Drouhin, J.-E. Wegrowe, and M. Razeghi, eds.), p. 881310, International Society for Optics and Photonics, 2013.

[112] G. Panzarini, L. C. Andreani, A. Armitage, D. Baxter, M. S. Skolnick, V. N. Astratov, J. S. Roberts, A. V. Kavokin, M. R. Vladimirova, and M. A. Kaliteevski, "Exciton-light coupling in single and coupled semiconductor microcavities: Polariton dispersion and polarization splitting," *Phys. Rev. B*, vol. 59, pp. 5082–5089, 1999.

[113] Y. K. Kato, R. C. Myers, A. C. Gossard, and D. D. Awschalom, "Observation of the spin hall effect in semiconductors," *Science*, vol. 306, no. 5703, pp. 1910–1913, 2004.

[114] M. Z. Hasan and C. L. Kane, "Colloquium: Topological insulators," *Reviews of Modern Physics*, vol. 82, no. 4, pp. 3045–3067, 2010.

[115] C. Leyder, M. Romanelli, J. P. Karr, E. Giacobino, T. C. H. Liew, M. M. Glazov, A. V. Kavokin, G. Malpuech, and A. Bramati, "Observation of the optical spin Hall effect," *Nat Phys*, vol. 3, no. 9, pp. 628–631, 2007.

[116] R. Hivet, H. Flayac, D. D. Solnyshkov, D. Tanese, T. Boulier, D. Andreoli, E. Giacobino, J. Bloch, A. Bramati, G. Malpuech, and A. Amo, "Half-solitons in a polari-

ton quantum fluid behave like magnetic monopoles," *Nature Physics*, vol. 8, no. 10, pp. 724–728, 2012.

[117] L. Lu, J. D. Joannopoulos, and M. Soljačić, "Topological photonics," *Nature Photonics*, vol. 8, no. 11, pp. 821–829, 2014.

[118] A. Nalitov, D. Solnyshkov, and G. Malpuech, "Polariton z topological insulator," 2014.

[119] C. L. Kane and E. J. Mele, "Quantum spin hall effect in graphene," *Phys. Rev. Lett.*, vol. 95, p. 226801, 2005.

[120] M. Konig, S. Wiedmann, C. Brune, A. Roth, H. Buhmann, L. W. Molenkamp, X.-L. Qi, and S.-C. Zhang, "Quantum spin hall insulator state in hgte quantum wells," *Science*, vol. 318, no. 5851, pp. 766–770, 2007.

[121] A. Kavokin, G. Malpuech, and M. Glazov, "Optical spin hall effect," *Phys. Rev. Lett.*, vol. 95, p. 136601, 2005.

[122] V. G. Sala, D. D. Solnyshkov, I. Carusotto, T. Jacqmin, A. Lemaitre, H. Tercas, A. Nalitov, M. Abbarchi, E. Galopin, I. Sagnes, J. Bloch, G. Malpuech, and A. Amo, "Spin-orbit coupling for photons and polaritons in microstructures," *Phys. Rev. X*, vol. 5, no. 011034, 2015.

[123] D. H. Foster and J. U. Nöckel, "Methods for 3-d vector microcavity problems involving a planar dielectric mirror," *Optics Communications*, vol. 234, no. 1–6, pp. 351 – 383, 2004.

[124] H. Flayac, D. D. Solnyshkov, I. A. Shelykh, and G. Malpuech, "Transmutation of Skyrmions to Half-Solitons Driven by the Nonlinear Optical Spin Hall Effect," *Phys. Rev. Lett.*, vol. 110, no. 1, p. 016404, 2013.

[125] J. Kasprzak, D. D. Solnyshkov, R. André, L. S. Dang, and G. Malpuech, "Formation of an exciton polariton condensate: thermodynamic versus kinetic regimes," *Phys. Rev. Lett.*, vol. 101, no. 14, p. 146404, 2008.

[126] L. Allen, M. Beijersbergen, R. Spreeuw, and J. Woerdman, "Orbital angular momentum of light and the transformation of Laguerre-Gaussian laser modes," *Physical Review A*, vol. 45, no. 11, pp. 8185–8189, 1992.

[127] M. Wouters, I. Carusotto, and C. Ciuti, "Spatial and spectral shape of inhomogeneous nonequilibrium exciton-polariton condensates," *Phys. Rev. B*, vol. 77, p. 115340, 2008.

[128] E. Wertz, L. Ferrier, D. D. Solnyshkov, R. Johne, D. Sanvitto, A. Lemaitre, I. Sagnes, R. Grousson, A. V. Kavokin, P. Senellart, G. Malpuech, and J. Bloch, "Spontaneous formation and optical manipulation of extended polariton condensates," *Nat Phys*, vol. 6, no. 11, pp. 860–864, 2010.

[129] M. Abbarchi, A. Amo, V. Sala, D. Solnyshkov, H. Flayac, L. Ferrier, I. Sagnes, E. Galopin, A. Lemaitre, G. Malpuech, and J. Bloch, "Macroscopic quantum self-trapping and josephson oscillations of exciton polaritons," *Nature Physics*, vol. 9, pp. 275–279, 2013.

[130] X.-W. Xu and Y. Li, "Strong photon antibunching of symmetric and antisymmetric modes in weakly nonlinear photonic molecules," *Phys. Rev. A*, vol. 90, p. 033809, 2014.

[131] S. Michaelis de Vasconcellos, A. Calvar, A. Dousse, J. Suffczyński, N. Dupuis, A. Lemaître, I. Sagnes, J. Bloch, P. Voisin, and P. Senellart, "Spatial, spectral, and polarization properties of coupled micropillar cavities," *Applied Physics Letters*, vol. 99, no. 10, pp. –, 2011.

[132] S. Ishii and T. Baba, "Bistable lasing in twin microdisk photonic molecules," *Applied Physics Letters*, vol. 87, no. 18, pp. –, 2005.

[133] A. Armitage, M. S. Skolnick, V. N. Astratov, D. M. Whittaker, G. Panzarini, L. C. Andreani, T. A. Fisher, J. S. Roberts, A. V. Kavokin, M. A. Kaliteevski, and M. R. Vladimirova, "Optically induced splitting of bright excitonic states in coupled quantum microcavities," *Phys. Rev. B*, vol. 57, pp. 14877–14881, 1998.

[134] S. Dufferwiel, F. Fras, A. Trichet, P. M. Walker, F. Li, L. Giriunas, M. N. Makhonin, L. R. Wilson, J. M. Smith, E. Clarke, M. S. Skolnick, and D. N. Krizhanovskii, "Strong exciton-photon coupling in open semiconductor microcavities," *Applied Physics Letters*, vol. 104, no. 19, pp. –, 2014.

[135] A. Dousse, J. Suffczyński, O. Krebs, A. Beveratos, A. Lemaître, I. Sagnes, J. Bloch, P. Voisin, and P. Senellart, "A quantum dot based bright source of entangled photon pairs operating at 53 k," *Applied Physics Letters*, vol. 97, no. 8, pp. –, 2010.

[136] E. A. Cerda-Mendez, D. N. Krizhanovskii, M. Wouters, R. Bradley, K. Biermann, K. Guda, R. Hey, P. V. Santos, D. Sarkar, and M. S. Skolnick, "Polariton condensation in dynamic acoustic lattices," *Phys. Rev. Lett.*, vol. 105, p. 116402, 2010.

[137] E. A. Cerda-Mendez, D. N. Krizhanovskii, K. Biermann, R. Hey, M. S. Skolnick, and P. V. Santos, "Dynamic exciton-polariton macroscopic coherent phases in a tunable dot lattice," *Phys. Rev. B*, vol. 86, p. 100301, 2012.

[138] H. Flayac, D. D. Solnyshkov, and G. Malpuech, "Oblique half-solitons and their generation in exciton-polariton condensates," *Phys. Rev. B*, vol. 83, p. 193305, 2011.